Adaptive Model-Predictive Control and Its Applications in Paper-Making Processes

by

Qiugang Lu

B.Sc., Harbin Institute of Technology, 2011
M.Sc., Harbin Institute of Technology, 2013

A THESIS SUBMITTED IN PARTIAL FULFILLMENT OF
THE REQUIREMENTS FOR THE DEGREE OF

DOCTOR OF PHILOSOPHY

in

The Faculty of Graduate and Postdoctoral Studies

(Chemical and Biological Engineering)

THE UNIVERSITY OF BRITISH COLUMBIA

(Vancouver)

January 2018

Abstract

Model-based controllers such as model-predictive control (MPC) have become dominated control strategies for various industrial applications including sheet and film processes such as the machine-directional (MD) and cross-directional (CD) processes of paper machines. However, many industrial processes may have varying dynamics over time and consequently model-based controllers may experience significant performance loss under such circumstances, due to the presence of model-plant mismatch (MPM). We propose an adaptive control scheme for sheet and film processes, consisting of performance assessment, MPM detection, optimal input design, closed-loop identification and controller adaptive tuning.

In this work, four problems are addressed for the above adaptive control strategy. First, we extend conventional performance assessment techniques based on minimum-variance control (MVC) to the CD process, accounting for both spatial and temporal performance limitations. A computationally efficient algorithm is provided for large-scale CD processes. Second, we propose a novel closed-loop identification algorithm for the MD process and then extend it to the CD process. This identification algorithm can give consistent parameter estimates asymptotically even when true noise model structure is not known. Third, we propose a novel MPM detection method for MD processes and then further extend it to the CD process. This approach is based on routine closed-loop identifications with moving windows and process model classifications. A one-class support vector machine (SVM) is used to characterize normal process models from training data and detect the MPM by predicting the classification of models from test data. Fourth, an optimal closed-loop input design is proposed for the CD process based on noncausal modeling to address the complexity from high-dimensional inputs and outputs. Causal-equivalent models can be obtained for the CD noncausal models and thus closed-loop optimal input design can be performed based on the causal-equivalent models.

The effectiveness of the proposed algorithms are verified by industrial examples from paper machines. It is shown that the developed adaptive controllers can automatically tune controller parameters to account for process dynamic changes, without the interventions from users or recommissioning the process. Therefore, the proposed methodology can greatly reduce the costs on the controller maintenance in the process industry.

Lay Summary

A good model of an industrial process is an important prerequisite for high-quality products since most industrial controllers depend on the model. When the quality of the model degrades due to the changes of process characteristics, a new model has to be identified to improve the control performance. In this research, we develop data-based performance metrics to assess the control performance and quality of employed models online. Once the degradation in the quality of process model is detected, an experiment is designed to trigger the identification of underlying process models. This experiment is designed in an optimal way such that the subsequent identification can yield a model as accurate as possible. Based on the updated model, the controller is retuned to improve the control performance. With this scheme, the controller can account for process changes automatically without user interventions and this can significantly reduce the maintenance cost of model-based controllers.

Preface

The results presented in this thesis are based on a close collaboration with Mr. Johan Backstrom and Dr. Michael Forbes from Honeywell Process Solutions at North Vancouver, BC, Canada. Besides, routine closed-loop identification for MD processes in Chapter 2 is collaborated with Lee Rippon from the University of British Columbia. The main algorithms, theoretical verifications, simulations and literature review in Chapter 3-6 are based on my original ideas and joint discussions with my supervisors Prof. Bhushan Gopaluni, Prof. Philip Loewen from University of British Columbia as well as our industrial partners.

- The results in Chapter 2 have been submitted as a US patent: Q. Lu, L. Rippon, B. Gopaluni, M. Forbes, P. Loewen, J. Backstrom and G. Dumont, "Closed-loop model parameter identification for industrial model-based process controllers," Application number H0057287-0108, 2016. This work is also summarized into a paper and to be submitted to the peer reviewed journal: Q. Lu, L. Rippon, B. Gopaluni, M. Forbes, P. Loewen, J. Backstrom and G. Dumont, "A closed-loop ARX output-error identification method for industrial routine operating data".

- The results in Chapter 3 have been submitted as a US patent: Q. Lu, B. Gopaluni, M. Forbes, P. Loewen, J. Backstrom and G. Dumont, "Model-plant mismatch detection using model parameter data clustering for paper machines or other processes", Application number H0057510-0108. This work also has been published as a conference paper: Q. Lu, B. Gopaluni, M. Forbes, P. Loewen, J. Backstrom and G. Dumont, "Model-plant mismatch detection with support vector machines", in Proceedings of the IFAC World Congress, 50(1): 7993-7998, 2017.

- The results in Chapter 4 have been published as a journal paper: Q. Lu, M. Forbes, B. Gopaluni, P. Loewen, J. Backstrom and G. Dumont, "Performance assessment of cross-directional control for paper machines", IEEE Transactions on Control Systems Technology, 25(1): 208-221, 2017.

- The results in Chapter 5 have been submitted as a US patent: Q. Lu, B. Gopaluni, M. Forbes, P.

Loewen, J. Backstrom and G. Dumont, "Model-plant mismatch detection with support vector machines for cross- directional process behavior monitoring", Application number H0059870-0108. This work is also summarized into a paper and to be submitted to the peer reviewed journal: Q. Lu, B. Gopaluni, M. Forbes, P. Loewen, J. Backstrom and G. Dumont, "Model-plant mismatch detection with support vector machines: An application to cross-directional processes".

- The results in Chapter 6 have been published as a US patent: Q. Lu, B. Gopaluni, M. Forbes, P. Loewen, J. Backstrom and G. Dumont, "Optimal closed-loop input design for identification of flat sheet process models", Application number 62305412. It has also been published as a conference paper: Q. Lu, B. Gopaluni, M. Forbes, P. Loewen, J. Backstrom and G. Dumont, "Noncausal modeling and closed-loop optimal input design for cross-directional processes of paper machines", in Americal Control Conference, pp. 2837-2842, 2017.

Table of Contents

List of Tables

List of Figures

Nomenclature

ARX	Autoregressive exogenous
AsN	Asymptotically normal
CD	Cross Direction
CV	Controlled Variable
$\oplus$	Direct sum between sets
$\delta(\cdot)$	Dirichlet function
$\mathbb{E}$	Expectation of a random variable
$\overline{\mathbb{E}}$	Generalized expectation of a random variable
$\mathbf{E}_i$	The i-th basis matrix
FIR	Finite impulse response
FOPTD	First-order plus time-delay
$\mathbf{G}^{\dagger}$	Pseudo-inverse of matrix $\mathbf{G}$
i.i.d	Independent and identically distributed
IMC	Internal model control
IR	Impulse response
$\kappa(\mathbf{x},\mathbf{y})$	Kernel function between two vectors $\mathbf{x}$, $\mathbf{y}$
LQG	Linear quadratic Gaussian
λ^{-1}	Unit backward shift operator in spatial direction
LMI	Linear matrix inequality
MD	Machine Direction
MIMO	Multi-input-multi-output
MISO	Multi-input single-output
MPC	Model-predictive control
MPM	Model-plant mismatch

MV	Manipulated Variable
MVC	Minimum-variance control
$N(\mu, \mathbf{P})$	Multivariate Gaussian distribution with mean μ and covariance $\mathbf{P}$
OE	Output-error
PDF	Probability density function
PEM	Prediction-error method
PRBS	Pseudorandom binary sequence
q^{-1}	Unit backward shift operator in temporal direction
SISO	Single-input-single-output
sup	Supremum of a set
SVM	Support vector machine
$\rightarrow$	Convergence of a sequence of numbers or functions
w.p.1	With probability one

Acknowledgments

I would like to first express my sincere gratitude to my supervisor Professor Bhushan Gopaluni. He introduced me to this university-industry collaborative research project and gave me invaluable guidance towards addressing practical problems arising from the industry. This work would not be possible without his support, patience and inspiring discussions throughout my PhD study. Working with Prof. Gopaluni and his group is one of the most enjoyable experiences in my life.

I am greatly thankful to my co-supervisor, Professor Philip Loewen. He helped a lot in my studies from the initial literature review all the way to the paper writing. I received extensive training on mathematics from working with him on the proofs for our ideas and I believe that I would benefit enormously in my future career from being rigorous, in both research and life.

My sincere appreciation also goes to my industrial supervisors, Dr. Michael Forbes and Mr. Johan Backström. Michael gave me numerous assistances in realizing our algorithms in the real industry. I appreciate those hundreds of productive weekly meetings organized by Michael to implement our algorithms into the real paper machine. These meetings are one of the most important reasons for the success of this project. I also acknowledge Johan for his insightful feedback on our progress to make our work practically significant. Completing this project would have been more difficult without his guidance and steering.

I am also thankful to Prof. Richard Braatz for hosting me at the Department of Chemical Engineering at MIT. He introduced me to a new research area on fault detection and data analytics. I benefited a lot from his broad knowledge and great expertise in control and optimization. I would also like to thank Prof. Benben Jiang from Beijing University of Chemical Technology, China, who was visiting Prof. Richard Braatz's lab at the same time, for his help during my visit at MIT and the fruitful discussions on the new research area.

I would also like to thank all the collaborators and colleagues in my PhD project and study: Lee Rippon, Cristian Gheorghe, Greg Stewart, Yiting Tsai, Mahdi Yousefi, Prof. Guy Dumont. I have been fortunate enough to work with you over the last four years.

Finally, I offer special thanks to my parents and my wife, Hui Tian, for their unyielding support, unconditional love and tolerance in my life. To them I dedicate this dissertation.

Chapter 1

Introduction

The stiff competition globally on the reduction of energy and improvement of quality has exerted extensive pressure on the increasing of all-around efficiency of pulp and paper industry. As one of the major sectors in pulp and paper industry, sheet and film processes are facing strong demands for highly efficient, autonomous, and environmentally sustainable operations to enhance their competitive edge. In this work, we focus on development of novel methods to improve efficiency through automation and adaptive information processing for paper machine that is a typical sheet and film process.

1.1 The paper machine

Paper machines transform with high efficiency a slurry of water and wood cellulose fibres into sheets of paper. The diagram of a typical Fourdrinier paper machine is illustrated in Figure 1.1. A paper machine contains four sections: wet end section, press section, dryer section and post drying section. In the wet end section, diluted fibre (mixture of water and fibre with about 0.5% fibre concentration) is bumped into the headbox. The array of actuators controlling the opening of slice lips at the headbox across the paper sheet are used to adjust the amount of pulp distributed on the drainage belt. The drainage belt moves at a high speed with various suction devices underneath to remove most water in the fibre. In the press section, steam boxes and pressing rolls are used to further dewater the paper sheet, ending with approximate 40% fibre concentration. A series of steam-heated cans further evaporate the water content in the fibres in the dryer section, reducing the water concentration to about 5-9% [1]. In the post drying section paper properties, such as paper sheet thickness (caliper) and surface properties (gloss), are controlled by calendar stacks and finally the paper sheets are wounded up on the reel at the end.

The most important paper properties are sheet weight, moisture content and thickness. These properties are measured by traversing scanners located at the end of paper machine, as shown in Figure 1.1. These scanning sensors travel back and forth across the paper sheet to measure paper properties and thus the scanned

points on the paper product form a zig-zag trajectory due to the movement of paper sheet. The objective in controlling paper machines is to reduce variations in paper properties due to disturbances by increasing controllable bandwidth such that disturbances with frequency less than the bandwidth will be attenuated. For the control of paper machines, there are two important directions that divide paper machines into two parts. The first direction is known as the machine direction (MD) and it refers to the direction in which the paper sheet moves. The other direction is called cross direction (CD) and it is perpendicular to the MD. The primary objective in the control of a paper machine is to make the actual paper properties as close to desired as possible by adjusting the manipulation of actuators [2].

MD control is concerned with controlling the average values of measurement points and MD processes are usually represented as single-input-single-output (SISO) or low-dimensional multi-input-multi-output (MIMO) systems. For example, MD basis weight is controlled by adjusting the fibre concentration of the pulp in the headbox. The overall moisture is controlled by the average amount of steam pumped into the dryer section. Note that Figure 1.1 only shows the structure of CD processes afterwards.

Cross-directional control is a finer-resolution control on the top of MD control. Five types of common CD actuators are shown in Figure 1.1. An array of slice lip actuators are mounted after the headbox and controlling the opening of each slice lip actuator locally can affect the amount of pulp pumped out from the slice lip, thus impacting the local basis weight of fibres on the sheet. Note that slice lip actuators can also influence other properties such as moisture and caliper of the paper sheet. In the press section, an array of steam box actuators are used to facilitate the dewatering by spraying hot steams onto the paper sheet. Rewet showers spray water drops onto the paper sheet to prevent over-drying. Similarly, the calendar stacks, an array of induction heating rolls, are used to change the thickness of paper sheet. All these arrays of actuators can be manipulated individually to modify local properties. Although there exist strong interactions between different arrays of actuators and controlled variables (CVs), in this work, for the cross direction, we mainly focus on the single-array CD process since the methods developed can be easily extended to multiple-array cases.

Compared with MD control, CD control is much more complex due to the characteristics associated with CD processes [3, 4]. First, a typical industrial paper machine may be as wide as 10 meters with hundreds of actuator and measurement bins. If modeled as a multivariable system, the large dimension will make the controller design a challenging problem [5]. Second, due to the spatially-distributed nature, most CD process models are often ill-conditioned, and consequently, a large portion of eigenvector directions with

small eigenvalues are indeed uncontrollable [6]. Third, model uncertainty especially the gain sign uncertainty associated with the uncontrollable eigenvector directions make robust stability difficult to achieve [7, 8].

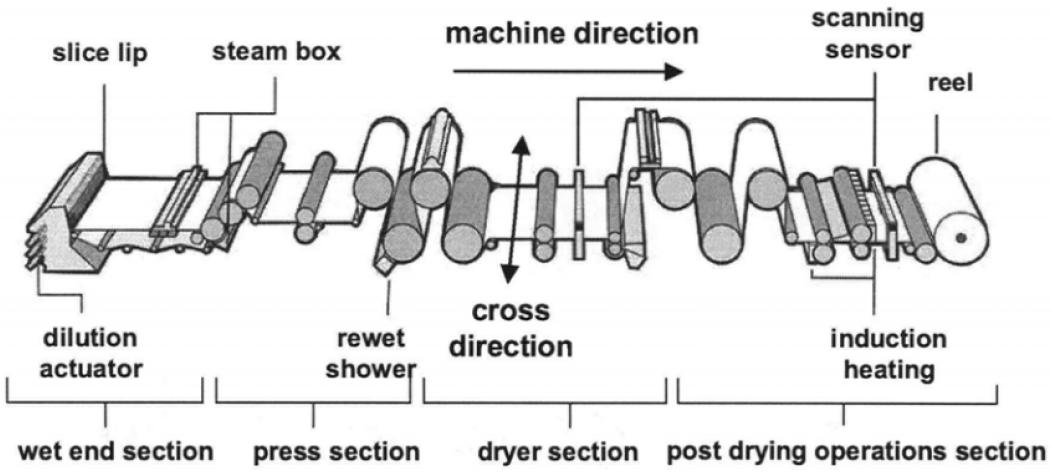

Figure 1.1: Diagram of a typical paper machine [1]

1.2 Research objectives

With the development of model-based control, especially model-predictive control (MPC), most MD and CD controllers are based on models identified *a priori* from experiments such as bump tests [9, 10]. Taking CD processes as an example, classical CD control strategies include two dimensional loop shaping [11], CD model predictive control (MPC) [12], and robust CD control [13]. In these conventional CD control techniques, the quality of CD process model plays a vital role in determining the closed-loop performance. However, as the process operating conditions may change, the quality of the process model may deteriorate and consequently the control performance will degrade [14]. In this case, a new model must be identified for the process. Therefore, it is of great interest to develop techniques to evaluate the control performance by using input-output data. A straightforward idea is to find benchmarks that represent satisfactory control performance against which we can assess the currently implemented controller. Some performance indices can be put forward to quantitatively measure the closeness of the current control performance to the benchmark. As various factors may lead to the control performance deterioration such as poor model quality, inappropriate controller tuning, disturbance change, etc., the process model re-identification is necessary only when the root cause is diagnosed as the model quality degradation. Hence it is attractive to find techniques which are able to detect the existence of significant model-plant mismatches. Since we would like to perform the

mismatch detection task online, it is desirable that the proposed technique can be applied to daily routine operating data. The problem here is that routine industrial data generally lacks excitation signals and thus it is difficult to precisely identify the process model in real-time. In this work, we will propose an effective method to resolve the mismatch detection problem.

Once the poor model quality has been diagnosed as the root cause for performance degradation, a model identification scheme can be initiated to obtain an updated model of the process. A typical model identification scheme involves three stages: optimal input design, model identification and model validation [15]. Among these stages, the optimal input signal (or dithering signal) plays an important role in determining the quality of process model estimates. For a parametric model, the least requirement on the dithering signal is that it should contain enough frequency components so as to excite all necessary modes. Furthermore, a good input signal shall also guarantee a small variance associated with the identified parameters. It is desirable that the perturbation to the process from excitation signals is minimal so as to prevent economic losses and to meet physical process constraints. The objective of optimal input design can be formulated as that of minimizing a scalar function of the covariance matrix of parameter estimates with respect to input sequence (spectrum) subject to a set of constraints. The literature is replete with algorithms for optimal input design in both time and frequency domains, and for both open and closed-loop data [16]. Most current optimal input design techniques can be applied to MD processes. However, for CD processes, the literature on input design focuses only on the open-loop case, where the controller has to be turned off which would result in profit loss for paper mills. In this work, the optimal input signal will be designed in closed-loop, and the large input-output dimensions for CD processes will be taken into account.

Model identification has been a mature research area where a variety of techniques have been developed and applied in the industry. Specifically, model identifications can be roughly grouped into open-loop identifications and closed-loop identifications. Open-loop identifications are known to be simple and flexible as there is no feedback or controller that correlate manipulated variables (MVs) with output noise. For the closed-loop identification, its main advantage is that the system identification is performed during closed-loop operations and this is particularly important for open-loop unstable systems. However, the strong correlation between the input signal and the output disturbance complicates the closed-loop identification and it often leads to biased model estimates [15]. For the MD process, a novel closed-loop identification method will be proposed in this work, aiming at providing unbiased process model estimates. This method will then be extended to the CD process. For the high-dimensional inputs and outputs associated with CD processes,

we will present an iterative approach to simplify the identification of CD processes.

In particular, we will develop (a) a performance monitoring mechanism to evaluate the quality of MD and CD process models by using routine operating data; (b) a model-plant mismatch detection scheme to examine the occurrence of mismatch in real-time; (c) a closed-loop optimal input method particular to the papermaking process; (d) a closed-loop system identification technique. The outcome of this project will be a "quasi" adaptive control scheme [1], as shown in Figure 1.2, which will automatically monitor the performance, identify new models, and re-tune controllers online without user intervention, for both MD and CD processes.

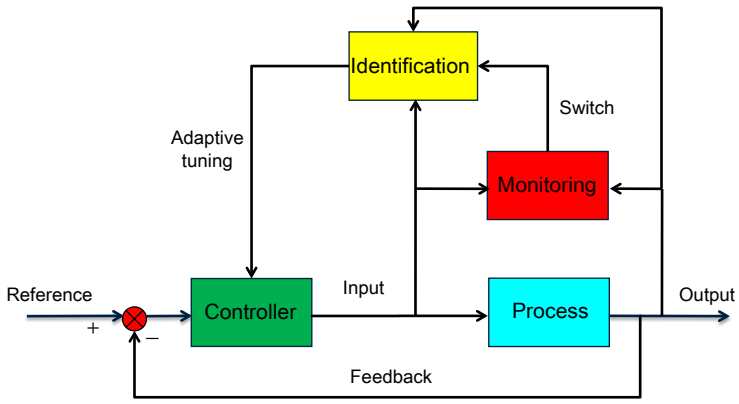

Figure 1.2: The overall adaptive control structure applicable to both MD and CD processes.

1.3 Process models

In this section, we demonstrate typical process models employed in the industry for MD and CD processes. As mentioned in previous sections, single-array MD processes can be well represented by using SISO models. For example, a typical MD process can be modeled as

$$y(t) = G(q)u(t) + H(q)e(t), \tag{1.1}$$

where $G(q)$ is a scalar transfer function, usually with a first-order-plus-time-delay (FOPTD) structure. $H(q)$ is a stable, inversely stable and monic transfer function showing the dynamics of measurement noise $e(t)$. $\{e(t)\}$ is usually assumed to be a Gaussian sequence. $u(t)$ and $y(t)$ are input (e.g., stock flow) and output

[1] Here the adaptive control is in a general sense that resembles iterative identification and control, in contrast to the conventional adaptive control. Thus standard problems related to stability of traditional adaptive control do not occur in the proposed scheme.

(e.g., dry weight) profiles. It shall be pointed out that a multiple-array MD process is usually represented as a lower triangular MIMO system to represent the coupling between different arrays of actuators and paper properties.

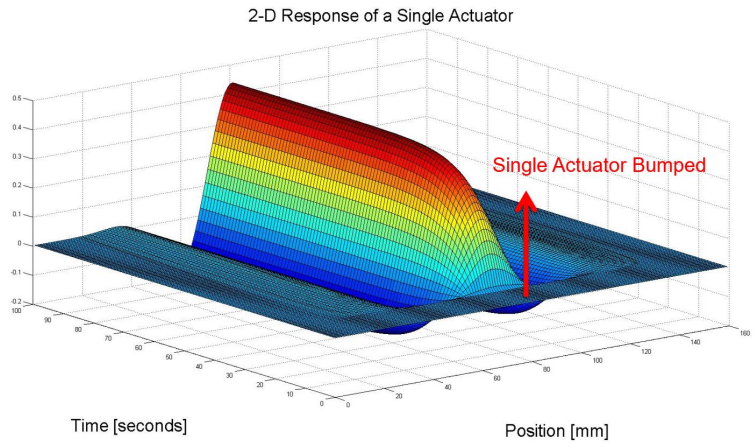

Figure 1.3: Two-dimensional response of a CD actuator under bump signal

Compared with MD, CD processes are much more complicated due to the large number of input-output dimensions. Typical CD processes involve hundreds of actuators and measurement boxes in an array. Essentially, the responses of CD actuators are two-dimensional, in both spatial and temporal directions. Fig. 1.3 shows the response (spatial and temporal) curve of a single actuator under bump signal. Note that the temporal response is similar to that of a first-order model while the spatial response is highly-nonlinear that is modeled by a parameterized nonlinear function. CD measurement sensors are viewed as discretization of the nonlinear response curve. When modeling a CD process, a widely used assumption is the separability between spatial and temporal responses. Under such assumption, the temporal response is described by a FOPTD model with time constant and time-delay as the parameters. The spatial response is depicted by a nonlinear function parameterized by several spatial parameters:

$$b(x) = \frac{\gamma}{2}\left\{ e^{-\frac{\alpha(x+\beta\xi)^2}{\xi^2}} \cos\left[\frac{\pi(x+\beta\xi)}{\xi}\right] + e^{-\frac{\alpha(x-\beta\xi)^2}{\xi^2}} \cos\left[\frac{\pi(x-\beta\xi)}{\xi}\right]\right\}, \tag{1.2}$$

where x is the spatial coordinate and $b(x)$ is the spatial response curve. Gain γ, width ξ, divergence β and attenuation α are four parameters associated with the nonlinear function. The temporal step response and spatial steady-state impulse response of a single actuator are demonstrated in Fig. 1.4. Four spatial parameters, together with two temporal parameters, form the parameter vector that we wish to estimate in

CD model identification.

The nonlinear model (1.2) is not convenient for CD controller design. An additional assumption is placed stating that all actuators are supposed to have identical spatial and temporal response behaviors. Substantial facts from industry have revealed the validity of this assumption for CD actuators in an array except those near the edge. With this assumption, the spatial model is simplified as a highly-structured gain matrix and all actuators share the same temporal model. A generic CD process model is represented as

$$\mathbf{y}(t) = g(q)\mathbf{G}\mathbf{u}(t) + \mathbf{v}(t), \tag{1.3}$$

where $\mathbf{y}(t) \in \mathbb{R}^m$ stands for the measured CD profile, such as basis weight, and $\mathbf{u}(t) \in \mathbb{R}^n$ is the manipulated variable such as the opening of slice lip actuators. m and n are respectively the output and input dimensions. $\mathbf{v}(t) \in \mathbb{R}^m$ represents the output measurement noise. $g(q)$ is a scalar FOPTD transfer function showing the common dynamics of all actuators in the array in temporal direction. $\mathbf{G}$ is a Toeplitz-structured gain representing the spatial responses of actuators at steady-state. In particular, the (i, j)-th entry of $\mathbf{G}$ is determined by the value $b(d_s i - c_j)$ in (1.2), where d_s is the spatial distance between neighboring measurement bins and c_j is the spatial response center of actuator j.

Note that in the following chapters, we will elaborate the MD and CD models in different aspects according to the specific needs in the context.

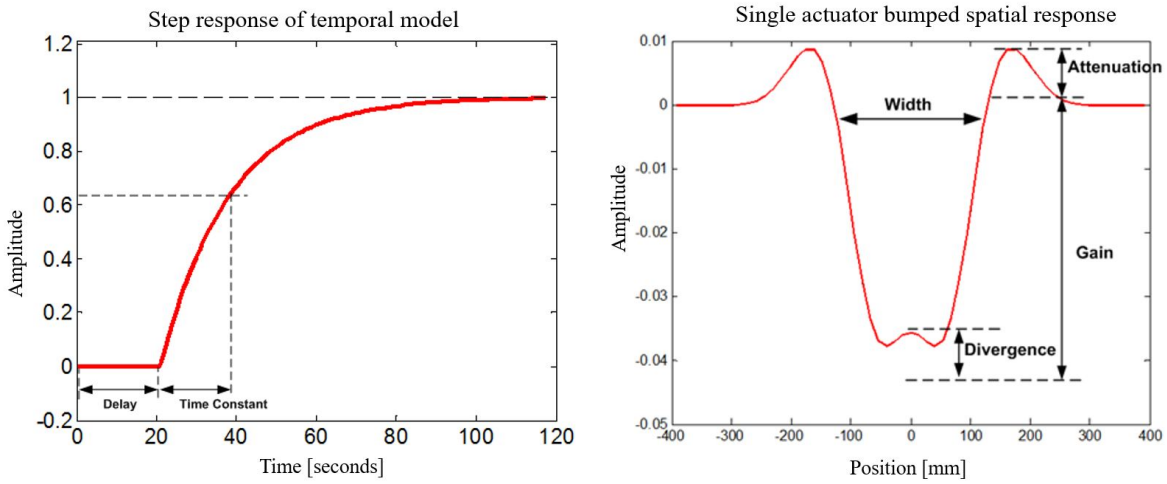

Figure 1.4: Temporal step response and spatial impulse response of a CD actuator.

1.4 Literature review

1.4.1 Performance assessment

Controller performance assessment for univariate systems have been extensively studied in the literature. Excellent surveys on performance assessment for univariate and multivariate processes can be referred to [17–19] and the references therein. Most performance assessment techniques aim at finding a benchmark which characterizes a theoretically best control performance and compare it with the actual performance achieved by the implemented controllers. For a typical control system, there exist a variety of factors that prevent the controller from achieving 'ideal' control performance. For example, we cannot expect the controller to track a setpoint change perfectly without any tracking error since the inherent lag of a physical system in response to any abrupt setpoint change cannot be overcome by any controller. Such constraints on the achievable performance of a controller are called performance limitations, including time-delays, time constants, non-minimum-phase zeros, etc [20]. Thus the performance of a controller cannot be evaluated simply by comparing it with the ideal control performance, but rather, it should be assessed by taking into account the corresponding performance limitations existing in the underlying system.

Among these performance limitations time-delays are the most fundamental and have the most direct influence on the controller performance. Harris [21] first proposed the minimum variance control (MVC) benchmark which specifies the minimum variance that a closed-loop system can achieve when time delay is the fundamental performance limitation. Due to its straightforward intuition and easy deployment, this benchmark has become the most popular tool in the process monitoring area. A time series model is fitted into the measured output data and the first few coefficients are the controller-invariant part (benchmark). The filtering and correlating (FCOR) algorithm was proposed in [18] in which only the output data and time delay are required to calculate the minimum variance benchmark. Furthermore, the MVC benchmark was extended from SISO systems to MIMO systems [19, 22, 23]. Note that for MIMO systems, the interactor matrix has to be factored out as an analogy of the time-delay for the SISO case in order to apply the MVC benchmark. Moreover, it has been proved that the multivariate MVC is able to achieve minimal variance in each individual output channel provided that the interactor matrix is simple or diagonal [18]. A variety of industrial applications using MVC benchmark have emerged afterwards [24], such as paper machine [25] and refinery process [26].

Due to the aggressiveness of the MVC benchmark, a generalized minimum variance controller (GMVC)

benchmark was proposed in [27] which enables the incorporation of input signals into the benchmark. The weight selection strategy was presented in [28] for the GMVC benchmark. The LQG benchmark for performance monitoring was proposed and investigated in [18, 29, 30], where a trade-off curve between the output variance and input variance was obtained and the performance of implemented controllers was evaluated against this curve. Furthermore, due to the wide use of MPC in the industry, performance assessment techniques specific to MPC systems were investigated in [31, 32]. However, most MIMO systems under consideration have small input and output dimensions. A suitable extension of the MVC benchmark to spatially distributed systems, such as the cross direction of paper machines, has received relatively little attention. The high dimensionality of measurements as well as the poorly conditioned nature of the CD process model presents significant challenges for performance monitoring [14].

For CD performance monitoring, in [33], the deviation of an implemented controller from the MVC was estimated in terms of actual input-output data as well as the plant model (known *a priori*). More practical considerations such as actuator constraints were taken into account in the monitoring process. In [34], the original CD model was decoupled into a family of SISO systems and Harris' MVC benchmark was applied to each subsystem. The minimum variance performance index for CD processes was proposed in [35] which accounts for both time-delay performance limitations in the temporal direction and spatial bandwidth performance limitations in the cross (spatial) direction. A Bayesian method was employed to impose Toeplitz structure to the coefficient matrices in estimating the time series model. However, it is not straightforward to obtain a quantitative assessment of the CD processes from the proposed methods. Thus it is desirable to develop an intuitive performance index which directly measures the control performance for the CD process. Moreover, the performance index must be reasonably easy to compute so as to be implemented on-line. Note that the process monitoring for MD processes, with MVC-based benchmark and user-specified benchmark, has been thoroughly studied in [36]. In this work, our focus would be on the performance assessment for CD processes.

1.4.2 Model-plant mismatch detection

Although process monitoring provides a quantitative way of measuring the control performance, control loop performance may deteriorate for various reasons such as model-plant mismatch (poor-quality model), changes in disturbance characteristics, improper tuning of controllers [30]. Among these factors the model-plant mismatch (MPM) is vital since when the mismatch degrades the control performance, system re-

identification will be required to produce an updated model and deploy it to the controller. Note that it is not necessary to perform model re-identification for the other causes of performance degradation. Thus there is an increasing demand on an automated and highly-reliable scheme to directly detect the presence of significant mismatches.

MPM often arises from the susceptibility of industrial processes to changes of operating conditions over time, such as a drift to the chemical process caused by catalyst deactivation [37]. Significant MPM can lead to suboptimal control decisions, production loss, or even closed-loop instability, in which case a process model re-identification procedure is necessary [38]. Traditionally, the MPM detection problem is considered as a component in the diagnostic part of the overall process monitoring hierarchy [39]. A correlation-based method was proposed in [40] which relies on examining the significance of cross-correlations between set-point and model error to separate MPM from other causes of performance degradation. Multivariate chi-squared test on the output and prediction error was proposed to diagnose the presence of MPM in [41]. A hypothesis test method was proposed in [42] to distinguish the effects of changes in process and disturbance on control performance drop. As pointed on in [39], during this early stage of research on MPM detection, most efforts concentrated on the performance monitoring and little endeavors were reported to separate the MPM from other causes. Another category of methods on MPM detection during that period constructs statistics to detect the abrupt changes in the process parameters. A variety of statistical tools such as time series modeling, principal component analysis (PCA), generalized likelihood ratio test and several new statistics were presented in [43–46]. The issue of deciding when to perform the model re-identification, based on PCA and Akaike information criterion, was investigated in [47]. Periodic injection of external excitation signals was required to perform simple tests to detect the model degradation. More recently, attempts on directly identifying the presence or even the model of MPM have become the mainstream in the literature. A method based on partial correlation was illustrated in [48] to address the correlations among MVs. The correlation between each MV and each model residual, after de-correlating the MVs, was employed to examine the occurrence of MPM. In [49], an important method was proposed to discriminate the noise covariance mismatch and process model mismatches. It was shown that both mismatches affect the Kalman filter design, leading to non-white innovations. These two mismatches differ in the order of innovation sequences and from this the MPM can be separated from noise model changes. The impacts of MPM on the sensitivity function was thoroughly explored in [50] and a resultant performance index was put forward for the diagnosis.

Over the last few years, interests on MPM detection have grown significantly, pushing the frontiers towards realistic industrial contexts with closed-loop routine operating data. Several approaches have been reported based on model residual analysis [51], output autocovariance function [37], plant-model ratio [52] and the nominal sensitivity function [52]. Despite these achievements, the MPM detection problem is not yet completely solved. The remaining key issues on this topic can be summarized into two categories: the separability between MPM and noise model change [38, 51], and the usage of external excitations [48, 50]. First, most MPCs perform predictions based solely on a process model or together with a presumed simple noise model, e.g. a step or random-walk disturbance. Despite that changes in true noise model may cause drifts in the variance of process variables, the resultant degradation in control performance shall not be attributed to the MPC. In other words, operators in the industry are more concerned with the quality drop in the underlying process model instead of that of the noise model. An ideal MPM detection approach shall not mistake the changes in noise model as MPM and be robust to such noise changes [38]. Most approaches built on variance-based metrics are susceptible to this issue, such as the minimum-variance benchmark [21]. Second, most present approaches to directly identify the MPM depend on certain external excitations, such as dither signals or setpoint changes. Nevertheless, external excitations bring additional perturbations to the system and inevitably cause profit loss to the industry. Although it is possible to identify the MPM during the setpoint change (e.g. grade changes for paper machines), we prefer to monitor MPM during the routine operation stage, given that most of the time the system operates at steady-state that may be free of any type of external excitations. In terms of CD processes, the problem of MPM detection still remains open. It can be expected that extending previous approaches to CD processes faces extensive difficulties due to the complexity from large-scale inputs and outputs.

1.4.3 Optimal input design

The input design answers the question on how to design an excitation signal optimally to excite the system so that the identified system model is as accurate as possible. For an input design problem, the objective is often formulated as minimizing the variance of parameter estimates by carefully choosing the excitation signal [15]. A default assumption that is often made is that the employed estimator is consistent or unbiased, so that the covariance of the estimator is the only concern that we have. So far, a number of approaches have been put forward, including time-domain, frequency-domain, open-loop and closed-loop approaches.

The optimal input design problem has been extensively investigated since 1970s. During that period, the

research focused on open-loop input design and the design variable was selected as the input signal. Both time domain and frequency domain approaches were explored [53]. In the time domain approaches, the problem was formulated as that of maximizing some scalar function of the Fisher Information Matrix by selecting the input sequence from an admissible compact set. The time domain approaches suffered from the complexity of nonlinear optimizations [54]. In the frequency domain approach, the information matrix was replaced by an asymptotic per sample information matrix, which can be expressed as an affine function of the input spectrum [53]. The optimal input spectrum can be obtained by optimizing a scalar function (e.g. A-optimal, D-optimal, E-optimal, etc.) of the asymptotic per sample covariance matrix subject to constraints [55]. Later on, the results on parameter covariance were extended directly to transfer function estimates, where the asymptotic variance formulas were derived under the assumption that both model order and sample number tend to infinity [56, 57]. The results have been shown to be effective not only for high order models but also for model orders that do not exceed that of the true system. In the nineties, the concept of identification for control emerged where the identification focus was more on the intended use of the model [58]. The identification criteria were chosen to be as close to the control performance as possible. The iterative identification and control design scheme was proposed to achieve these goals [59]. More recently, the focus shifted to the influence of variance error of the estimated model on the set of robust stabilizing controllers. Semidefinite programming with linear matrix inequality (LMI) [60] constraints makes the problem solvable. More specifically, during this period, the research has significantly expanded into the realm of optimal design criteria and constraints. For instance, the design criteria were no longer restricted to be the classical criteria or the variance of transfer function estimates [61]. More practical constraints such as the frequency-by-frequency constraints can be included as well in addition to the conventional power constraints [62]. In conjunction with these new results are the developments of optimization and parameterization techniques associated with the input design problem. It has been shown that most input design problems can be recast as LMI optimization problems, and some parameterization techniques have been proposed to reduce the infinite dimensional LMI into finite dimensions. Two well-known parameterizations are the finite dimensional parameterization and partial correlation parameterization [63]. More recent advances include using graph theory to address the input design problem for closed-loop MPC systems in time domain with probabilistic bound constraints on input and output [64, 65].

With regard to optimal input design for MIMO and ill-conditioned systems, classical results are referred to [66–70]. However, for the CD process, a high-dimensional MIMO and ill-conditioned process, most

existing input design methods were developed for the open-loop case, see [71]. The main drawback of open loop input design is the resultant production loss as normal operations of process risk being interrupted. Results on closed-loop optimal input design for CD processes are scarce, with the current industrial practice of using spatial-bump-temporal-PRBS signals as excitations for closed-loop identification (termed as "bump excitations" in this work) [72]. How to design optimal input excitation signal in the closed-loop for large-scale spatially distributed systems is still an unsolved problem.

1.4.4 Closed-loop identification

Identifying process models using closed-loop data has received extensive attention in the last few decades [73]. There are a number of occasions where open-loop identifications may not be suitable and closed-loop identifications are more desirable. For example, when the underlying system is unstable, the controller has to be in the loop in order to perform identification experiments [59]. Furthermore, if the objective of the identification is to supply a model for the robust controller design, it has been revealed that closed-loop identification is advantageous relative to open-loop identification [74]. A more recent but important application of closed-loop identification is in process performance monitoring, particularly for industrially relevant model-based controllers (e.g., MPC). Many industrial processes collect a large amount of routine operating data and an important aspect of industrial process assessment is to extract metrics in real-time to monitor the performance of control loops. Most of these data are collected in the closed-loop and thus closed-loop system identification becomes one of the most powerful tools in industrial data analytics [75]. One important feature of such closed-loop identification is that the data are collected during the routine operation stage where external excitations (e.g., setpoint change or dither signal) may not exist and no *a priori* knowledge of the noise model is available.

Over the past few decades, closed-loop identification has become a well-established area of research where a number of effective techniques, such the prediction error method (PEM), have been proposed and widely used [15]. Broadly speaking, current closed-loop identification methods can be categorized as follows: direct identification, indirect identification, joint input-output identification method, the two-stage method and the projection method. The direct identification method treats closed-loop data as if they were generated in the open-loop and therefore neglects the correlation between input and noise [76, 77]. However, for this method complete knowledge of the noise model is required to generate an unbiased estimate of process model. To avoid significant bias, the direct identification method is restricted to situations where

the feedback effect is weak (e.g., the controller is highly detuned or the signal-to-noise ratio is high). The indirect identification method proceeds by identifying a closed-loop transfer function (e.g., the sensitivity function) and then factoring out the open-loop process model by assuming that the regulator model is available and accurate [73]. The joint input-output method [78], the two-stage method [79] and the projection method [80] share the same idea, i.e., identifying the closed-loop transfer functions from the dither signal to the process input and output, respectively. The open-loop process model can then be determined from these two closed-loop transfer functions, although the resultant model is often of high order. An additional model order reduction process is necessary to acquire a parsimonious model for further model-based controller design [73]. The latter four closed-loop identification methods require injection of a dither signal into the closed-loop system and in general the dither is independent of the noise. As a consequence, identification of the closed-loop transfer function with these methods is essentially reduced to identification of "open-loop processes". Additionally, the latter four methods are generally developed for linear controllers and applying them when the controller is nonlinear may cause erroneous results. In this case, the direct identification method becomes favorable [75]. These aforementioned closed-loop identification methods can be applied to MD processes. However, the lack of a noise model in MD processes poses a barrier in achieving unbiased estimates of process models. In this work, we propose a novel closed-loop identification method for SISO or low-dimensional MIMO systems, which is applicable to both experimental data and routine operating data.

For CD processes, the large-dimensional nature brings significant challenges for even open-loop identification. A traditional way of dealing with open-loop CD identification is estimating the finite impulse response (FIR) coefficients along the cross direction [81]. Apparently, the parameters estimated from this method have large uncertainty due to the large number of free parameters [82]. Other identification tools use nonlinear least squares to estimate the parameters in determining the spatial response curve [83]. Due to the noncausal nature of spatial response of CD actuators, noncausal parsimonious models are put forward to represent CD processes [82, 84]. However, these methods only consider open-loop data. Their extensions to closed-loop data have not been reported in the literature. In this work, we will present a closed-loop CD identification algorithm, which can be applied to both CD experimental data and routine operation data.

1.5 Outline of this thesis

This thesis covers the entire adaptive control for CD processes and part of adaptive control for MD processes. Note that each process contains components as shown in Fig. 1.2. For the MD process, our focus would be on the model-plant mismatch and closed-loop identification. Detailed simulations on adaptive control for MD processes can be referred to [85]. The performance assessment and optimal input design for MD processes can be referred to the work of a colleague [36].

Chapter 2 is devoted to the development of a novel closed-loop identification scheme. This closed-loop identification contains two steps and it can supply an unbiased estimate for the process model even when the knowledge on the true noise model structure is not available. Moreover, it can operate with closed-loop data collected during an experiment in which a dither signal is injected or the data obtained from routine operating stage in which no external signal is present. Note that this closed-loop identification approach will be employed both in MPM detection stage and final closed-loop identification stage.

Chapter 3 introduces a novel MPM detection scheme based on support vector machines (SVM). This method consists of two steps: routine closed-loop identification and SVM classification for the obtained model estimates. This method can be applied to routine operating data that are free of external excitation signals, and can avoid the issue of being sensitive to noise model changes. This MPM detection scheme will run in parallel with the performance assessment to reduce false alarms for MPM detection.

Chapter 4 demonstrates the extension of classical performance assessment techniques based on MVC benchmark to the CD process. Detailed analysis with regard to performance limitations associated with CD process is provided, based on which a practical CD MVC benchmark is derived. Moreover, to account for the actual tuning status of CD controllers, a user-specified benchmark is proposed to reflect the performance of current controllers. A computationally efficient algorithm is put forward to address the difficulties in computation due to the large number of dimensions in CD processes.

Chapter 5 gives an SVM-based MPM detection method for CD processes, which can be viewed as an extension of the idea from Chapter 3. In particular, a novel iterative CD closed-loop identification is proposed, inspired by the identification of Hammerstein models. Convergence and consistency analysis are performed for this novel CD closed-loop identification approach. SVM-based MPM detection is then applied to the identified CD process models and noise models to monitor the occurrence of model-plant mismatches. With this method, we can detect the MPM with only routine operating data and can discriminate MPM from

noise model changes.

Chapter 6 presents a novel closed-loop input design method for single-array CD processes. The contribution lies in that traditional closed-loop input design, either time-domain approaches or frequency-domain approaches, can not be implemented to CD processes due to the large dimensions of inputs and outputs. Inspired by the noncausal modeling for CD processes, we propose a closed-loop input design idea based on noncausal models. The advantage of this idea is that CD spatial model can be effectively represented by low-order noncausal models, reducing the complexity associated with the input design.

Chapter 7 provides several examples on the adaptive control (more precisely, iterative identification and controller re-tuning) for CD processes. These simulations are performed on a simulator from Honeywell Process Solutions. Specifically, we demonstrate the procedures in detail from introducing a MPM, detecting the existence of MPM, performing closed-loop input design and identification to the adaptive tuning of CD controllers. Various spatial and temporal parametric mismatches are provided to verify the effectiveness of this entire adaptive control scheme.

1.6 Significance of the research

The above adaptive control scheme is proposed based on the stringent requirement in practice for passive performance monitoring and minimal user intervention during the entire monitoring, identification and controller re-tuning loop. Both control performance assessment and MPM detection do not need the injection of external excitations or even setpoint changes to avoid the resultant production loss. Optimal input design and system re-identification are performed in closed-loop to prevent the continuous operation of the process from being interrupted. To enhance of the robustness during the monitoring procedure and reduce false alarms on process deterioration, we combine control performance assessment and MPM detection to make decisions on whether it is necessary to trigger the identification procedures. Although the entire framework is proposed for paper machines, it can easily be extended to other sheet and film processes such as coating, metal rolling and polymer film extrusion. For generic processes that are not spatially distributed, the above scheme is also applicable with minor modifications. With this scheme, industrial manufactures can greatly take advantage of advanced control methods to promote the production efficiency and dramatically reduce the expense on the associated controller maintenance.

Chapter 2

Routine Closed-loop Identification

2.1 Introduction

Over the last few decades, model-based controllers (especially MPC) have become the dominant controllers in most industrial processes. One typical task of process monitoring is to assess the quality of process models used by the controller. This work often involves real-time estimation of the process model based on routine industrial data, which may lack any type of external excitations [86]. Moreover, most industrial MPC may display nonlinear dynamics and thus those closed-loop identification methods relying on external dither signals or linear regulators may not be suitable in this scenario. The direct identification method appears to be appropriate, however, the lack of knowledge of true noise model structure may create biased estimates of the process models [87]. Therefore, it is of great significance to develop a new closed-loop identification method which can be applied to the process monitoring situation, i.e., with or without excitation signals and without knowing the noise model structure.

With the above motivation in mind, we propose a novel closed-loop identification technique. The goal of this method is to overcome the bias issue associated with the direct identification method while preserving its versatility and simplicity in dealing closed-loop data under linear or nonlinear control. A major advantage of the proposed method is its applicability to situations both with and without external excitations. The proposed identification method is referred to as the closed-loop (autoregressive with exogenous input, output error) ARX-OE method. It consists of two steps: high-order ARX modeling in the first step and the OE identification in the second step. In the second step, the OE identification is applied to input and output data that have been filtered by the inverse of estimated noise model from the first step. Some preliminaries and assumptions are presented in the next section followed by a detailed description of the ARX-OE method in Section 2.3 and discussions of the asymptotic properties in Section 2.4. An explanation of the usage of this method for routine industrial operating data is provided in Section 2.5. Two examples validating the effectiveness of the ARX-OE method are presented in Section 2.6 with conclusions given in Section 2.7.

2.2 Preliminaries

Consider the following SISO true system with Box-Jenkins structure

$$\mathscr{S}: \quad y(t) = G_0(q)u(t-d) + H_0(q)e_0(t), \tag{2.1}$$

where $y(t)$ and $u(t)$ represent the measured output signal (CV) and input signal (MV), respectively. The true process model, G_0, is a stable minimum-phase rational transfer function that is assumed to have at least one sample delay. The noise model H_0 is a monic, stable and inversely stable filter. The sequence $\{e_0(t)\}$ is independent and identically distributed (i.i.d.) Gaussian white noise with zero mean and variance σ_e^2.

In closed-loop, the input signal $u(t)$ is determined by the following nonlinear mapping

$$u(t) = k(t, u^{t-1}, y^{t-1}, r(t)), \tag{2.2}$$

where $u^{t-1} = \{u(t-1), u(t-2), \ldots, u(1)\}$ and y^{t-1} is defined analogously. The external excitation signal, $r(t)$, can be either the dither signal (normally added to the actuator site) or the setpoint signal. Note that (2.2) is a general representation of the controller and it includes both linear and nonlinear cases. A typical example of a nonlinear controller is MPC with varying active constraints. From the perspective of system identification, a nonlinear controller could be more conducive to closed-loop identification as it is likely to break the correlation between input and noise through the feedback path [15].

Assumption 2.2.1. We assume that all relevant signals in (2.1)-(2.2) are quasi-stationary, i.e., the following conditions hold [15]

$$\begin{aligned} \mathbb{E}[s(t)] &= m(t), \ |m(t)| \leq C, \ \forall t, \\ \overline{\mathbb{E}}[s(t)s(t-\tau)] &= R_s(\tau), \ |R_s(\tau)| \leq C, \ \forall \tau, \end{aligned}$$

where $s(t)$ is a signal in (2.1)-(2.2), C is some constant and $\mathbb{E}$ is the conventional expectation operator for random variables. The generalized expectation operator, $\overline{\mathbb{E}}$, is applicable to the signals consisting of both stochastic and deterministic components

$$\overline{\mathbb{E}}[s(t)] = \lim_{N\to\infty} \frac{1}{N} \sum_{t=1}^{N} \mathbb{E}[s(t)].$$

Furthermore, we define

$$Z^N = \{u(1), y(1), \ldots, u(N), y(N)\},$$

to be a collection of sampled closed-loop data. To facilitate derivations, the following assumption is default unless otherwise explicitly stated.

Assumption 2.2.2. The collected closed-loop input-output data Z^N is informative enough for the selected model structures in the relevant closed-loop identification.

Remark 2.2.1. When external excitation exists, Assumption 2.2.2 holds if the external excitation signal $r(t)$ is persistently exciting of sufficient orders. For the case without external excitation, we assume that the linear or nonlinear controller is complex enough to make this assumption hold, see Section 2.5.2. Note that for the theoretical derivation, in the sequel we assume that $r(t)$ exists. The corresponding results without external excitation can be easily derived by setting $r(t) = 0$.

For the prediction-error method (PEM), a class of model structures are constructed to fit into the data set, parameterized by $\theta = [\rho^T \ \gamma^T]^T \in \Omega_\theta \subseteq \mathbb{R}^{n_\theta}$,

$$\mathscr{M}: \ \ y(t) = G(q,\rho)u(t) + H(q,\gamma)e(t),$$

where $q \in \Omega_\rho \subseteq \mathbb{R}^{n_\rho}$ and $\gamma \in \Omega_\gamma \subseteq \mathbb{R}^{n_\gamma}$ are parameter vectors of the process and noise models, respectively. Define Ω_θ, Ω_ρ, and Ω_γ to be the corresponding convex and compact sets of parameters θ, ρ and γ. First we introduce the definition of uniform stability for a model structure [15].

Definition 2.2.1. Let $G(q,\theta) = \sum_{k=1}^{\infty} g_k(\theta) q^{-k}$ be a transfer function depending on parameter $\theta \in \Omega_\theta$. The model structure $G(q,\theta), \theta \in \Omega_\theta$, is said to be *uniformly stable* on Ω_θ if there exists a sequence $\{g(k)\}$ independent of θ such that $\sum_{k=1}^{\infty} g(k) < \infty$ and $|g_k(\theta)| \leq g(k)$ for each k and every $\theta \in \Omega_\theta$.

We further suppose that the selected model structures $G(q,\rho)$ and $H(q,\gamma)$ are uniformly stable ('uniformly' is with respect to the parameter θ and ρ) and $H(q,\gamma)$ is also inversely uniformly stable. Note that in what follows we may use G_ρ, $G_\rho(q)$ and $G(q,\rho)$ interchangeably if there is no risk of confusion.

Assumption 2.2.3. It is assumed that the true process model is contained in the set of selected process model structures, i.e.,

$$G_0 \in \mathscr{G} \triangleq \{G(q,\rho) | \rho \in \Omega_\rho\}.$$

Further, we assume that all relevant closed-loop transfer functions formed by the selected family of model structures are uniformly stable under the controller in (2.2). Note that this condition also guarantees closed-loop stability of the true system since the true system is contained in the selected model structure.

We further stress that Assumption 2.2.3 is valid from a practical point of view since for most industrial processes the required *a priori* knowledge of the process is often available. It is well-known that if the selected noise structure also contains the true noise model, then the direct identification method provides consistent estimates for both the process and noise model parameters, regardless of whether the experiment is conducted in closed-loop or open-loop [15]. However, in practice this statement is too stringent to hold since in general, the characteristics of noise are too complex to analyze or come up with an appropriate model structure. Thus discrepancy between the true noise model and the selected noise model structure is inevitable. Moreover, for process control engineers, reliability of the identified process model is more important than that of the noise model for controller design.

A direct consequence of this noise model mismatch is a biased estimate of the process model if the PEM is applied to closed-loop data (we only consider the direct closed-loop identification method for now). To be more specific, taking the fixed noise model, $H_*(q)$, as an example, the process model parameter estimate is shown to be [15]

$$\rho^* = \arg\min_{\rho\in\Omega_\rho} \frac{1}{2\pi}\int_{-\pi}^{\pi} \frac{\left|G_0(e^{j\omega}) + B(e^{j\omega}) - G_\rho(e^{j\omega})\right|^2 \Phi_u(\omega)}{\left|H_*(e^{j\omega})\right|^2} d\omega, \tag{2.3}$$

where $B(e^{j\omega})$ is the bias term and

$$B(e^{j\omega}) = \frac{\left(H_0(e^{j\omega}) - H_*(e^{j\omega})\right)\Phi_{ue}(\omega)}{\Phi_u(\omega)}, \tag{2.4}$$

where $\Phi_{ue}(\omega)$ is the cross-spectrum between the input and noise. It is obvious that for open-loop data $\Phi_{ue}(\omega) = 0$ and thus the OE structure with a fixed noise model can give an unbiased process model estimate. In this work, we propose to use a two-step approach to resolve the bias issue while maintaining other advantages of the direct identification method.

2.3 The closed-loop ARX-OE identification method

In this section we describe the proposed closed-loop ARX-OE identification method in detail. The proposed closed-loop identification method, as mentioned above, consists of two consecutive steps: high-order ARX identification followed by closed-loop OE identification using filtered input-output data.

2.3.1 First step: high-order ARX identification

Let us first re-write (2.1) in an equivalent form

$$A_0(q)y(t) = B_0(q)u(t) + e_0(t), \tag{2.5}$$

where

$$A_0(q) = \frac{1}{H_0(q)}, \;\; B_0(q) = \frac{G_0(q)}{H_0(q)}.$$

Since $H_0(q)$ is assumed to be inversely stable, it is clear that $A_0(q)$ and $B_0(q)$ are also stable. It is worth pointing out that in most cases, the impulse response (IR) coefficients of $A_0(q)$ and $B_0(q)$ contain infinite terms, i.e.,

$$A_0(q) = 1 + \sum_{k=1}^{\infty} a_k^0 q^{-k}, \;\; B_0(q) = \sum_{k=1}^{\infty} b_k^0 q^{-k}. \tag{2.6}$$

Thus the original Box-Jenkins model can be represented by an ARX model but with an infinite number of parameters. Here we propose to use a high-order ARX model to fit the closed-loop data

$$A(q,\eta_n)y(t) = B(q,\eta_n)u(t) + e(t), \tag{2.7}$$

where n is the selected order and

$$A(q,\eta_n) = 1 + \sum_{k=1}^{n} a_k q^{-k}, \;\; B(q,\eta_n) = \sum_{k=1}^{n} b_k q^{-k}, \tag{2.8}$$

with

$$\eta_n = [a_1 \ldots, a_n, b_1, \ldots, b_n]^T.$$

The basic idea is that the IR coefficients may converge to zero after sufficient lags and the high-order ARX model will capture the first few significant coefficients. Based on (2.7) and (2.8), the parameter estimates

of the ARX model can be readily achieved by solving a least-squares problem. The estimate of parameter vector is defined as

$$\hat{\eta}_n = [\hat{a}_1 \ldots, \hat{a}_n, \hat{b}_1, \ldots, \hat{b}_n]^T. \tag{2.9}$$

It is evident that the parameter estimate $\hat{\eta}_n$ under (2.7) and (2.8) will suffer from large variance due to the large number of parameters. In fact, the accuracy of parameter estimates from the first step is consequential to the second step. One remedy to this issue is to add regularizations to the least-squares problem. For theoretical derivations in this work, we employ the regularization with a form shown in [88]: for small $\delta > 0$,

$$R^n_{reg}(N) = \begin{cases} R^n(N), & \text{if } \|R^n(N)^{-1}\|_2 < 2/\delta \\ R^n(N) + \frac{\delta}{2} I, & \text{otherwise} \end{cases}$$

where $R^n(N) = \frac{1}{N}\sum_{t=n+1}^{N} \varphi^n(t)\varphi^n(t)^T$ with the regressor $\varphi^n(t) = [-y(t)\ u(t)\ \ldots\ -y(t-n)\ u(t-n)]^T$. N is the sample size. It has been proved in that paper that asymptotically, the first and second order properties of the parameter estimate will not depend on the regularization term. Another important point is that the IR coefficients of most practical noise models tend to decay rapidly and *a priori* information can be used to choose a reasonable model order for the ARX identification in the first step. For theoretical convenience, we make the following assumption which states that as the sample size N tends to infinity, the order $n(N)$ (as a function of N) of the selected ARX structure (2.7) is allowed to tend to infinity but with a much slower increase rate than N.

Assumption 2.3.1. For the high-order ARX model (2.7), it holds that

$$n(N) \to \infty, \ \ n(N)^{3+\delta}/N \to 0, \ \ \text{as } N \to \infty, \tag{2.10}$$

where $\delta > 0$ is some constant.

It is straightforward that the parameters in (2.7) can be estimated with ordinary least-squares. Denote

$$\hat{\eta}_N = \hat{\eta}_{n(N)}, \tag{2.11}$$

to represent the least-squares estimates of the parameter η_n when n is allowed to tend to infinity as a function of N. We also define η_0 as a vector stacking the infinite number of true parameters in the high-order ARX

model, i.e.,

$$\eta_0 = [a_1^0 \ldots, a_n^0, \ldots, b_1^0, \ldots, b_n^0, \ldots]^T. \tag{2.12}$$

In the following sections, we use $A_0(q)$ and $A(q,\eta_0)$ interchangeably as well as $B_0(q)$ and $B(q,\eta_0)$.

Before proceeding to the second step of the ARX-OE method, we present the following lemma [88].

Lemma 2.3.1. *Consider the true high-order ARX model in* (2.5) *and the selected model structure in* (2.7)*. If the previous assumptions hold, then for the least-squares estimate $\hat{\eta}_N$, we have*

$$\sup_{\omega} \left| A(e^{j\omega}, \hat{\eta}_N) - A_0(e^{j\omega}) \right| \to 0, \quad \textit{w.p.1, as } N \to \infty. \tag{2.13}$$

Note that we can acquire a similar statement for $B(e^{j\omega}, \hat{\eta}_N)$. However, as will be explained below, we are only interested in $A(e^{j\omega}, \hat{\eta}_N)$. Lemma 2.3.1 asserts that, asymptotically, in both the sample number and the order of ARX model, the estimate $A(q,\hat{\eta}_N)$ of $A_0(q)$ converges almost surely to the true value. Notice that this lemma holds regardless of whether the data are gathered in open-loop or closed-loop, as long as the corresponding assumptions are satisfied. As will be seen later, this lemma plays an essential role in the asymptotic analysis of the proposed ARX-OE method.

2.3.2 Second step: OE modeling with filtered input and output data

In the second step of the proposed approach, we perform an OE model identification on the filtered input and output signals. Here the filter is chosen as the estimated $A(q,\hat{\eta}_N)$ from the first step. For ease of notation, from now on we define the operation of filtering a signal $s(t)$ using $A(q,\hat{\eta}_N)$ as

$$s(t,\hat{\eta}_N) = A(q,\hat{\eta}_N)s(t),$$

to show this explicit dependence. With this notation, the filtered input and output signals are as follows

$$y(t,\hat{\eta}_N) = A(q,\hat{\eta}_N)y(t), \quad u(t,\hat{\eta}_N) = A(q,\hat{\eta}_N)u(t).$$

To estimate the process model, we fit the following OE model to filtered input-output data, i.e.,

$$y(t,\hat{\eta}_N) = G(q,\rho)u(t,\hat{\eta}_N) + e(t), \quad \rho \in \Omega_\rho, \tag{2.14}$$

where *a priori* information on the process model can be imposed, e.g., a FOPTD model for the paper machine example in the simulation section. The one-step-ahead predictor of the above OE model is

$$\hat{y}(t|t-1,\rho,\hat{\eta}_N) = G(q,\rho)u(t,\hat{\eta}_N), \tag{2.15}$$

and the resulting prediction error is

$$\varepsilon(t,\rho,\hat{\eta}_N) = y(t,\hat{\eta}_N) - \hat{y}(t|t-1,\rho,\hat{\eta}_N) = [G_0 - G(q,\rho)]u(t,\hat{\eta}_N) + \frac{A(q,\hat{\eta}_N)}{A_0(q)}e(t). \tag{2.16}$$

For the prediction error method, the optimal parameter is obtained by minimizing the following objective function

$$\hat{\rho}_N = \arg\min_{\rho\in\Omega_\rho} V_N(\rho,\hat{\eta}_N) = \frac{1}{N}\sum_{t=1}^{N}\frac{1}{2}\varepsilon^2(t,\rho,\hat{\eta}_N). \tag{2.17}$$

Note that solving the OE model identification in (2.16)-(2.17) often involves nonconvex optimization and thus the global minima in general cannot be guaranteed. However, in this work we do not intend to develop techniques to overcome this issue. For details on this topic, see [89].

2.4 Asymptotic analysis of the ARX-OE method

In this section, we will analyze the consistency and asymptotic distribution of the proposed closed-loop ARX-OE identification method.

2.4.1 Consistency analysis

We show that the estimate of process model approaches the true model as the sample size N tends to infinity. First, by replacing $A(q,\hat{\eta}_N)$ in (2.16) using $A(q,\eta_0)$, let us define the prediction error under the ideal filter $A(q,\eta_0)$ as

$$\varepsilon(t,\rho,\eta_0) = y(t) - \hat{y}(t|t-1,\eta_0) = [G_0 - G(q,\rho)]u(t,\eta_0) + e(t), \tag{2.18}$$

and the corresponding loss function as

$$V_N(\rho,\eta_0) = \frac{1}{N}\sum_{t=1}^{N}\frac{1}{2}\varepsilon^2(t,\rho,\eta_0).$$

Defining

$$\overline{V}(\rho,\eta_0) \stackrel{\Delta}{=} \overline{\mathbb{E}}\frac{1}{2}\varepsilon^2(t,\rho,\eta_0), \tag{2.19}$$

the following theorem shows that for large sample size the loss function (2.17) coincides with (2.19) almost surely.

Theorem 2.4.1. *Suppose that Assumptions 2.2.1–2.3.1 hold and consider the loss functions under prefilters* $A(q,\hat{\eta}_N)$ *and* $A(q,\eta_0)$ *as shown in* (2.17) *and* (2.19)*, respectively. If follows that*

$$\sup_{\rho\in\Omega_\rho}\left|V_N(\rho,\hat{\eta}_N)-\overline{V}(\rho,\eta_0)\right|\to 0, \;\; \textit{w.p.1, as } N\to\infty, \tag{2.20}$$

where $\overline{V}(\rho,\eta_0)$ *is defined as in* (2.19)*.*

Proof. See Appendix A.1. ■

Based on the arguments in Theorem 2.4.1, we are ready to show that the estimate of process model is consistent through the following theorem.

Theorem 2.4.2. *Consider the Box-Jenkins model* (2.1) *and the equivalent ARX model* (2.5)*. Assume that the output-error model in* (2.14) *is uniformly stable. Then under Assumptions 2.2.1–2.3.1, the parameter estimate from the ARX-OE method in* (2.17) *is consistent, i.e.,*

$$\hat{\rho}_N\to\rho^*=\arg\min_{\rho\in\Omega_\rho}\frac{1}{2\pi}\int_{-\pi}^{\pi}\left|G_0(e^{j\omega})-G(e^{j\omega},\rho)\right|^2\frac{\Phi_u(\omega)}{|H_0(e^{j\omega})|^2}d\omega, \;\; \textit{w.p.1, as } N\to\infty. \tag{2.21}$$

Proof. Notice that due to the delay in G_0 and $G(q,\rho)$, the term $[G_0-G(q,\rho)]u(t,\eta_0)$ in (2.18) contains only $e(t-s), s\geq 1$, and thus is not correlated with $e(t)$. From the Parseval's theorem, it follows that

$$\overline{V}(\rho,\eta_0)=\frac{1}{4\pi}\int_{-\pi}^{\pi}\left|G_0(e^{j\omega})-G(e^{j\omega},\rho)\right|^2\left|A_0(e^{j\omega})\right|^2\Phi_u(\omega)+\sigma_e^2.$$

Thus based on Theorem 2.4.1, we conclude that (2.21) in Theorem 2.4.2 holds. ■

Remark 2.4.1. Theorem 2.4.1 and Theorem 2.4.2 verify the consistency of process model estimate from the proposed ARX-OE method. It should be pointed out that in practice, proper selection of the ARX model may require trial and error or be based on *a priori* knowledge of the process. Although above results are derived under the assumption that the ARX model order tends to infinity, our experience shows that sufficiently high

order is enough to give high-quality estimates of the noise model. However, in practice, the regularization is vital in the first step to reduce the variance associated with the parameter estimate in high-order ARX identification.

2.4.2 Asymptotic distribution

In this section, for simplicity, we restrict our asymptotic distribution analysis for the proposed ARX-OE algorithm to linear feedback case, i.e., the controller in (2.2) is reduced to (suppose $r(t)$ is at the process input site)

$$u(t) = -K(q)y(t) + r(t), \tag{2.22}$$

where $K(q)$ is the linear feedback controller. We assume, without loss of generality, that $r(t)$ is an excitation signal independent of $e(t)$. Let us suppose that all relevant closed-loop transfer functions are exponentially stable under (2.22). The closed-loop system is denoted as

$$y(t) = S_0 G_0 r(t) + S_0 H_0 e(t), \tag{2.23}$$

$$u(t) = S_0 r(t) - S_0 K H_0 e(t), \tag{2.24}$$

where S_0 is the sensitivity function, i.e.,

$$S_0 = \frac{1}{1 + G_0 K}. \tag{2.25}$$

Before proceeding to the main results, the following lemma is necessary for the analysis of asymptotic covariance of high-order ARX model parameter estimates [88].

Lemma 2.4.1. *Assume that polynomials $A_0(q)$ and $B_0(q)$ in the ARX representation* (2.5)-(2.6) *of the Box-Jenkins model* (2.1) *are stable. Suppose that Assumption 2.3.1 holds, then*

$$\left\| \mathbb{E}\left[N(\hat{\eta}_N - \bar{\eta}_{n(N)})(\hat{\eta}_N - \bar{\eta}_{n(N)})^T \right] - \sigma_e^2 [\overline{\mathbf{R}}^{n(N)}]^{-1} \right\|_2 \to 0, \text{ as } N \to \infty, \tag{2.26}$$

where $\bar{\eta}_{n(N)}$ is the expected value of $\hat{\eta}_N$ and

$$\overline{\mathbf{R}}^n = \overline{\mathbb{E}}[\varphi_t^n (\varphi_t^n)^T], \;\; \varphi_t^n = [-y(t-1) \; \ldots \; -y(t-n) \; u(t-1) \; \ldots \; u(t-n)]^T. \tag{2.27}$$

The above lemma explicitly shows the asymptotic covariance of parameter estimates. It will be utilized in the following theorem to derive the asymptotic distribution of parameter estimates from the closed-loop ARX-OE algorithm. Note that in the following theorem we denote $G'_\rho(\rho_0) = dG/d\rho|_{\rho=\rho_0}$ and so on to reduce the notational burden. First we need the following lemma.

Lemma 2.4.2. *Let $\{e(t)\}$ be a sequence of independent random variables with zero mean and constant variance. Suppose that $z(t)$ is a function of $\{e(k),\ k \le t-1\}$, then the following relation holds*

$$\mathbb{E}[z(t)e(t)\cdot e(s)z(s)] = \mathbb{E}[z(t)z(s)]\cdot\mathbb{E}[e(t)e(s)] = \sigma_e^2\mathbb{E}[z^2(t)]. \tag{2.28}$$

Proof. Given the condition in this lemma, the signal $z(t)$ can be expressed as, $z(t) = f(e(t-1), e(t-2), \ldots)$, where $f(\cdot)$ is some nonlinear function. Then it is straightforward that $z(t)$ is independent of $e(t)$ and similarly $z(s)$ is independent of $e(s)$. If $t \le s-1$, then $e(s)$ is independent of the other three terms and as a result, (2.28) will be zero. Analogously, if $s \le t-1$, then (2.28) is also zero. Thus (2.28) is nonzero only when $t = s$, and the right-hand side of (2.28) is obtained. ■

Lemma 2.4.2 is useful in the derivation of asymptotic distribution of the ARX-OE method. Before presenting the relevant results, first we may notice from (2.27) that

$$\begin{aligned}
\varphi_t^n &= \begin{bmatrix} -G_0\Gamma_n \\ \Gamma_n \end{bmatrix} u(t) + \begin{bmatrix} -\frac{1}{A_0}\Gamma_n \\ 0 \end{bmatrix} e(t) \\
&= \begin{bmatrix} -G_0\Gamma_n S_0 \\ \Gamma_n S_0 \end{bmatrix} r(t) + \begin{bmatrix} G_0\Gamma_n S_0 K H_0 - \frac{\Gamma_n}{A_0} \\ -\Gamma_n K H_0 S_0 \end{bmatrix} e(t) \\
&= \begin{bmatrix} -G_0\Gamma_n S_0 & -\Gamma_n H_0 S_0 \\ \Gamma_n S_0 & -\Gamma_n K H_0 S_0 \end{bmatrix} \begin{bmatrix} r(t) \\ e(t) \end{bmatrix},
\end{aligned} \tag{2.29}$$

where $\Gamma_n = [1\ q\ \ldots\ q^{-n}]^T$. Note that the second equality follows by substituting $u(t)$ with (2.24). The third equality uses $A_0H_0 = 1$, as well as (2.25). Now let us establish the main theorem on the asymptotic distribution of parameters estimates.

Theorem 2.4.3. *Suppose that assumptions 1-4 hold and the feedback controller is linear as in* (2.22)*. Consider the parameter estimates $\hat{\rho}_N$ in* (2.17) *from the closed-loop ARX-OE method. We assume that $\hat{\rho}_N \to \rho_0$,*

w.p.1 as $N \to \infty$*, then*

$$\sqrt{N}(\hat{\rho}_N - \rho_0) \sim AsN(0, \mathbf{P}_\theta), \tag{2.30}$$

where

$$\mathbf{P}_\theta = \left[\overline{\mathbb{E}}\left[\psi(t,\rho,\eta_0)\psi^T(t,\rho,\eta_0)\right]\right]^{-1} \mathbf{Q} \left[\overline{\mathbb{E}}\left[\psi(t,\rho,\eta_0)\psi^T(t,\rho,\eta_0)\right]\right]^{-1},$$

and $\overline{\mathbb{E}}\left[\psi(t,\rho,\eta_0)\psi^T(t,\rho,\eta_0)\right]$ *is the derivative of the predictor in* (2.15) *w.r.t. parameter* ρ*, evaluated at* ρ *and* η_0 *(see* (A.3)*). The term* $\mathbf{Q}$ *is*

$$\begin{aligned}\mathbf{Q} &= \sigma_e^2\overline{\mathbb{E}}[\psi(t,\rho_0,\eta_0)\psi^T(t,\rho_0,\eta_0)] + Z_2^{n(N)}[\overline{\mathbf{R}}^{n(N)}]^{-1}(Z_2^{n(N)})^T + Z_2^{n(N)}[\overline{\mathbf{R}}^{n(N)}]^{-1}\sigma_e^2 \\ &\quad \cdot\overline{\mathbb{E}}\left[\varphi_t^{n(N)}\psi^T(t,\rho_0,\eta_0)\right] + \sigma_e^2\overline{\mathbb{E}}\left[\psi(t,\rho_0,\eta_0)(\varphi_t^{n(N)})^T\right][\overline{\mathbf{R}}^{n(N)}]^{-1}(Z_2^{n(N)})^T,\end{aligned} \tag{2.31}$$

where

$$Z_2^{n(N)} = -\left[\overline{\mathbb{E}}[G'_\rho(\rho_0)S_0Ke(t)\cdot\Gamma_{n(N)}^T H_0 e(t)] \quad \mathbf{0}_{1\times n(N)}\right],$$

and $\overline{\mathbf{R}}^{n(N)}$ *is defined in* (2.27) *with* φ_t^n *defined in* (2.29)*.*

Proof. See Appendix A.2. ■

Remark 2.4.2. Unlike open-loop case [89], the proposed closed-loop ARX-OE method cannot supply efficient estimates for the system. Specifically, the parameter covariance of the OE step will be dependent on the parameter covariance $\overline{\mathbf{R}}^n$ from the first high-order ARX modeling step. However, this method provides consistent estimates and is applicable to routine operating data. Although the ARX-OE method is similar to the asymptotic method (ASYM) approach proposed by Zhu [90], our approach mainly applies to routine closed-loop data without external excitations, since for process monitoring such data are the most common type in practice. These scenarios have certain unique problems, such as the informativeness of closed-loop data, that will be discussed in the next section.

Remark 2.4.3. A similar result is reported in Corollary 10 in [73] on asymptotic distribution of the parameter estimates under direct identification with orders of noise model tend to infinity. It is shown that direct identification with current noise model yields minimal covariance on parameter estimates. Investigations on the possible links between these two results will be a promising future direction and this will provide

valuable insights to the interpretation of (2.31).

2.5 Identification based on routine operating data

Most on-line process monitoring tasks, e.g., MPM detection for MPC, require closed-loop identification based on routine operating data where external excitation signals may not exist. In this section, we discuss several important aspects of applying the above ARX-OE method in this situation.

2.5.1 Estimate of the controller inverse

It is well-known that if there are no external excitations, nonparametric closed-loop identifications (e.g., spectral analysis method) may result in an estimate of the inverse of controller. This is due to the possibility of relating input-output data through the feedback instead of through the process and noise models. In particular, when $r(t) = 0$, (2.23)-(2.24) are equivalent to

$$y(t) = G_0(q)u(t) + H_0(q)e(t), \tag{2.32}$$

$$u(t) = -K(q)y(t). \tag{2.33}$$

The modeling error of estimating G_0 is always larger than zero, while the modeling error of estimating $-1/K(q)$ between $y(t)$ and $u(t)$ is zero. Thus nonparametric methods will take the controller inverse as an estimate of the process since the corresponding prediction error is the minimum. One solution to this issue is to impose time-delay to the identification method where a large time-delay will help prevent yielding the inverse of controller as the process model estimate. A number of delay estimation approaches using closed-loop data are available in the literature (refer to [91], [92]). Time-delay estimation is a necessary step before performing the closed-loop ARX-OE identification method. For our paper machine examples in the simulation section, time-delay is assumed to be available and large enough to avoid estimating controller inverse as the process model estimate.

2.5.2 Sufficient excitation

It has been shown in the literature (e.g., [93]) that for a linear closed-loop system without any external excitations, its identifiability is related to the order of regulator and time-delay. Specific conditions on the

closed-loop identifiability are investigated in [93] and [94]. It is concluded that a complicated controller and a large time-delay will enrich the informativeness of closed-loop data. Thus nonlinear controllers are favored from this perspective. Fortunately, for most industrial processes (e.g., the paper machine) controlled by MPC, routine input-output data is generally sufficiently exciting (i.e., contains sufficiently many nonzero frequency components in the spectra) to apply the above ARX-OE method, especially when the MPC operates with active constraints.

2.5.3 The role of noise

For most closed-loop identification methods relying on external excitations, such as the indirect identification method, two-stage method and projection method, the presence of noise inflates the variance of the associated parameter estimates. However, for the direct identification method, it is proved in [73] that the noise can indeed reduce the variance of parameter estimates (refer to Corollary 10 in [73]). This argument also applies to the situation of implementing our ARX-OE identification method to the routine operating data in which noise is the only external signal. Moreover, in this case, large noise may trigger the constraints in MPC and thus renders the controller to be nonlinear, which in general enriches the informativeness of closed-loop data.

2.6 Examples

In this section, we provide one SISO example and one MIMO example from a paper machine to verify the proposed closed-loop ARX-OE identification method.

2.6.1 Case I: univariate MD control of the paper machine

We begin by studying a SISO process from the machine direction. For this particular MD process, the valve of thick stock pump is manipulated to alter the amount of pulp slurry provided to the headbox, which ultimately is used to control the basis weight of the paper sheet being produced. The true process has the following first-order model

$$G_0(s) = \frac{1.0545}{50s+1}e^{-80s}.$$

The sampling interval is 5 seconds and the discretized process model is shown to be

$$G_0(q) = \frac{b}{1+aq^{-1}}q^{-17},$$

Table 2.1: Tuning parameters of the SISO MD MPC

Tuning parameters	Values	Tuning parameters	Values
Actuator movement weight	0.01	Actuator deviation weight	0
CV target value	23.75 $lbs/3000ft^2$	MV target value	131 gpm
Prediction horizon	40	Control horizon	4
CV target weight	1	MV target weight	1
CV min-max weight	1	MV min-max weight	1
Bounds of MV	[0 3000]	Limit of MV movement	0.1667

where $b = 0.1003$, $a = -0.9048$. The controller employed is MPC with tuning parameter specifications shown in Table 2.1. The true noise model is chosen as

$$H_0(q) = \frac{1-0.9q^{-1}}{1+0.9q^{-1}}e(t),$$

where $e(t)$ is white noise with zero mean and variance $\sigma_e^2 = 0.01$. In this simulation, we assume that there is no MPM. To verify the effectiveness of the proposed closed-loop ARX-OE algorithm with routine operating data, we leave the setpoint unchanged during the entire simulation, i.e., the noise is the only external signal into the system. To avoid obtaining the inverse of controller, we assume that the true process delay is available and has been specified to the identification algorithm. With above settings, the simulation of closed-loop system lasts for 15 hours (10800 samples of input-output data). Input and output data from the simulation is shown in Figure 2.1 below.

To more accurately identify the noise model we test scenarios with different ARX model orders in the first step of the ARX-OE algorithm. Note that here we use *na* and *nb* to denote the orders of $A(q,\eta_n)$ and $B(q,\eta_n)$ in (2.8), respectively. Figure 2.2 shows the comparison between true and estimated IR coefficients of the inverse noise model. We can see clearly that for this slow decaying inverse noise model, high-order ARX can better capture those IR coefficients. Figure 2.3 demonstrates the step responses of our estimated process model under different ARX orders. All three situations give high-quality process model estimates from their comparison with the true step response. The estimated gain and time constant pairs from these three cases are $[0.0975\ -0.9114]$, $[0.1033\ -0.907]$, and $[0.1036\ -0.9084]$, respectively. We can see that the estimated parameters from the scenario with $na = 30,\ nb = 30$ are closer to the true values, even though the step responses in these three situations are almost identical. Notice that in order to acquire smoothly decaying IR coefficients in the first step, we added a regularization term to the least-squares estimation. Another benefit of using the regularization term is that it can avoid overfitting caused by the large number of

parameters in the first step.

To further illustrate the effectiveness of the proposed closed-loop identification method, we perform 1000 Monte-Carlo simulations with the closed-loop MD process above. For simplicity, we only consider the case $na = 30,\ nb = 30$. In each Monte-Carlo simulation we collect 15 hours of data. The proposed closed-loop ARX-OE method is applied to each data set and the estimates of parameters b and a are recorded. The histograms of estimates for b and a are demonstrated in blue bars in Figure 2.4 and Figure 2.5, respectively. The corresponding fitted normal curves are shown in the blue line. We can see that both parameter estimates have an approximate normal distribution. The mean values in both histogram plots are close to the true parameter values and this indicates that the proposed method can give consistent estimates. Furthermore, as a comparison, we apply the closed-loop direct identification method with correct and wrong specifications of the noise model order. For the latter case, we choose the noise model to have first order in the denominator and zero order in the numerator (and thus we expect biased estimates in a and b). In Figures 2.4 and 2.5, the green and red bars illustrate the histograms of parameter estimates from direct identification method with correct and wrong noise model structure, respectively. The green and red curves are the corresponding fitted normal curves from the histograms. As expected, the direct identification with correct noise model structure gives an unbiased estimate whereas with wrong noise model specification it gives a biased estimate. In practice, *a priori* knowledge of the noise model structure is often unavailable and thus the proposed closed-loop ARX-OE method shows great advantages under this circumstance compared with the direct identification method. Note that in this Monte-Carlo simulation we did not introduce any external excitation and thus it resembles the routine operating stage of industrial processes.

2.6.2 Case II: multivariate MD control of the paper machine

In this example, we consider a MIMO MD process in the paper machine. For this process, one stock flow and two steam flows (Steam4 and Steam3) are manipulated to control three properties of the paper sheet, i.e., weight, press moisture and reel moisture. It is important to note that there exist extensive interactions among these variables. Specifically, changing the stockflow will affect all three CVs. Also, the two steam variables have a coupling effect on the press and reel moisture. However, the influence on the weight caused by two steam flows can be considered negligible and thus the internal interactions among these variables can

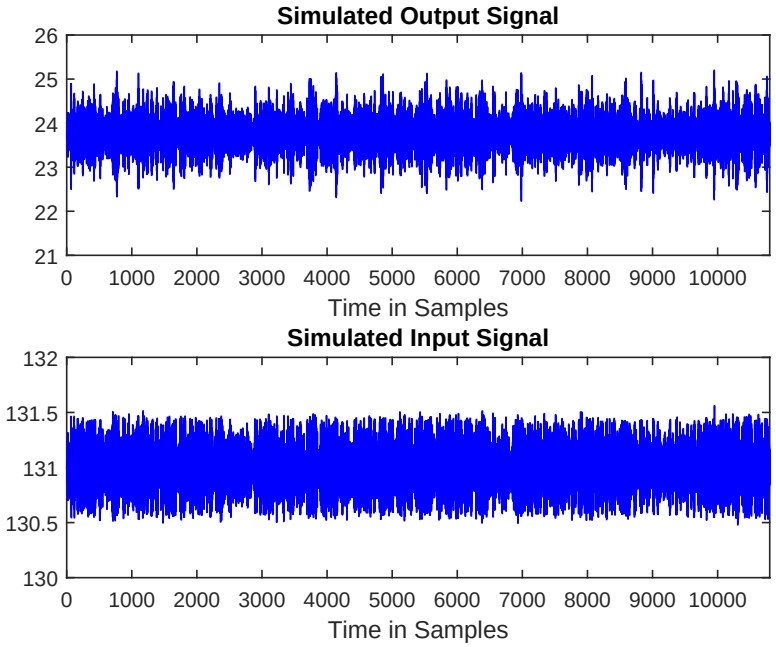

Figure 2.1: Simulated input and output data for the closed-loop MD process

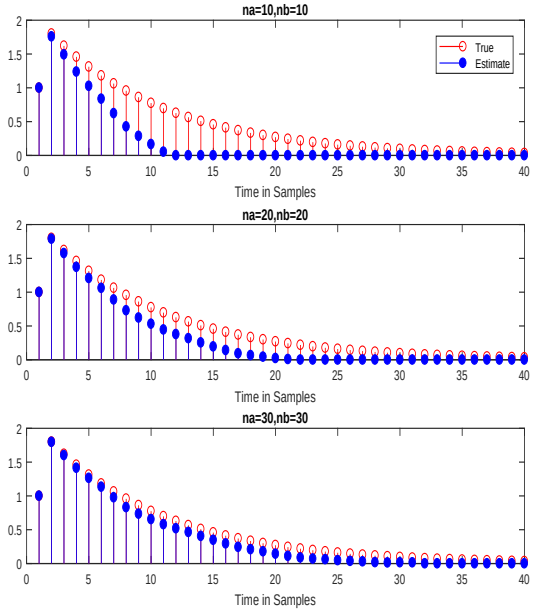

Figure 2.2: IR coefficients of the estimated noise model inverse with different ARX orders

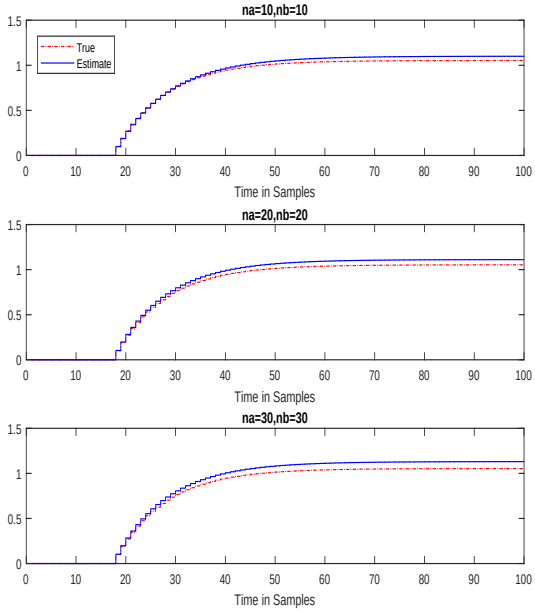

Figure 2.3: Step response of the estimated process model with different ARX orders

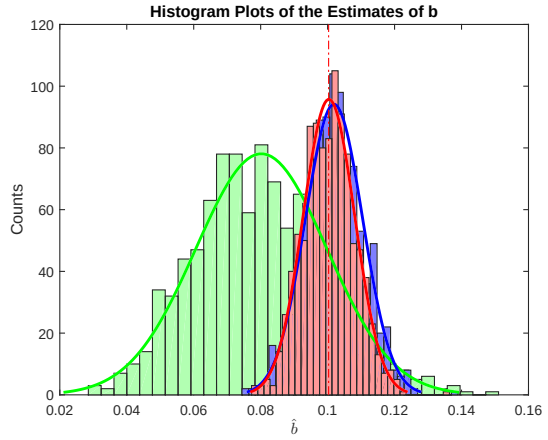

Figure 2.4: Histogram of parameter b estimates in 1000 Monte-Carlo simulations. Green: direct identification method with wrong noise model structure. Red: direct identification method with correct noise model structure. Blue: closed-loop ARX-OE method. Red dashed line: the true parameter value.

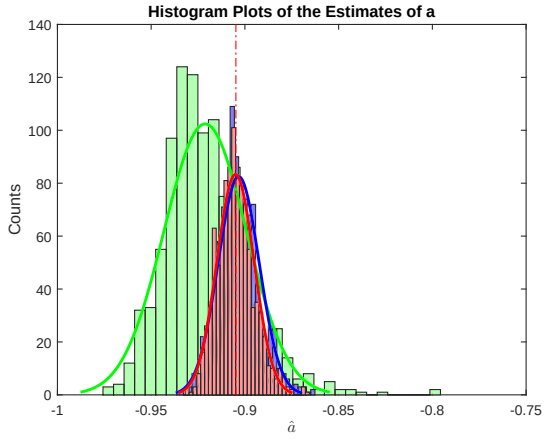

Figure 2.5: Histogram of parameter a estimates in 1000 Monte-Carlo simulations. Green: direct identification method with wrong noise model structure. Red: direct identification method with correct noise model structure. Blue: closed-loop ARX-OE method. Red dashed line: the true parameter value.

be modeled by a lower triangular transfer function matrix. We have the following MIMO MD process model

$$\begin{bmatrix} y_1(t) \\ y_2(t) \\ y_3(t) \end{bmatrix} = \begin{bmatrix} \frac{1.0545}{66.66s+1}e^{-72s} & 0 & 0 \\ \frac{0.2960}{46.02s+1}e^{-90s} & \frac{-0.14}{270.00s+1}e^{-114s} & 0 \\ \frac{0.7530}{154.80s+1}e^{-42s} & \frac{-0.2380}{211.20s+1}e^{-30s} & \frac{-0.0555}{24.84s+1}e^{-90s} \end{bmatrix} \begin{bmatrix} u_1(t) \\ u_2(t) \\ u_3(t) \end{bmatrix},$$

where the three CVs $y_1(t)$, $y_2(t)$ and $y_3(t)$, are weight, press moisture and reel moisture, respectively. The three MVs $u_1(t)$, $u_2(t)$ and $u_3(t)$, correspond to stockflow, Steam4 and Steam3, respectively. In this simulation, the selected sampling interval is 5 seconds and the above process model is discretized for controller design. We have the discretized process model (denoting $\mathbf{G}_0(q)$ as the transfer matrix)

$$\mathbf{G}_0(q) = \begin{bmatrix} \frac{0.07627}{1-0.9277q^{-1}}q^{-15} & 0 & 0 \\ \frac{0.03047}{1-0.897q^{-1}}q^{-19} & \frac{-0.002569}{1-0.9817q^{-1}}q^{-23} & 0 \\ \frac{0.02393}{1-0.9682q^{-1}}q^{-9} & \frac{-0.005568}{1-0.9766q^{-1}}q^{-7} & \frac{-0.01012}{1-0.8177q^{-1}}q^{-19} \end{bmatrix}.$$

For the noise model, we suppose that the noise sequences in three output channels are mutually independent, with the noise model as

$$\mathbf{d}(t) = \begin{bmatrix} \frac{1-0.5q^{-1}}{1+0.5q^{-1}} & 0 & 0 \\ 0 & \frac{1-0.3q^{-1}}{1+0.6q^{-1}} & 0 \\ 0 & 0 & \frac{1+0.2q^{-1}}{1+0.7q^{-1}} \end{bmatrix} \begin{bmatrix} e_1(t) \\ e_2(t) \\ e_3(t) \end{bmatrix},$$

where three noise sequences have the same variance, $\sigma_e^2 = 0.1$. For the ensuing discussion, we use $G_{ij}(q)$ and $H_{ij}(q)$ to represent the scalar transfer function located at the (i, j)-th position of $\mathbf{G}_0(q)$ and $\mathbf{H}(q)$, respectively. In this example, a multivariate MPC is used to control this MIMO process. The specific tuning parameters of the controller are illustrated in Table 2.2 above. The simulation duration of closed-loop MIMO MD system is set to 1150 minutes (13800 samples). The setpoint stays constant throughout the simulation and no external excitation is introduced. With current setup, the controller is very likely to work in a nonlinear mode. Therefore, closed-loop identification methods requiring a linear regulator will not be suitable in this situation. In the following content, we examine the effectiveness of our proposed method with MIMO closed-loop data, assuming that we have no *a priori* knowledge on the true noise model structure. To identify the process model, we apply the proposed method channel by channel. Each output channel is considered as a closed-loop multi-input single-output (MISO) system. A MISO high-order ARX model is first estimated by

$$A_i(q)y_i(t) = \sum_{j=1}^{i} B_{i,j}(q)u_j(t) + e_i(t), \quad i = 1,2,3, \tag{2.34}$$

where

$$A_i(q) = 1 + a_{i,1}q^{-1} + \ldots + a_{i,n}q^{-n}, \;\; B_{i,j}(q) = 1 + b_{i,j,1}q^{-1} + \ldots + b_{i,j,n}q^{-n},$$

giving rise to an estimate of the inverse noise model in the i-th output channel. Define $\hat{A}_i(q), \hat{B}_{i,j}(q)$ as the respective estimate of $A_i(q)$ and $B_{i,j}(q)$ from the above high-order ARX modeling step. We then apply the MISO OE identification after filtering the input and output signals using the obtained noise model estimate. Specifically, it follows that

$$y_i^f(t) = \sum_{j=1}^{i} G_{i,j}(q,\rho)u_j^f(t) + e_i(t), \quad i = 1,2,3,$$

Table 2.2: Tuning parameters of the MIMO MD MPC

Tuning parameters	Values	Tuning parameters	Values
Actuator movement weight	[0.01 0.01 0.01]	Actuator deviation weight	[0 0 0]
CVs target weight	[1 1 1]	MVs target weight	[1 1 1]
CVs min-max weight	[1 1 1]	MVs min-max weight	[1 1 1]
Actuator movement weight	[0.01 0.01 0.01]	Actuator deviation weight	[0 0 0]
Target value for CV1	174 $lbs/3000ft^2$	Target value for MV1	165 gpm
Target value for CV2	2.3 %	Target value for MV2	115 psi
Target value for CV3	6.2 %	Target value for MV3	35 psi
Prediction horizon	20	Control horizon	2
Upper bounds of MVs	[250 180 180]	Lower bounds of MVs	[0 0 0]
Limits of CV movement	[0.1 0.1 0.1]	Limits of MV movement	[0.2 1 1]

where

$$y_i^f(t) = \hat{A}_i(q)y_i(t), \;\; u_j^f(t) = \hat{A}_i(q)u_j(t).$$

The classic PEM can be applied to identify above MISO system. As before, we assume that the true time-delay for each channel is available. This assumption can be relaxed if external excitation signals are injected into the system or if the objective is not pursing a precise model estimate (e.g., MPM detection).

Figure 2.6 and Figure 2.7 show the simulated CV and MV profiles of the closed-loop MD process, respectively. The estimated and true IR coefficients of the inverse noise model are given in Figure 2.8. Clearly, the estimated coefficients are very close to true values, ensuring the reliability of using the estimated noise model for subsequent filtering operations. Figure 2.9 shows the step response comparison between the estimated and true process models. It is obvious from Figure 2.9 that the estimated process models are very close to the true ones. Specifically, we demonstrate explicitly the estimated process model $\hat{\mathbf{G}}(q)$ for further comparison as follows

$$\hat{\mathbf{G}}(q) = \begin{bmatrix} \frac{0.0769}{1-0.9270q^{-1}}q^{-15} & 0 & 0 \\ \frac{0.03062}{1-0.8916q^{-1}}q^{-19} & \frac{-0.002467}{1-0.9819q^{-1}}q^{-23} & 0 \\ \frac{0.02375}{1-0.9679q^{-1}}q^{-9} & \frac{-0.005639}{1-0.9760q^{-1}}q^{-7} & \frac{-0.009975}{1-0.0.8206q^{-1}}q^{-19} \end{bmatrix}.$$

Comparing $\hat{\mathbf{G}}(q)$ with the true process model $\mathbf{G}_0(q)$ one can see that the closed-loop ARX-OE identification provides accurate parameter estimates with routine operating data even though there are no external excitation signals. Therefore, the proposed method can be used for routine process monitoring purposes (e.g., real-time controller performance monitoring and MPM detection) that require online estimation of the

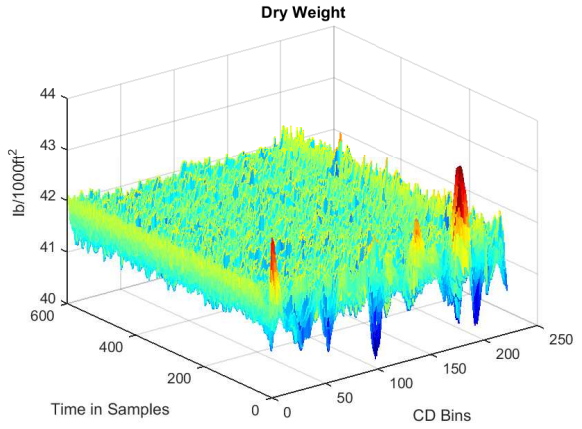

Figure 2.6: The simulated output profiles (CVs) for the MIMO MD process of a paper machine

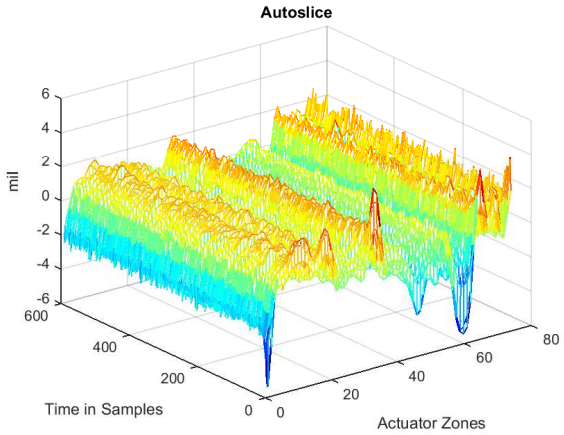

Figure 2.7: The simulated input profiles (MVs) for the MIMO MD process of a paper machine

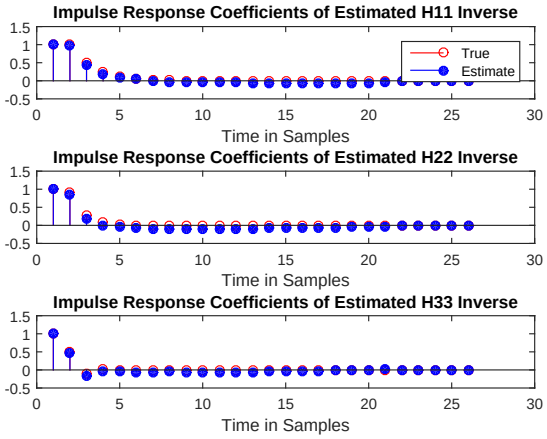

Figure 2.8: IR coefficients of the true and estimated inverse noise model for each output channel.

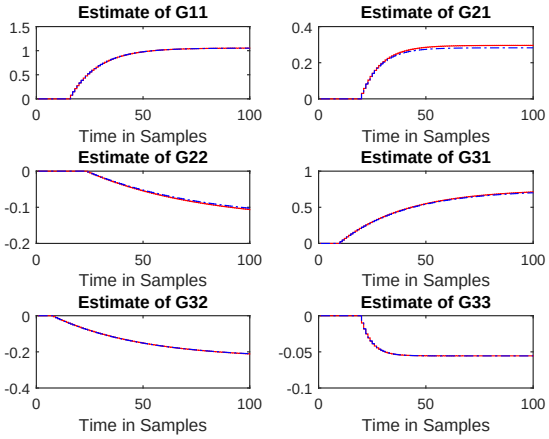

Figure 2.9: Step response of the true (red solid line) and estimated (blue dashed line) process models.

process model during routine operation.

2.7 Conclusion

This chapter presents a novel closed-loop identification method that can correct the bias inherent in the direct identification method due to insufficient specification of the noise model. First, a high-order ARX is identified to obtain an estimate of the noise model. In the second step, we filter input and output data by using the estimated inverse of noise model, and then perform an OE identification with filtered input-output data to obtain the process model estimate. It is shown that this closed-loop ARX-OE identification approach

can give consistent estimates and that the parameter estimator is asymptotically normally distributed. This method is applicable not only when the controller is nonlinear but also for the case where closed-loop data contain no external excitations. Therefore, this method exhibits great potential for purposes such as controller performance monitoring and MPM detection that require process model identifications based on routine operating data.

Chapter 3

Model-plant Mismatch Detection for MD Processes

3.1 Introduction

Model-plant mismatch (MPM) is the main source of control performance degradation in industrial MPCs. As mentioned in the previous chapters, an MPM detection scheme must not be sensitive to changes in the noise models since it may result in increased false alarms, and it should not require external perturbations as they will disturb normal operations of industrial processes. In this chapter, we propose a novel MPM detection approach that addresses these two challenges. Our idea is inspired by the historical data based benchmarks used in controller performance monitoring [95]. In those methods, to assess the control performance, process variable metrics under actual data are compared with those under a set of historical data which are collected during a period with satisfactory performance. Similarly, in our method, we partition routine operating data into a "training" stage (that we believe is generated with no MPM) and a "testing" stage. The training data serves as a benchmark against which we evaluate the presence of MPM in the test data. Specifically, we propose a novel method, based on closed-loop identification and support vector machine (SVM) classification, that can monitor MPM and noise change independently and thus can directly discriminate MPM from noise model change. The most striking benefit of our method is that it is suitable for situations where external excitations may not exist.

This chapter is outlined as follows. We begin in Section 3.2 by analyzing the drawbacks of several current methods for MPM detection. In Section 3.3, we elucidate the framework of the proposed MPM detection approach. Section 3.4 is devoted to developing a new closed-loop identification method that can provide consistent parameter estimates for the plant model based on the ARX-OE method in Chapter 2. In Section 3.5 we elaborate detailed procedures on training an SVM model based on the training data and implementing

it in the test data to examine the MPM and noise model change. An industrial example from the MD process of paper machines is provided to verify the proposed approach in Section 3.6, followed by conclusions in Section 3.7.

3.2 Drawbacks of several MPM detection methods

The minimum variance controller (MVC) benchmark has become one of the most popular tools in assessing controller performance due to its simplicity in computation and less required prior knowledge (only time-delay) of the process. However, as pointed out in previous sections, one pitfall of using MVC benchmark to detect MPM is that not only MPM but also disturbance changes can affect the performance metrics. It seems impossible to separate MPM from disturbance change by using the MVC benchmark. The rationale behind this conclusion is briefly outlined as follows.

Consider a SISO process under regulatory control (the setpoint is constant), where the process is denoted as $G(q) = q^{-d}\tilde{G}(q)$. Notice that d is the time delay and $\tilde{G}(q)$ is the delay-free plant. Define the controller to be $K(q)$. Suppose that the output noise is a filtered white noise with a noise model $H(q)$ and that $e(t)$ is a Gaussian white noise. The closed-loop transfer function from the noise $e(t)$ to the output $y(t)$ is then

$$y(t) = \frac{H(q)}{1+q^{-d}\tilde{G}(q)K(q)}e(t). \tag{3.1}$$

From the Diophantine decomposition of $H(q)$ we have

$$H(q) = \underbrace{h_0 + h_1 q^{-1} + \ldots + h_{d-1}q^{-(d-1)}}_{F(q)} + Rq^{-d}, \tag{3.2}$$

then the closed-loop transfer function (3.1) is further written as

$$y(t) = F(q)e(t) + L(q)e(t-d), \tag{3.3}$$

where $L(q) = \frac{R - F\tilde{G}K}{1+q^{-d}\tilde{G}K}$ is a proper transfer function, dependent on the controller. Here the argument q is omitted for simplicity of notations. The basic idea of the MVC benchmark is to consider $F(q)e(t)$ as a controller-invariant part and the minimum output variance is achieved by choosing a suitable controller (which is MVC) such that the second term $L(q)e(t-d)$ vanishes. Thus the theoretically minimal output

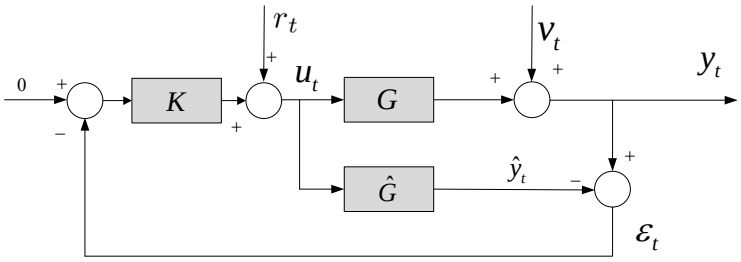

Figure 3.1: The IMC structure

variance will be the same, regardless of the implemented controller, as long as the disturbance model is unchanged. The actual controller performance is evaluated by the ratio

$$\eta = \frac{var[F(q)e(t)]}{var[y(t)]}. \tag{3.4}$$

If η is close to 1 then it indicates good control performance as the underlying controller is acting to achieve the minimal output variance. From (3.3) and (3.4) it is straightforward to find that if the disturbance model $H(q)$ changes, then η will be affected and will be no longer valid for the performance monitoring. Therefore, using the MVC benchmark (3.3) to detect MPM might be misleading and a more reliable approach insensitive to disturbance changes is necessary.

Another family of methods in detecting model-plant mismatch is based on system identification theory. A straightforward idea is to directly identify the process model online and compare it with the initial model used by the controller. Any significant discrepancy between them is then regarded as a model-plant mismatch. This idea requires that the identification method give a reliable estimate of the process model with the presence of feedback and with routine operating data in which external dither signals may not exist. Among all well-developed system identification methods the direct identification can fulfill this demand. But the condition for a consistent estimate is that the closed-loop data has to be informative enough and the selected process and disturbance model structures are flexible enough to contain the true model. The informativeness issue might be resolved if the controller is complex enough and most actual MPCs in industrial processes generally can satisfy this requirement. However, the noise model structure issue is difficult to address since it is not straightforward to acquire *a priori* information on the structure of a practical noise model and misspecification of the noise model often leads to a biased estimate of the process model.

Another approach is to use process variables in the internal model control (IMC) structure (see Figure

3.1) to identify the mismatch model $\Delta(q) = G(q) - \hat{G}(q)$. From IMC, one can easily verify the following closed-loop relationships among process variables (considering SISO case):

$$\varepsilon(t) = \frac{\Delta K}{1+\Delta K} r(t) + \frac{1}{1+\Delta K} v(t), \tag{3.5}$$

$$u(t) = \frac{K}{1+\Delta K} r(t) - \frac{K}{1+\Delta K} v(t), \tag{3.6}$$

where $\varepsilon(t)$ is the output error (or model residual), $u(t)$ is the process input, $r(t)$ is the dither signal and $v(t)$ is the output disturbance. Note that $v(t)$ is assumed to be filtered white noise, $v(t) = H(q)e(t)$ and $e(t)$ is Gaussian white noise. $H(q)$ is assumed to be stable, monic and of minimum phase. It is obvious that if dither signal is sufficiently exciting (notice that $\{r(t)\}$ and $\{v(t)\}$ are independent), the mismatch $\Delta(q)$ can always be factored out from (3.5)-(3.6). If there is no dither signal, i.e., $r(t) = 0$, the transfer function between $\varepsilon(t)$ and $u(t)$ is further shown to be

$$u(t) = -\frac{1}{K}\varepsilon(t). \tag{3.7}$$

Thus without external excitation it is impossible to determine the mismatch model by identifying the transfer function between $u(t)$ and $\varepsilon(t)$. Indeed the identified result is always the inverse of the controller. In this work we propose a novel closed-loop identification method that is able to identify the process and noise models using routine operating data. These models are further used by the proposed mismatch detection scheme.

3.3 The MPM detection idea

We mention first that the noise model change detection follows the same course as the MPM detection in our method. So in subsequent sections, our attention is mainly on introducing the MPM detection approach. The proposed method is based on a novel closed-loop identification algorithm which is capable of providing unbiased estimates for the process models with routine operating data, albeit with large variance. The inevitable variance associated with process model estimates impedes us from directly comparing our results with nominal models to identify the mismatch. In other words, discrepancies between the model estimates and the true plant can not always be blamed on the MPM and they may simply be an artifact of the variance in the estimates. Thus we have to form a reasonable uncertainty bound around the estimated process model due to the variance of parameter estimates. Models outside this uncertainty range are regarded as mismatched

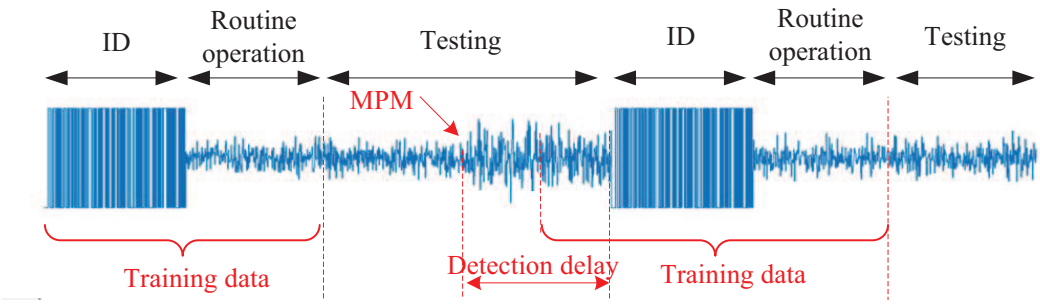

Figure 3.2: Illustration of the training and testing data (ID stands for identification).

models. Such an uncertainty range can be naturally captured by using the SVM technique. Note that to synthesize all possible mismatch situations (e.g., gain mismatch and time constant mismatch) with an overall metric, we would represent process model estimates in the FIR form. With a high order FIR model we can capture the process dynamics of any order model. Now the problem of detecting MPM can be reduced to that of checking if the estimated FIR coefficients are "equal to" the FIR coefficients of the current model. However, comparing the high dimensional FIR coefficient vectors is non-trivial and it forms the motivation for using SVMs.

Fig. 3.2 demonstrates the proposed approach to detect the MPM. The industrial data is split into training data and testing data. The training data is collected during a time interval in which the MPM is absent, e.g., the period during or right after the identification stage, as shown in the above figure. Notice that our algorithm is in the form of moving windows and the amount of training data can be properly selected according to the window size. For each window, we apply closed-loop ARX-OE identifications to obtain an estimate of the process model. With a set of estimated process models from moving windows in the training data, a one-class SVM is trained which can be interpreted as an appropriate boundary encompassing this set (see blue curves in Fig. 3.3- 3.4). Any model inside this boundary is considered as normal, indicating the absence of MPM. For the testing data, a similar moving window is applied and each process model estimate obtained is examined by the SVM model to predict whether it is located inside the boundary. If so, the SVM returns a positive score, implying no MPM and otherwise, it returns a negative score to indicate the presence of MPM in the current moving window. To be cautious in triggering an identification experiment, the MPM alarm is not raised until we gather a large number of negative scores. Note that the entire training and testing operations are carried out with routine operating data free of external excitations. In the following sections we focus on the closed-loop identification as well as SVM training and testing.

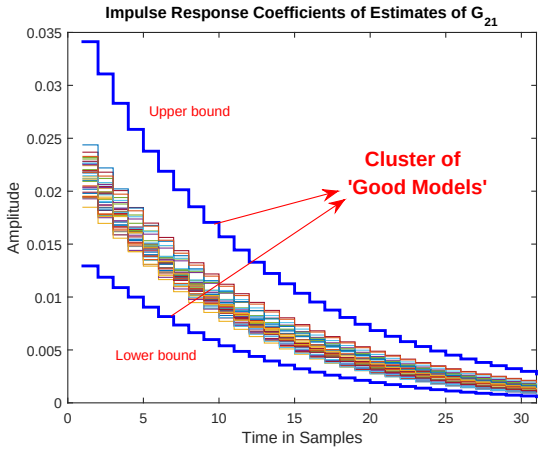

Figure 3.3: Illustration of the SVM training. Each curve shows the IR coefficients of the estimated models from training data. The upper and lower bounds define the width of the cluster.

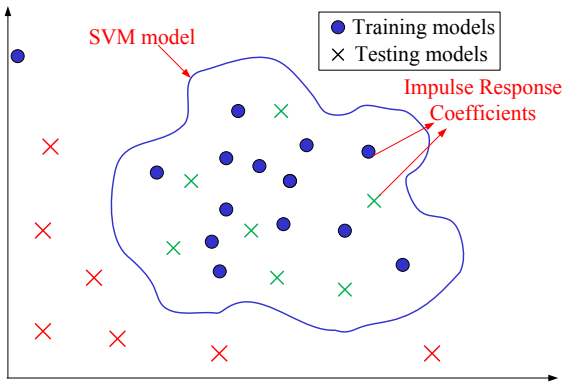

Figure 3.4: Illustration of the MPM detection idea. Here the training and testing models refer to the process model estimates from training and testing data sets.

3.4 Closed-loop identification

From the explanations above we can see that closed-loop identification plays a fundamental role in determining the performance of our proposed MPM detection algorithm. In this section, we apply the proposed ARX-OE method in Chapter 2 to routine operating data to obtain process and noise model estimates. Sufficient conditions guaranteeing the informativeness of routine closed-loop data are provided.

Consider the SISO Box-Jenkins model (2.1) and the controller in (2.2). It should be noted that a persistently exciting dither signal can always guarantee that the closed-loop data is informative, regardless of the controller orders. However, without external excitations, for *linear* controller to achieve the informativeness requirement, the following relationship must be satisfied for Box-Jenkins models [93]:

$$\max(n_x - n_f, n_y - n_b) \geq n_d + \min(n_x, n_f), \tag{3.8}$$

where n_x and n_y are numerator and denominator orders of the linear controller, respectively. n_b and n_f stand for the orders of polynomials in the process model numerator and denominator, respectively. n_d denotes the order of numerator polynomial in the noise model. One observation from (3.8) is that more complex controllers and a larger time-delay often imply richer information in the closed-loop data [86]. Additionally, if the controller is nonlinear, as is the case of MPC, the closed-loop data is generally sufficiently exciting for relevant system identifications [15]. Another benefit of a nonlinear controller is that it can prevent the

identification algorithm from returning an estimate of controller inverse. Moreover, we assume that the true time-delay is known *a priori* and is specified to the identification algorithm [2].

Following the main closed-loop ARX-OE identification algorithm presented in Chapter 2, we have the following theorem regarding the parameter estimate $\hat{\rho}_N$.

Theorem 3.4.1. *Consider the true Box-Jenkins model for the plant* (2.1) *as well as the equivalent high-order ARX form* (2.6)*. Assume that conditions in Theorem 2.4.1 hold and that the plant model is correctly parameterized. Then the parameter estimate* $\hat{\rho}_N$ *from the closed-loop ARX-OE identification method is consistent, i.e., we have*

$$\hat{\rho}_N \to \rho_0, \ \ \textit{w.p.1, as } N \to \infty, \tag{3.9}$$

where ρ_0 *is the true parameter value of* G_0 *if the condition* (3.8) *is satisfied for high-order ARX model* (2.6)*. Moreover, the estimated parameter value* $\hat{\rho}_N$ *is asymptotically Gaussian distributed with mean value* ρ_0*.*

Proof. (Outline) Define

$$\varepsilon(t,\rho) := [G_0 - G(q,\rho)]u(t) + \frac{1}{A(q,\eta_0)}e(t),$$

and

$$\begin{aligned} V_N(\rho,\hat{\eta}_N) &:= \frac{1}{N}\sum_{t=1}^{N}\frac{1}{2}[A(q,\hat{\eta}_N)\varepsilon(t,\rho)]^2, \\ V_N(\rho,\eta_0) &:= \frac{1}{N}\sum_{t=1}^{N}\frac{1}{2}[A(q,\eta_0)\varepsilon(t,\rho)]^2. \end{aligned}$$

Due to Theorem 2B.1 in [15] and Lemma 2.3.1, we have

$$V_N(\rho,\hat{\eta}_N) \to \overline{V}(\rho,\eta_0), \ \ \text{w.p.1, as } N \to \infty,$$

where $\overline{V}(\rho,\eta_0) := \overline{\mathbb{E}}\frac{1}{2}[A(q,\eta_0)\varepsilon(t,\rho)]^2$. Applying Parseval's theorem yields

$$\overline{V}(\rho,\eta_0) = \frac{1}{4\pi}\int_{-\pi}^{\pi}|G_0(e^{j\omega}) - G(e^{j\omega},\rho)|^2\frac{\Phi_u(\omega)}{|H_0(e^{j\omega})|^2}d\omega + \sigma^2.$$

[2] It will be shown shortly that knowing the true time-delay is an excessively strong requirement for the proposed MPM detection method. In fact, a prior knowledge for time-delay (might be wrong) is enough for the purpose of MPM detection.

Therefore, if $G(q,\rho)$ is correctly parameterized and closed-loop data is informative enough for selected model structures, we can conclude that (3.9) is valid. The proof for the Gaussian distribution of $\hat{\eta}_N$ follows the lines of Theorem 9.1 in [15] and is thus omitted here. ■

Remark 3.4.1. Despite the premise on the correct parameterization of $G_0(q)$ in Theorem 3.4.1, it is not supposed to be a restrictive limitation on the proposed closed-loop identification method. As will be shown in the following section, the SVM in MPM detection is trained and tested on the FIR form of $G(q,\hat{\rho}_N)$. Thus using an FIR model in the OE identification step, if *a priori* information about $G_0(q)$ is not accessible, is suggested in such cases to eliminate the bias.

Note that the explicit expression of the variance of $\hat{\rho}_N$ is non-trivial. It is thus recommended to use a set of training data from which we can obtain a collection of process model estimates as an approximation to the variance of transfer function estimates.

3.5 MPM detection

Before delving into the MPM detection algorithm, let us briefly review the SVM technique.

3.5.1 One-class learning support vector machines

SVM is a well-known binary classification technique. The idea behind a two-class SVM is to choose a hyperplane in the data space to separate two distinct classes of data. However, for linearly separable data, there are typically infinitely many hyperplanes that are able to discriminate the two classes. The SVM seeks the one that not only separates the two groups but also maximizes its geometric distance (known as the margin) to either class [96]. Therefore, the SVM is essentially an optimal separating hyperplane in the sense of robustness by significantly reducing the false classifications if other separating hyperplanes were used.

Suppose we are given a set of training data

$$\{\mathbf{x}_1,\ldots,\mathbf{x}_l\},\ \ \mathbf{x}_i \in \mathscr{X} \subset \mathbb{R}^r, \tag{3.10}$$

and the corresponding (binary) labels $\{y_1,\ldots,y_l\}$, where l stands for the number of data points. r is the dimension of input space $\mathscr{X}$ that the training data are located in. As the data are grouped into two classes, for convenience, we use $y_i = 1$ to denote the first class and $y_i = -1$ to denote the second class. A generic

two-class SVM training problem is formulated as [97]

$$\min_{\mathbf{w},b,\zeta} \quad \frac{1}{2}\|\mathbf{w}\|^2 + C\sum_{i=1}^{n}\zeta_i \tag{3.11}$$

$$s.t. \quad y_i(\mathbf{w}^T x_i + b) \geq 1 - \zeta_i,\ i = 1,\ldots,l, \tag{3.12}$$

$$\zeta_i \geq 0,\ i = 1,\ldots,l, \tag{3.13}$$

where $\mathbf{w} \in \mathbb{R}^r$ and $b \in \mathbb{R}$ are two parameters (slope and offset) characterizing a hyperplane. ζ_i, $i = 1,\ldots,n$, are nonnegative slack variables and C is a weight parameter to compromise between maximizing the margin and minimizing the training errors. Note that the presence of slack variables allows local violations of separating boundary determined by the hyperplane. This dramatically enhances the SVM's flexibility in treating nonseparable data sets. A major advantage of SVM in classifications, relative to other techniques, is the ease of generalization to incorporate kernel tricks. This operation is achieved by solving the dual problem,

$$\min_{\alpha} \quad \sum_{i=1}^{l}\alpha_i - \frac{1}{2}\sum_{i=1}^{l}\sum_{j=1}^{l}\alpha_i\alpha_j y_i y_j \kappa(\mathbf{x}_i,\mathbf{x}_j) \tag{3.14}$$

$$s.t. \quad 0 \leq \alpha_i \leq C,\ i = 1,\ldots,l, \tag{3.15}$$

$$\sum_{i=1}^{l}\alpha_i y_i = 0, \tag{3.16}$$

where α_i is the Lagrangian multiplier, and $\kappa(\cdot,\cdot)$ is the kernel function that will be explained in (3.18). The corresponding prediction function is shown as

$$p(\mathbf{x}) = \sum_{i=1}^{l}\hat{\alpha}_i y_i \kappa(\mathbf{x}_i,\mathbf{x}) + \hat{b}, \tag{3.17}$$

where $\hat{\alpha}$ and $\hat{b}$ are respectively the obtained Lagrangian multiplier and offset. It is easy to verify that the solution $\hat{\alpha}$ is sparse from KKT conditions. Those x_i corresponding to nonzero $\hat{\alpha}_i$ are known as support vectors. The sparsity of $\hat{\alpha}$ can significantly simplify the predictions in (3.17) as the summation only involves very few terms. The inclusion of a kernel function enables SVM to deal with nonlinear classifications.

As a convention, the SVM is developed particularly for binary classification problem. However, for the specific MPM detection problem, we use the set of process models from the training data as a reference group representing the behaviors of "no mismatch" process model cluster. The other group of data is ordinarily not

accessible since abnormal situations may occur in a variety of ways such as various parametric mismatches, irregular disturbances and so on. Thus the MPM detection is a one-class learning problem, which is also known as the "novelty detection problem".

The one-class learning SVM is depicted in the feature space, i.e., a space the data is mapped into. Consider the set of training data samples in (3.10). Prior to one-class SVM training it is necessary to map the data through $\Phi : \mathscr{X} \mapsto F$ into a (higher-dimensional) feature space F. The kernel function $\kappa(\mathbf{x},\mathbf{y})$ is such that the inner product in the feature space can be evaluated in the input space as

$$\kappa(\mathbf{x},\mathbf{y}) =< \Phi(\mathbf{x}),\Phi(\mathbf{y}) >, \ \ \forall \mathbf{x},\mathbf{y} \in \mathscr{X}. \tag{3.18}$$

A well-known kernel function that will be used hereafter is the Gaussian kernel

$$\kappa(\mathbf{x},\mathbf{y}) = e^{-\|\mathbf{x}-\mathbf{y}\|^2/c}, \tag{3.19}$$

where c is a parameter that is used to tune the sharpness of the Gaussian kernel function. It should be pointed out that with the Gaussian kernel function all data points in the feature space are located in the same orthant since $\kappa(\mathbf{x},\mathbf{y}) > 0$, $\forall \mathbf{x},\mathbf{y} \in \mathscr{X}$. Thus it is possible to find a hyperplane to separate the origin from the training data in the feature space with maximized margin. With this idea the one-class SVM training problem is formulated as [98]

$$\min_{\mathbf{w},\xi,b} \quad \frac{1}{2}\|\mathbf{w}\|^2 + \frac{1}{vl}\sum_{i=1}^{l}\xi_i - b \tag{3.20}$$

$$s.t. \quad \mathbf{w}^T\Phi(x_i) \geq b - \xi_i, \ \xi_i \geq 0, \tag{3.21}$$

where $\mathbf{w}$ and b represent the slope and offset of the hyperplane in feature space. The term $v \in (0,1]$ is a parameter tuning the upper bound of the fraction of outliers and lower bound of the fraction of support vectors. ξ is a slack variable allowing for local violations of the hard boundary determined by the hyperplane. Solving the optimization problem (3.20)-(3.21) can be converted into solving the following dual problem,

$$\min_{\alpha} \quad \frac{1}{2}\sum_{i,j=1}^{l}\alpha_i\alpha_j\kappa(\mathbf{x}_i,\mathbf{x}_j) \tag{3.22}$$

$$s.t. \quad 0 \leq \alpha_i \leq \frac{1}{vl}, \ \ \sum_{i=1}^{l}\alpha_i = 1. \tag{3.23}$$

It is obvious that while the primal problem is formulated in the feature space, its dual problem can be resolved in the input space by resorting to the kernel function. Thus we can avoid the intense computation arising from large dimensions of the feature space. Efficient algorithms are available in the literature to solve this dual problem. In the simulations presented in Section 3.6, we used sequential minimal optimization (SMQ) [98] to solve the dual problem above. A feature associated with the solution $\hat{\alpha}$ of dual problem is its sparsity, with most optimal dual variables $\hat{\alpha}_i$ valued at 0. Data points corresponding to nonzero optimal dual variables are known as support vectors and it is revealed that the optimal $\mathbf{w}$ and b (denoted as $\hat{\mathbf{w}}$ and $\hat{b}$, respectively) are completely determined by those nonzero optimal dual variables. Furthermore, with kernel function, the decision (or score value) function is also represented in the input space, instead of in the high-dimensional feature space, by the following,

$$p(\mathbf{x}) = \sum_{i=1}^{l} \hat{\alpha}_i \kappa(\mathbf{x}_i, \mathbf{x}) - \hat{b} \tag{3.24}$$

where $\mathbf{x}$ is a test example. Note that the sum in (3.24) typically involves $n_\alpha << l$ nonzero terms, where n_α is the number of nonzero dual variables. This allows for efficient evaluation. For a given test example $\mathbf{x}$, the value $|p(\mathbf{x})|$ represents the distance of $\mathbf{x}$ to the separating hyperplane. If $p(\mathbf{x}) > 0$, it means that $\mathbf{x}$ can be classified into the initial class. Otherwise $\mathbf{x}$ does not belong to that class. We note that the introduction of kernel functions significantly expands the flexibility of SVM in constructing separating boundaries, enabling it to generate a nonlinear classifier in the input space.

A critical issue in applying one-class SVM training strategy to MPM detection is the limited amount of training data available in industrial processes. Taking the paper machine as an example, grade changes (setpoint changes) often take place on a daily basis and thus training data has to be collected after each grade change to represent the current operating condition before carrying out MPM detection. Consequently, only a few process model estimates from training data are available to build an SVM model. In order to overcome this issue we use a resampling technique to enlarge the cluster of no mismatch models estimated from training data before performing the SVM training.

3.5.2 Resampling

The main principle we adopt here is to fit a probability density function (PDF) to each impulse response coefficient of the estimated process model. Then a large number of samples can be generated by sampling randomly from the estimated density function. More specifically, denote the FIR form of the estimated

process model $G(q,\hat{\rho}_N)$ in the k-th moving window as

$$G(q,\hat{\rho}_N^k) = \hat{g}_0^k q^{-d} + \hat{g}_1^k q^{-d-1} + \ldots + \hat{g}_m^k q^{-d-m}, \tag{3.25}$$

where m is a pre-specified number. Here $k = 1,2,\ldots,N_k$, are the indices of moving windows in the training data. It is straightforward that FIR coefficients $\hat{g}_i^k, i = 0,\ldots,m$, are asymptotically Gaussian distributed, given that $\hat{\rho}_N^k$ has an asymptotically Gaussian distribution (cf. Theorem 3.4.1). For each coefficient $\hat{g}_i^k$, several estimated values are obtained from moving windows in the training data. Then we can construct rough estimators for the mean and variance of each IR coefficient

$$\begin{aligned} \hat{\mu}_i &= \mu(\hat{g}_i^1, \hat{g}_i^2, \ldots, \hat{g}_i^{N_k}),\ i = 0,\ldots,m, \\ \hat{\sigma}_i^2 &= \sigma(\hat{g}_i^1, \hat{g}_i^2, \ldots, \hat{g}_i^{N_k}),\ i = 0,\ldots,m, \end{aligned}$$

where $\mu(\cdot)$ and $\sigma(\cdot)$ are some functions. One choice of these two functions is sample mean and sample variance. Due to the limited amount of training data (N_k normally is small), the estimated PDF for each FIR coefficient is much more conservative than the true PDF. Thus we use a parameter α to tune the width of the PDF to avoid this problem. The guidelines for selecting α are:

- If we have plenty of training data, α is small;
- If we have very few training data, α is large.

The rationale behind these guidelines is that more training data may give us a more precise and reliable estimate of the PDF and vice versa. The next step is to use the resampling idea to randomly generate a large number of samples of each FIR coefficient subject to the corresponding estimated PDF. Then a one-class SVM model can be developed from these enhanced samples for the initial cluster of "good" process models.

Remark 3.5.1. Note that the proposed SVM MPM detection approach relies on the training data and then detecting changes on the testing data. In practice, there is no prior knowledge on how severe an MPM might be. Thus determining the value of tuning parameter α shall be based on the anticipated sensitivity from practical demands. For example, if we require our approach to be able to detect only significant MPM but be robust to minor MPM, α shall be specified to a relatively large value and vice versa. Moreover, our approach can detect both abrupt and slowly drifting mismatches since our training data will be fixed once they are selected.

3.5.3 MPM detection with SVM

With the trained one-class SVM, we first need to estimate FIR coefficients of the process model identified from each moving window in the testing data, following the same procedures as previous sections. For estimated FIR coefficients, we apply the SVM model to predict whether they belong to the initial cluster. If so, the SVM returns a positive score value indicating that the current testing window does not display any sign of mismatch. Otherwise the SVM returns a negative score to signify the mismatch. However, to be cautious to start an identification experiment, the MPM alarm is not triggered until we have accumulated a sufficiently large number of mismatch reports. Specifically, define I_t as the sign of score value for time instant t

$$I_t = sign(p(\mathbf{x}_t)), \tag{3.26}$$

with $\mathbf{x}_t$ being the FIR coefficient vector of the plant model estimate for the window data at time t. Denote $T_t = \{t-n_T, \ldots, t-1, t\}$ where n_T is a detection interval, i.e., the number of previous moving windows under inspection to determine the existence of MPM. We further define an MPM indicator

$$s = \frac{|I_-|}{n_T}, \tag{3.27}$$

where $I_- := \{I_i = -1 : i \in T_t\}$ and $|I_-|$ is the number of elements in the set $|I_-|$. The user can specify a threshold s_T for the MPM indicator to raise an MPM alarm. We suggest a conservative s_T (e.g., $s_T = 0.95$) to be circumspect in raising the MPM alarm.

Remark 3.5.2. Note that the MPM detection method presented above can also be applied to the noise model estimate $A(q, \hat{\eta}_n)$ from the ARX-OE method to find the noise mismatch. In this manner we can monitor the process and noise models separately to distinguish MPM from noise model changes. We comment that while the controllers considered in this chapter are assumed to be tuned based solely on the plant model, in cases where controller tuning also depends on noise model (such as minimum variance control and some MPCs), detection of a noise model change can also be used to trigger an identification experiment. Moreover, if *a priori* information about the true process model structure is not available, we can specify it with an FIR structure to acquire consistent model estimates and the subsequent mismatch detection scheme is still applicable. The entire logic flow of MPM detection is shown in 3.5.

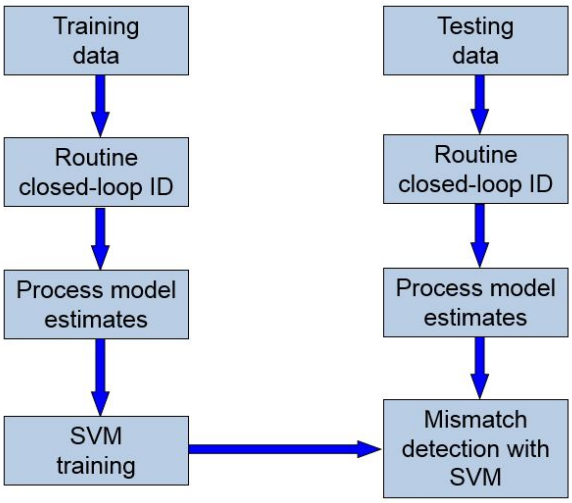

Figure 3.5: Flow chart of MPM detection scheme

3.6 Examples of MPM detections for MD processes

In this section we demonstrate the MPM detection algorithm through a SISO example in the MD process of paper machines. The CV is dry weight and the MV is stockflow. The sampling interval is set as 5 seconds. After discretization we obtain the true plant model

$$G_0 = \frac{0.1003}{1-0.9048q^{-1}}q^{-17}.$$

In the simulation of MD process the true noise model is selected as

$$H_0 = \frac{1-0.3q^{-1}}{1+0.6q^{-1}}.$$

We use an MPC as the MD controller. To reflect the reality of a paper machine's operating condition we set the standard deviation of noise to be $\sigma = 0.05$. The entire simulation lasts 15 hours without any setpoint change. During this simulation, initially there is no mismatch between the true plant and process model employed in MPC. After 7 hours we change the true noise model into

$$H_0 = \frac{1+0.3q^{-1}}{1-0.6q^{-1}},$$

Table 3.1: Parameters setup of the MPM detection algorithm

Parameters	Values	Note
W_{size}	2 hours	Moving window size
W_{step}	5 min	Moving window step size
n	9	Order of ARX model
T_{train}	3 hours	Duration of training stage
n_T	2 hours	Mismatch inspection interval
s_T	0.95	Mismatch threshold
α	1.5	Tuning the width of estimated PDF

to create a noise mismatch. Furthermore, we double the plant gain to introduce an MPM after 11 hours. The objective is to examine whether the proposed MPM detection algorithm is able to detect the process and noise model changes separately, with the collected routine operating data. We summarize configurations of parameters relevant to the MPM detection algorithm in Table 3.1. Note that we use the same window size and step size for both training and testing stages.

Fig. 3.6 depicts the simulated CV and MV profiles. Note that the first vertical red dash-dotted line indicates the time instant at which the noise change is introduced to the process. The second vertical line shows the time when we create an MPM. In plotting this graph we have removed the mean from the profiles. It is obvious that both the noise change and MPM bring significant variations to the profiles which are not favored since the control objective is to keep CV profiles as flat as possible. However, it is stressed that poor control performance from merely noise change should not trigger an identification experiment. We use the first 180 minutes of data as training data and the rest as testing data.

Fig. 3.7 demonstrates the detection results for both noise model change and MPM. Specifically, the first and third figures display the predicted SVM scores (cf. (3.24)) for noise and process model estimates, respectively. Clearly, the SVM scores drop to negative values after the corresponding noise model change occurs. The second and fourth plots track the mismatch indicator values s in (3.27) for both noise and process models. The red dash-dotted line highlights the specified threshold to raise an alarm. Ideally, a system identification experiment is triggered once the s value of the process model exceeds the threshold s_T. However, in this example we neglect the subsequent identification part and it will be more explicitly demonstrated in the following adaptive control chapters. From Figure 3.7 it is clear that the noise change at the 420th minute does not affect the prediction of MPM. Thus we may conclude that the proposed mismatch detection scheme is capable of monitoring the noise model change and MPM separately and thus is able to discriminate MPM from noise model change by using only routine operating data.

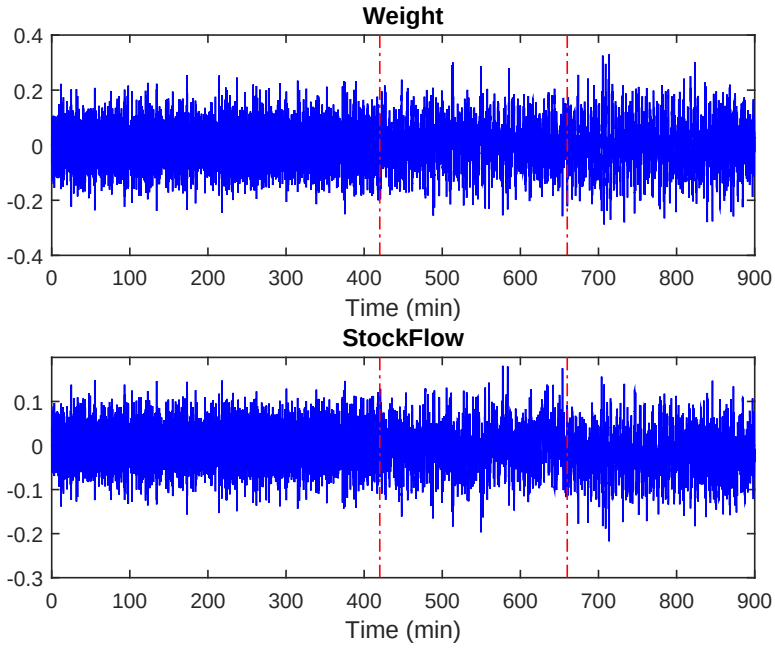

Figure 3.6: Simulated input and output profiles

3.7 Conclusion

This chapter presents a novel MPM detection algorithm that can separate MPM from noise model changes, relying only on routine operating data. To this end, we proposed a new closed-loop identification method that can give consistent parameter estimates for the process model without the need for any *a priori* information about the noise model. We split the mismatch detection problem into a training stage and a testing stage, and in the training stage an SVM model is developed based on the process model estimates. The trained SVM model is then used to detect MPM in the testing data. With the same procedures we can train another SVM model for noise models to detect noise model changes. This technique is tailored well enough to meet industrial demands on MPM monitoring. An example on paper machines is presented to illustrate the effectiveness of the proposed method.

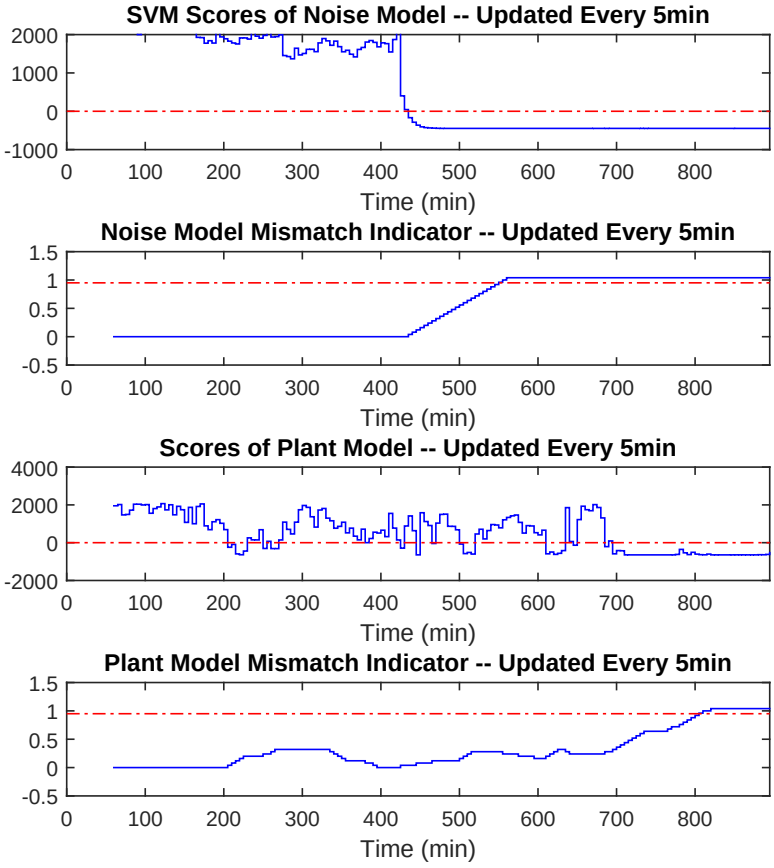

Figure 3.7: MPM and noise change detection results

Chapter 4

Control Performance Assessment for CD Processes

4.1 Introduction

Similarly to typical control loops, the CD process also suffers from the performance limitation due to time-delay in the dynamic model in temporal direction. In addition, the CD process has its unique performance limitations in the spatial direction which arise from the spatially-distributed nature of this large-scale process. An obvious fact regarding CD control is that the number of CD measurement bins is much greater than that of CD actuators, and this makes the CD process model matrix non-square. As a result, it becomes plausible that we are not able to find a CD controller to let the actuator array completely control all CD measurement bins. This non-square nature of CD process models forms the fundamental spatial performance limitation. Moreover, most CD process are ill-conditioned and the gains corresponding to high spatial frequency modes are small [12]. Thus for the sake of robust stability when model uncertainty is present, the controller normally does not exert any control action to compensate for high-frequency spatial disturbances, leaving them uncontrolled. In this sense it is appropriate to select the benchmarking CD controller as the one that allows for these CD performance limitations.

In this chapter we first derive the MVC benchmark for the CD process by studying both spatial and temporal fundamental performance limitations. However, MVC benchmark is rather aggressive since it represents an ideal performance limit for attenuating variations. In order to better reflect the performance of a practical controller, our next step is to build up a user-specified benchmark that not only accounts for above physical performance constraints but also considers the tuning status of implemented controllers. We may expect such user-specified benchmark to be a more suitable choice in monitoring the health of industrial processes.

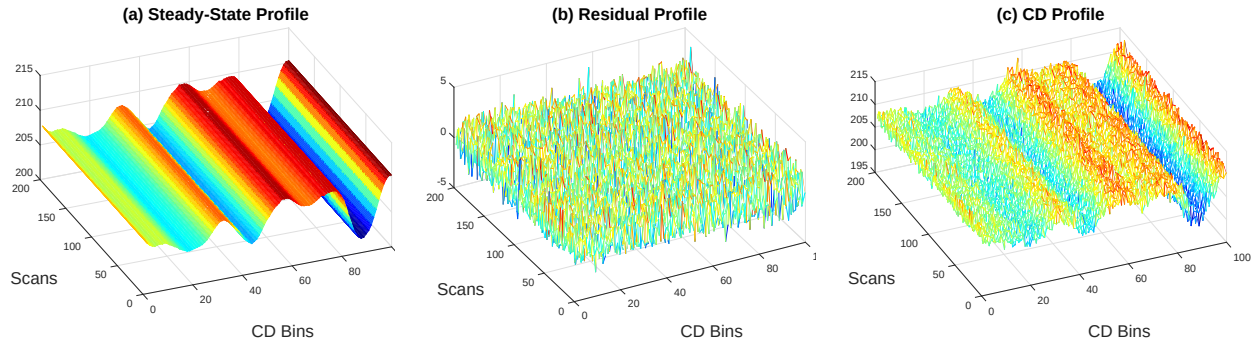

Figure 4.1: Illustration of the variation separation. (a): The steady-state profile plot. Note that the steady-state profile is replicated to have the same scan number as the residual profile and CD profile; (b): The residual profile plot. Each CD bin has zero mean; (c): The overall CD profile. Note that the CD profile is combined by the steady-state and the residual profile.

4.2 Preliminaries

4.2.1 Variance partition

A given data set $\mathbf{Y} \in \mathbb{R}^{m \times N}$ from a paper machine can always be separated into machine direction (MD), cross direction and residual components, where m is the number of measurement bins, and N is the number of scans in the data set. For details on the calculation and partitioning of variance, see Appendix B.1. In terms of CD control and CD performance monitoring, the MD variation is not taken into account. The data set without MD variation at time t is denoted as $\mathbf{y}(t) \in \mathbb{R}^m$ (CD profile), and we have

$$\mathbf{y}(t) = \mathbf{y}_{ss} + \mathbf{y}_r(t), \tag{4.1}$$

where $\mathbf{y}_{ss} \in \mathbb{R}^m$ is the steady-state profile, which is constant over all scans. $\mathbf{y}_r(t) \in \mathbb{R}^m$ is the residual profile and is changing over time. Figure 4.1 shows typical graphs of steady-state, residual and CD profiles. The process models for steady-state and residual profiles will be given in the following subsection, and the motivation to treat them separately will be presented in Section 4.5.

4.2.2 Process model

In traditional CD control, the steady-state performance is of great importance since most paper machines operate in regulatory mode at steady-state. The static steady-state model of a CD process is expressed as

$$\mathbf{y}_{ss} = \mathbf{G}\mathbf{u}_{ss} + \mathbf{v}_{ss}, \tag{4.2}$$

where $\mathbf{u}_{ss} \in \mathbb{R}^n$ is the steady-state manipulated variable, and n is the number of actuator zones. $\mathbf{G} \in \mathbb{R}^{m\times n}$ is the steady-state gain matrix. $\mathbf{v}_{ss}$ is the steady-state disturbance which refers to a deterministic disturbance persistently acting on the output, e.g., a spatial sinusoidal disturbance which is not changing over time. For the CD process, the overall disturbance is assumed to be a combination of the steady-state disturbance $\mathbf{v}_{ss}$ and a filtered white noise $\mathbf{v}_r(t)$, as shown in (4.3) below.

When considering only the residual profile, we have the following model,

$$\mathbf{y}_r(t) = g(q)\mathbf{G}\mathbf{u}_r(t) + \mathbf{v}_r(t), \tag{4.3}$$

where $\mathbf{y}_r(t) = \mathbf{y}(t) - \mathbf{y}_{ss}$ can be considered as the deviation of process output from the steady-state value due to stochastic disturbances. Similarly, $\mathbf{u}_r(t) = \mathbf{u}(t) - \mathbf{u}_{ss}, \mathbf{v}_r(t) = \mathbf{v}(t) - \mathbf{v}_{ss}$ are the deviations of manipulated variable and disturbance from their steady-state values, respectively. The output disturbance, $\mathbf{v}_r(t) \in \mathbb{R}^m$, is generally assumed to be filtered white noise. Note that the subscripts r in (4.3) stand for the residual. The scalar transfer function $g(q)$ in (4.3) can further be expressed as

$$g(q) = z^{-d}\frac{B(q)}{A(q)}, \tag{4.4}$$

where d stands for the time-delay and $B(q)$ and $A(q)$ are scalar polynomials. Similarly, the stochastic disturbance $\mathbf{v}_r(t)$ in (4.3) is filtered white noise assumed to be temporally and spatially separable, denoted as

$$\mathbf{v}_r(t) = \frac{C(q)}{A(q)}\phi\mathbf{e}(t), \tag{4.5}$$

where $C(q)$ and $A(q)$ are scalar polynomials describing the temporal filter while the constant matrix, ϕ, is used to represent the spatial filtering of the white noise vector $\mathbf{e}(t)$. The covariance matrix of white noise vector $\mathbf{e}(t)$ is assumed to be $\mathbb{E}[\mathbf{e}(t)\mathbf{e}^T(t_0)] = \Sigma_e\delta(t-t_0)$, where $\mathbb{E}$ is the expectation operator, Σ_e is the covariance matrix and δ is the Dirac delta function.

Remark 4.2.1. From the above description on steady-state and residual profiles, one can interpret each entry of the steady-state profile $\mathbf{y}_{ss}$ as the mean of the corresponding output channel (measurement bin). Each entry of the residual profile $\mathbf{y}_r(t)$ is the deviation of the profile from corresponding mean values.

4.3 The MVC benchmark for CD processes

In this section, the performance limitations for both steady-state model (4.2) and residual dynamic model (4.3) are illustrated. The MVC benchmarks for both models are developed analogously, and new performance indices are proposed based on these benchmarks.

4.3.1 MVC benchmark for the steady-state profile

For the steady-state model (4.2), the optimal control input $\mathbf{u}_{ss}$ which minimizes the output variance has the structure

$$\mathbf{u}_{ss} = -(\mathbf{G}^T\mathbf{G})^{-1}\mathbf{G}^T\mathbf{v}_{ss}, \tag{4.6}$$

involving the pseudo-inverse of the $\mathbf{G}$ matrix. It has been proved in [2] that if a controller has the structure (4.6) and an integrator in the dynamic part, then the steady-state output profile $\mathbf{y}_{ss}$ will contain no components in the column space of $\mathbf{G}$, which is regarded as the controllable subspace. If the $\mathbf{G}$ matrix is square and invertible, then the optimal input is able to achieve zero steady-state output. Therefore, the structure of the $\mathbf{G}$ matrix limits the performance of steady-state model (4.2). For a non-square $\mathbf{G}$ matrix with full rank, i.e., $rank\{\mathbf{G}\} = \min\{m,n\}$, the output $\mathbf{y}_{ss}$ with minimal variance is

$$\mathbf{y}_{ss} = [\mathbf{I} - \mathbf{G}(\mathbf{G}^T\mathbf{G})^{-1}\mathbf{G}^T]\mathbf{v}_{ss}. \tag{4.7}$$

In order to demonstrate the controller form which is able to achieve minimal steady-state variance, we assume that the controller $\mathbf{K}(q)$ has the following structure (refer to [2])

$$\mathbf{K}(q) = k(q)(\mathbf{G}^T\mathbf{G})^{-1}\mathbf{G}^T. \tag{4.8}$$

where $k(q)$ is the scalar dynamic part of $\mathbf{K}(q)$. From (4.8), the closed-loop sensitivity function is obtained as

$$\mathbf{y}(t) = [1 + g(q)\mathbf{G}\mathbf{K}(q)]^{-1}\mathbf{v}(t). \tag{4.9}$$

Using the singular value decomposition (SVD) of $\mathbf{G}$, (4.9) is further simplified as

$$\begin{bmatrix} \mathbf{y}_c(t) \\ \mathbf{y}_u(t) \end{bmatrix} = \begin{bmatrix} \frac{1}{1+g(q)k(q)} & 0 \\ 0 & \mathbf{I}_{(m-n)\times(m-n)} \end{bmatrix} \begin{bmatrix} \mathbf{v}_c(t) \\ \mathbf{v}_u(t) \end{bmatrix}, \tag{4.10}$$

where the subscripts c and u refer to spatially controllable and spatially uncontrollable signals, respectively. If $k(q)$ has an integrator, at steady-state, (4.10) will become

$$\begin{bmatrix} \mathbf{y}_{ss,c} \\ \mathbf{y}_{ss,u} \end{bmatrix} = \begin{bmatrix} 0 & 0 \\ 0 & \mathbf{I}_{(m-n)\times(m-n)} \end{bmatrix} \begin{bmatrix} \mathbf{v}_{ss,c} \\ \mathbf{v}_{ss,u} \end{bmatrix}. \tag{4.11}$$

It is clear that the MVC for the steady-state model (4.2) will completely remove all disturbance components within the controllable subspace. However, those disturbance components within the uncontrollable subspace will not be affected by the controller. Therefore, the spatially uncontrollable components $\mathbf{y}_{ss,u}$ can be used to develop the MVC benchmark. Note that the actual steady-state profile under a CD controller such as CD-MPC (not spatial MVC) may have components left in the controllable subspace.

4.3.2 MVC benchmark for the residual profile

For the residual profile, in the spatial direction, as with the steady-state case, due to there being more CD bins than actuator zones, i.e., $\mathbf{G}$ is not square, not all of the directions of $\mathbf{G}$ are controllable. This means that it is impossible to design a controller to reach zero error for a given disturbance. Therefore, the structure of $\mathbf{G}$ matrix contributes to the spatial performance limitation in the CD controller. In addition, the residual profile (4.3) also suffers temporal performance limitation due to the actuator dynamics. In the temporal direction, the time-delay forms a fundamental limitation on the controller design, upon which various types of delay compensators arise such as dead-beat controller, minimum variance controller, Dahlin controller, and so on.

For the disturbance model (4.5), from the Diophantine identity, we can decompose the prediction for time $t+d$ (at time t) as

$$\mathbf{y}_r(t+d|t) = \hat{\mathbf{y}}_{r,c}(t+d|t) + \underbrace{\hat{\mathbf{y}}_{r,u}(t+d|t) + F(q)\phi\mathbf{e}(t+d)}_{\text{controller-invariant}}, \tag{4.12}$$

where the subscript c and u stand for spatially controllable and uncontrollable parts of $\mathbf{y}_r(t+d|t)$, respec-

tively. Here the controllable subspace is defined as the column space of $\mathbf{G}$, as for the steady-state case. $F(q)$ is the first d terms after decomposition of $\frac{C(q)}{A(q)}$. The derivation of (4.12) is referred to Appendix B.2. It can be observed in (4.12) that the last two terms are controller-invariant, both spatially and temporally, parts of the profile, and hence can be used to define a benchmark for performance assessment. If the current controller being implemented is MVC, then the first term on the right hand side of (4.12) disappears.

Based on the proposed MVC benchmarks for both steady-state profile in (4.7) and residual profile in (4.12), a new MVC performance index for the CD process can be defined as

$$\eta_1 = \frac{trace\left[\sum_{i=0}^{d-1} \mathbf{F}_i \Sigma_e \mathbf{F}_i^T + \Sigma_{\hat{y}_{r,u}} + diag(\mathbf{y}_{ss,u}\mathbf{y}_{ss,u}^T)\right]}{trace\left(\Sigma_{y,mse}\right)}, \tag{4.13}$$

where $\mathbf{F}_i = f_i\phi$, $\Sigma_{\hat{y}_{r,u}}$ is the covariance matrix of the uncontrollable predicted profile $\hat{y}_{r,u}$, and $diag(\cdot)$ is a matrix formed by diagonal elements. The term in the denominator $\Sigma_{y,mse}$ is defined as

$$\Sigma_{y,mse} = \Sigma_{y_r} + diag(\mathbf{y}_{ss}\mathbf{y}_{ss}^T), \tag{4.14}$$

where Σ_{y_r} is the covariance matrix of the residual profile, each element on the diagonal represents the variance of an individual output channel of $\mathbf{y}_r$. $diag(\cdot)$ represents the operator of extracting the diagonal entries of a matrix into a diagonal matrix. For the term $diag(\mathbf{y}_{ss}\mathbf{y}_{ss}^T)$, each element stands for the corresponding mean deviation from zero of each individual output channel. In (4.13), the first term $\sum_{i=0}^{d-1} \mathbf{F}_i \Sigma_e \mathbf{F}_i^T$ in the numerator represents the covariance of unpredictable components in the residual profile. The second term $\Sigma_{\hat{y}_{r,u}}$ indicates the covariance of spatially uncontrollable predicted residual profile. The third term $diag(\mathbf{y}_{ss}\mathbf{y}_{ss}^T)$ stands for the spatially uncontrollable portion of steady-state profile. Thus the numerator of (4.13) specifies the measure of both residual MVC benchmark (4.12) and steady-state MVC benchmark (4.7). On the other hand, the denominator of (4.13) represents the overall mean square error (MSE) of the output profile. Hence, the new MVC performance index η_1 is the ratio between the covariance of benchmark of $\mathbf{y}(t)$ and its total variance (see Appendix B.1). If the implemented controller is MVC, the index η_1 will be equal to 1 as the measured output $\mathbf{y}$ only contains uncontrollable components, which are exactly the terms shown in the denominator of (4.13). Otherwise, η_1 will be less than 1. In general, a smaller value of η_1 implies worse control performance.

From the performance index in (4.13), we can see that one has to separate the spatially uncontrollable components $\hat{\mathbf{y}}_u(t)$ from $\hat{\mathbf{y}}(t)$ in (4.12) in order to evaluate the benchmark. Besides, this performance index

takes the spatially uncontrollable components into account. In industrial CD control systems, the spatially uncontrollable components of disturbances almost remain untouched. Therefore, we expect the performance index (4.13) to be sensitive to high-frequency spatial disturbances. If there is a great amount of spatially high-frequency disturbances (beyond the spatial bandwidth) present, the performance index (4.13) will be inflated by these high-frequency components, and therefore the performance index will be always close to one (this will be illustrated in the simulation part). In this case, the performance index η_1 becomes incapable of detecting the performance drop. An alternative is to separate the white noise $\mathbf{e}(t)$ into spatially uncontrollable components $\mathbf{e}_u(t)$ and controllable components $\mathbf{e}_c(t)$. Then (4.12) can be rewritten as

$$\mathbf{y}_r(t+d|t) = \hat{\mathbf{y}}_{r,c}(t+d|t) + F(q)\phi\mathbf{e}_c(t+d) + \underbrace{F(q)\phi\mathbf{e}_u(t+d) + \hat{\mathbf{y}}_{r,u}(t+d|t)}_{\mathbf{y}_{r,u}(t+d|t)}, \tag{4.15}$$

where $F(q)\phi\mathbf{e}_u(t+d|t)$ and $\hat{\mathbf{y}}_{r,u}(t+d|t)$ are combined as $\mathbf{y}_{r,u}(t+d|t)$, the uncontrollable parts of $\mathbf{y}_r(t+d|t)$. Specifically, define the projection operators $\mathbb{P}_c$ and $\mathbb{P}_u$ which project the profile into spatially controllable and uncontrollable subspaces, respectively. For the column space framework, $\mathbb{P}_c$ and $\mathbb{P}_u$ are defined as

$$\mathbb{P}_c = (\mathbf{G}^T\mathbf{G})^{-1}\mathbf{G}^T, \;\; \mathbb{P}_u = I - (\mathbf{G}^T\mathbf{G})^{-1}\mathbf{G}^T. \tag{4.16}$$

Then we have

$$\mathbf{y}_{r,u}(t+d|t) = \mathbb{P}_u\mathbf{y}_r(t+d|t), \;\; \mathbf{y}_{ss,u} = \mathbb{P}_u\mathbf{y}_{ss}. \tag{4.17}$$

From (4.17) one can see that the spatially uncontrollable components of both steady-state and residual profile can be extracted by using the operator $\mathbb{P}_u$. In order to solve the problem with the performance index (4.13) being sensitive to spatially high-frequency disturbances, the following modified performance index is suggested,

$$\eta_2 = \frac{trace\left[\sum_{i=0}^{d-1}\mathbf{F}_i\Sigma_{e_c}\mathbf{F}_i^T\right]}{trace(\Sigma_{y_{c,mse}})}, \tag{4.18}$$

where $\Sigma_{e_c} = \mathbb{E}[\mathbf{e}_c\mathbf{e}_c^T]$ is the covariance matrix of the white noise within the spatially controllable subspace. The covariance matrix in the denominator is further expressed to be

$$\Sigma_{y_{c,mse}} = \Sigma_{y_{r,c}} + diag(\mathbf{y}_{ss,c}\mathbf{y}_{ss,c}^T), \tag{4.19}$$

where $\Sigma_{y_{r,c}}$ is the covariance matrix of spatially controllable residual profile. The performance index (4.18) compares the covariance of unpredictable disturbance within the controllable subspace with the mean square error of the overall spatially controllable output profile. This performance index is not sensitive to high-frequency spatial disturbances since the spatially uncontrollable components have been removed before calculating the performance index.

Remark 4.3.1. Note that the numerator of (4.18) includes only the residual part, which makes sense since if the implemented controller has the spatial MVC structure (4.6) and an integrator, then the components of the steady-state profile within the controllable subspace (the steady-state benchmark) will be zero. However, since most implemented controllers are not MVC, there will be components left in the spatially controllable subspace, which explains the steady-state terms in (4.19).

4.4 User-specified benchmark

It is well known that for control loops MVC gives aggressive control actions and lacks robustness to model uncertainties. Consequently, MVC is not widely used in the process industry. In practice, to guarantee robust stability and performance, the actually implemented controllers are much more sluggish than MVC. If the MVC is still used as the benchmark, then most industrial controllers will show a very low performance index even though the underlying control loop is indeed operating with satisfactory performance. In such cases, the observation of low performance index based on the MVC benchmark does not necessarily imply poor controller design. Therefore, it is important to develop practical benchmarks based on the specific controller that is implemented in the process. The user-specified benchmark is an outcome of this idea, where a filter is defined as the desired closed-loop behavior and a parameter in the filter can be tuned to change the aggressiveness and conservativeness of the benchmark. In this section, the user-specified benchmark will be adapted to the CD process to make our benchmark more realistic.

For the CD process, we note that the spatial part of the MVC, $\mathbf{G}^{\dagger}$ in (B.12), removes the components of disturbance profile within the subspace spanned by columns of $\mathbf{G}$. However, due to the spatially-distributed nature, the $\mathbf{G}$ matrix for most CD processes has a large condition number. The ill-conditioned property of $\mathbf{G}$ implies that some of the singular values are vanishing. Therefore, the corresponding singular vector directions are considered uncontrollable and avoided in the CD controller so as to ensure robust stability and acceptable actuator action. It is therefore more realistic to select those (pseudo) singular vector directions (or

spatial frequencies, in the perspective of Fourier matrix transform) with significant mode gains and without wrong signs as controllable directions [99], which typically corresponds to the low spatial frequency range (specified by spatial bandwidth in this work).

The selection of desired spatial benchmark is not fixed depending on the specific CD controller that is being used. For instance, if we are using CD MPC, we may choose a spatial frequency dependent sensitivity function as the benchmark, which can be obtained from the steady-state weighting matrices in the objective function when there are no active constraints. In this thesis, for simplicity, we choose the estimated (closed-loop) spatial bandwidth as the spatial benchmark, which can be approximated from the width of the spatial response [100].

For the spatial bandwidth, the mathematical operators separating the spatially controllable and uncontrollable components $\mathbb{P}_{c,user}$ and $\mathbb{P}_{u,user}$ are constructed as

$$\mathbb{P}_{c,user} = \mathbf{P}_c^T \mathbf{P}_c, \;\; \mathbb{P}_{u,user} = \mathbf{I} - \mathbf{P}_c^T \mathbf{P}_c, \tag{4.20}$$

where [3] $\mathbf{P}_c = [\mathbf{P}(1:r,:)\ 0\ \mathbf{P}(m-r+2:m,:)]$, $\mathbf{P}$ is the m-dimensional Fourier matrix and in Matlab it can be defined as $\mathbf{P} = fft(eye(m))/sqrt(m)$. r is the selected spatial bandwidth. Notice that the selection of $\mathbf{P}$ can affect the performance index but this effect will be so small that the decision (e.g., as to the presence or absence of MPM) based on the performance index will not be influenced. Choosing $\mathbf{P}$ as the Fourier matrix is for the sake of being consistent with the definition of spatial bandwidth which is used in the tuning of CD controllers and expressed in the frequency domain. Moreover, it is more intuitive for users to specify the desired spatial bandwidth by choosing the Fourier matrix. According to the rule-of-thumb proposed in [101], r can be determined directly with the knowledge of spatial response width. The spatially controllable components, for both residual and steady-state profiles, are

$$\mathbf{y}_{ss,user} = \mathbb{P}_{c,user}\mathbf{y}_{ss}, \;\; \mathbf{y}_{r,user}(t) = \mathbb{P}_{c,user}\mathbf{y}_r(t). \tag{4.21}$$

In the temporal direction, when the implemented controller is not MVC, the controllable (either from

[3] Note that the colon follows Matlab's notation. $\mathbf{P}(1:r,:)$ represents the first r rows of $\mathbf{P}$, and $\mathbf{P}(m-r+2:m,:)$ represents the last $r-1$ rows of $\mathbf{P}$.

(4.16) or (4.20)) residual profile $\mathbf{y}_{r,c}(t)$ can be expressed as the impulse response form,

$$\begin{aligned}\mathbf{y}_{r,c}(t) &= f_0\mathbf{e}_c(t)+f_1\mathbf{e}_c(t-1)+\ldots+f_{d-1}\mathbf{e}_c(t-d+1)+\\ &\quad f_d\mathbf{e}_c(t-d)+f_{d+1}\mathbf{e}_c(t-d-1)+\ldots.\end{aligned} \tag{4.22}$$

For the temporal MVC, there will be no terms remaining after the first d terms in the time series model (4.22). The temporal user-specified term (scalar) $G_R(q)$ can be used to define a desirable form for the remaining terms such that,

$$\mathbf{y}_{r,c}(t) = f_0\mathbf{e}_c(t)+\ldots+f_{d-1}\mathbf{e}_c(t-d+1)+G_R(q)\mathbf{e}_c(t-d). \tag{4.23}$$

The user-specified term $G_R(q)$ can be selected as [18],

$$G_R(q) = [1-G_F(q)]R(q), \tag{4.24}$$

where $G_F(q)$ is the desired complementary sensitivity function with the first order form,

$$G_F(q) = \frac{1-\alpha_R}{1-\alpha_R q}, \tag{4.25}$$

and α_R is calculated via the desired closed-loop time constant τ_{des},

$$\alpha_R = e^{-\frac{T_s}{\tau_{des}}}, \tag{4.26}$$

where T_s is the sampling time. $R(q)$ is from the dynamic part of the disturbance model (4.5) via the Diophantine decomposition (B.7), $R(q) = H(q)/A(q)$.

By combining the spatial operators (4.21) and temporal term (4.24), the user-specified counterpart of η_2 can be obtained as follows,

$$\eta_{2,user} = \frac{trace\left[\sum_{i=0}^{d-1}\mathbf{F}_i\Sigma_{e_{user}}\mathbf{F}_i^T+\Sigma_{user}\right]}{trace(\Sigma_{y_{user,mse}})}, \tag{4.27}$$

where $\Sigma_{e_{user}} = \mathbb{E}[\mathbf{e}_{user}(t)\mathbf{e}_{user}^T(t)]$, $\mathbf{e}_{user}(t) = \mathbb{P}_{c,user}\mathbf{e}(t)$, $\Sigma_{user} = Var[G_R(q)\mathbf{e}_{user}(t)]$. The denominator of $\eta_{2,user}$

is,

$$\Sigma_{y_{user,mse}} = \Sigma_{y_{r,user}} + diag(\mathbf{y}_{ss,user}\mathbf{y}_{ss,user}^T), \tag{4.28}$$

where $\Sigma_{y_{r,user}} = \mathbb{E}[\mathbf{y}_{r,user}(t)\mathbf{y}_{r,user}^T(t)]$. It can be seen that compared with η_2, in the spatial direction, the only difference in $\eta_{2,user}$ is that the controllable projector is replaced by a user-specified projector $\mathbb{P}_{c,user}$, which is applied to both steady-state and residual profiles. In the temporal direction, an additional term $G_R(q)$ which represents the desired sensitivity function is included to the residual benchmark. Note that this term is not applicable to the steady-state profile.

Remark 4.4.1. Note that (4.24) implies that in order to obtain a user-specified benchmark, the disturbance model has to be available, which is not realistic as the disturbance model may change from time to time. However, for simplicity, we assume the disturbance model to be known. This assumption is valid since there have been extensive methods proposed on the identification of disturbance models using closed-loop input-output data [51, 102].

Remark 4.4.2. If the user-specified term is selected to be the same as the nominal closed-loop response (when the tuning parameters of controller are available), then the highest achievable user-specified performance index will be 1. In this case, the value of user-specified performance index will make more sense and provide better indication of the control performance.

4.5 Performance monitoring

In order to compute previous performance indices, the residual profile has to be fitted into a moving average model (refer to (4.15) and (4.22)) to obtain the estimates of impulse response coefficient matrices and white noise covariance. However, due to the high input-output dimensions of CD processes, the computational burden plays an essential role in multivariate time series estimation. In this section, a novel technique is proposed to reduce the computations in performance monitoring.

4.5.1 Vector autoregressive modeling

As illustrated in previous sections, to proceed with performance monitoring, we need to perform the following multivariate time series identification,

$$\mathbf{y}_r(t) = \Theta_1\mathbf{y}_r(t-1) + \ldots + \Theta_p\mathbf{y}_r(t-p) + \mathbf{e}(t), \tag{4.29}$$

where $\mathbf{e}(t) \in \mathbb{R}^m$ is the white noise vector. The $\Theta_i \in \mathbb{R}^{m\times m},\ i = 1,2,\ldots,p$, are the coefficient matrices to be estimated for the vector autoregressive (VAR) process, where p is the temporal order selected by the user. If $\Theta_i,\ i = 1,2,\ldots,p$, are chosen to be full matrices, estimating the VAR model (4.29) will be computationally expensive. However, we can assume that $\Theta_i,\ i = 1,2,\ldots,p$, are Toeplitz-structured, because in industry most CD controllers have limited spatial response width, which means that the CD multivariate controller will be band-diagonal [11, 103, 104]. Furthermore, the plant $\mathbf{G}$ in general is Toeplitz-structured, and as a result the closed-loop sensitivity function will be approximately band-diagonal [105]. By taking advantage of the special structure of Θ_i, the estimation problem can be greatly simplified through basis matrices method described below.

We construct basis matrices to decompose each Toeplitz-structured coefficient as the sum of a series of scalars multiplied by simple basis matrices. Each Toeplitz-structured VAR coefficient Θ_i matrix has the form,

$$\Theta_i = \text{toeplitz}\{\theta_{i,1},\ldots,\theta_{i,q},\ldots\}_{m\times m}, \tag{4.30}$$

where q is the spatial order selected by the user. There are only q unknown scalars to be estimated in each coefficient matrix. The unknown scalars $\theta_{i,j}, j = 1,\ldots,q$, are extracted from Θ_i by rewriting the large dimensional matrix as the sum of simple terms,

$$\Theta_i = \sum_{j=1}^{q} \theta_{i,j}\mathbf{E}_j, \tag{4.31}$$

where $\mathbf{E}_j, j = 1,\ldots,q$ are basis matrices with the j^{th} superdiagonal and $-j^{th}$ subdiagonal entries as 1, while the other entries are all 0. Thus the i-th term of the VAR model (4.29) can be written as,

$$\Theta_i\mathbf{y}_r(t-i) = \sum_{j=1}^{q} \theta_{i,j}\mathbf{E}_j\mathbf{y}_r(t-i) = \sum_{j=1}^{q} \theta_{i,j}\tilde{\mathbf{y}}_{r,ij}(t-i),$$

where $\tilde{\mathbf{y}}_{r,ij}(t-i) = \mathbf{E}_j y_r(t-i)$. The overall VAR model becomes

$$\begin{aligned}
\mathbf{y}_r(t) &= \theta_{11}\tilde{\mathbf{y}}_{r,11}(t-1)+\ldots+\theta_{1q}\tilde{\mathbf{y}}_{r,1q}(t-1)+\theta_{21}\tilde{\mathbf{y}}_{r,21}(t-2)+\ldots+\theta_{2q}\tilde{\mathbf{y}}_{r,2q}(t-2)+ \\
&\quad \ldots+\theta_{p1}\tilde{\mathbf{y}}_{r,p1}(t-p)+\ldots+\theta_{pq}\tilde{\mathbf{y}}_{r,pq}(t-p)+\mathbf{e}(t) \\
&\stackrel{\triangle}{=} \tilde{\mathbf{Y}}_r(t-1)\theta+\mathbf{e}(t),
\end{aligned} \tag{4.32}$$

where

$$\tilde{\mathbf{Y}}_r(t-1) = \begin{bmatrix} \tilde{\mathbf{y}}_{r,11}(t-1) & \tilde{\mathbf{y}}_{r,12}(t-1) & \dots & \tilde{\mathbf{y}}_{r,pq}(t-p) \end{bmatrix},$$

$$\theta = \begin{bmatrix} \theta_{11} & \theta_{12} & \dots & \theta_{pq} \end{bmatrix}^T.$$

The following steps for identification are similar to the scalar autoregressive model identification. There are various well-developed techniques for this problem, e.g., the least-squares method. The residuals $\hat{\mathbf{e}}(t)$ resulting from the identification are considered to be estimates of the innovations $\mathbf{e}(t)$. The estimate of coefficients θ is denoted as $\hat{\theta}$. Then the Toeplitz coefficients $\hat{\Theta}_i, i = 1,\dots,p$, can be determined by reconstructing $\hat{\theta}$. By using the basis matrices, the estimation of the VAR model (4.29) can be significantly simplified.

In order to calculate the performance indices, the VAR model above is transformed into the following vector moving average (VMA) model by using the technique in [106],

$$\mathbf{y}_r(t) = \hat{\Phi}_0\hat{\mathbf{e}}(t) + \dots + \hat{\Phi}_{d-1}\hat{\mathbf{e}}(t-d+1) + \hat{\Phi}_d\hat{\mathbf{e}}(t-d) + \dots, \tag{4.33}$$

where

$$\hat{\Phi}_0 = I, \tag{4.34}$$

$$\hat{\Phi}_i = \sum_{j=1}^{i} \hat{\Phi}_{i-j}\hat{\Theta}_j, \;\; i = 1,\dots,d,\dots. \tag{4.35}$$

Although the order of the VMA model (4.33) will be infinite, we are only interested in the first d terms since they are the coefficients required in evaluating the benchmark. When applying this algorithm, d can be selected to be the time delay in the model as an approximation of the true time delay in the process. On the other hand, due to the spatial performance limitation resulting from the structure of G, only the controllable components of estimated residuals $\hat{e}_c(t)$ and the output profile $y_{r,c}(t)$ are considered. The covariance matrix of the output under temporal MVC within the column space of G matrix is thus expressed as,

$$\hat{\Sigma}_{mv} = \sum_{i=0}^{d-1} \hat{\Phi}_i \Sigma_{\hat{e}_c} \hat{\Phi}_i^T, \tag{4.36}$$

where $\Sigma_{\hat{e}_c} = \mathbb{E}[\hat{e}_c(t)\hat{e}_c^T(t)]$ is the covariance of spatially controllable residual, $\hat{e}_c(t)$. The overall estimated

performance index $\hat{\eta}_2$ is obtained as,

$$\hat{\eta}_2 = \frac{trace(\hat{\Sigma}_{mv})}{trace(\Sigma_{y_{c,mse}})}, \tag{4.37}$$

where $\hat{\eta}_2$ is the estimate of performance index η_2.

4.5.2 Performance monitoring algorithm

As illustrated in previous sections, any given CD data set (without MD variations) can be separated into a sum of steady-state and residual profiles. The steady-state profile is obtained by averaging the data for each CD bin over all scans. In order to calculate performance indices (4.13), (4.18) or (4.27), the steady-state profile $\mathbf{y}_{ss}$ has to be separated into controllable parts $\mathbf{y}_{ss,c}$ and uncontrollable parts $\mathbf{y}_{ss,u}$ according to the column space of $\mathbf{G}$ or the spatial bandwidth. A VAR model (4.29) is applied to the residual profile $\mathbf{y}_r(t)$ to obtain the controller-invariant variation due to time-delay and spatial bandwidth limitations. The uncontrollable parts of the steady-state variation, $\mathbf{y}_{ss,u}$, and the controller-invariant variations of the residuals, $\mathbf{y}_{r,u}$, are combined to obtain the overall benchmark in (4.13). The algorithm we propose to calculate (4.18) is as follows:

1. For a given data set, $\mathbf{Y}$, remove the MD variations (i.e., mean value of each scan).

2. Calculate the average CD profile by averaging the data set across all scans, record it as $\mathbf{y}_{ss}$. Remove the mean of each CD bin to obtain the residual profile $\mathbf{y}_r(t)$.

3. Perform Toeplitz-structure VAR estimation (4.29) using the residual profile $\mathbf{y}_r(t)$ with the selected spatial order q and temporal order p. Check the whiteness of noise estimate $\hat{\mathbf{e}}(t)$. If the residual is not white, one can increase the orders of VAR model to allow more flexible model structures.

4. Transform the VAR model into a VMA model (4.33) and obtain the coefficient matrices $\hat{\Phi}_i, i = 0,\ldots,d-1$.

5. Construct the operator $\mathbb{P}_c$ based on the column space (4.16), and get the following controllable components: $\hat{\mathbf{e}}_c = \mathbb{P}_c\hat{\mathbf{e}}(t)$, $\mathbf{y}_{r,c} = \mathbb{P}_c\mathbf{y}_r$, $\mathbf{y}_{ss,c} = \mathbb{P}_c\mathbf{y}_{ss,c}$.

6. Calculate the estimated minimum covariance $\hat{\Sigma}_{mv}$ in (4.36), $\Sigma_{y_{c,mse}}$ in (4.37) and PI in (4.37).

For the user-specified benchmark $\eta_{2,user}$, in Step 5, the operator $\mathbb{P}_c$ can be constructed based on the selected spatial bandwidth (4.20). Besides, the temporal user-specified term can be obtained from the knowledge of desired closed-loop time constant together with (4.24) and (4.26).

Remark 4.5.1. In order to obtain the performance index, one has to fit the CD profile to the VAR model (4.29), which requires each output channel to be zero-mean. Otherwise, there will be an offset term showing up in (4.29), as illustrated in [106]. This fact motivates the profile partition in Section 4.2 and 4.3. After splitting the output measurements into steady-state profile and residual profile, we can simply fit only the residual profile into (4.29).

4.6 Examples

It has been mentioned that various factors such as a poorly tuned controller, model-plant mismatch, change of disturbance dynamics, etc., can cause a drop in the performance index. From the perspective of industry engineers, when the model quality deteriorates, a new model has to be identified. Therefore, it is of interest to determine whether the proposed performance benchmarks are sensitive to model-plant mismatches. In this section, the validity of the proposed performance benchmark for the CD process is tested using data sets from both paper machine simulators and paper mills.

4.6.1 Simulation results

In this subsection, scenarios with various types of model-plant mismatch are created to test the sensitivity of performance index. In this simulation, the employed control strategy is the two-dimensional loopshaping technique. The number of actuators in the CD array is 238, and the number of CD bins downstream at the scanner side is 714.

The continuous steady-state spatial response shape of a single actuator is determined by four parameters, gain γ, width ξ, divergence β and attenuation α in (1.2) (see [12] for more details). In the temporal direction, the actuator dynamic model $g(s)$ is assumed to be FOPTD with unit steady-state gain,

$$g(s) = \frac{1}{\tau s + 1} e^{-\tau_d s}, \tag{4.38}$$

where τ the time constant τ and τ_d is the time delay. In the simulator, the nominal values of these parameters on both plant and process model are set initially as $\gamma_0 = -0.03, \xi_0 = 164mm, \beta_0 = 0.15, \alpha_0 = 7.0, \tau_0 = 17.34s, \tau_{d0} = 21s$. Figure 4.2 illustrates the spatial steady-state impulse response and the temporal step response of one actuator with these nominal parameter values. This process is relatively easy to control

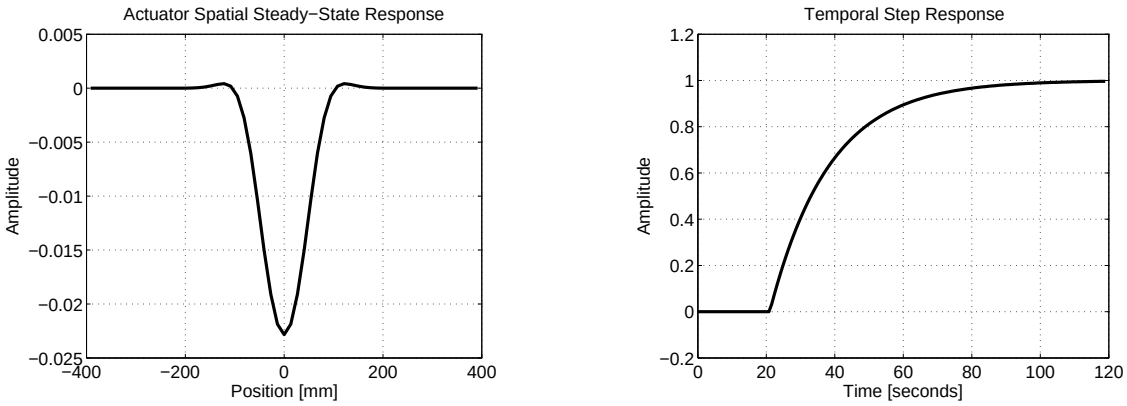

Figure 4.2: Spatial impulse steady-state response and the temporal step response of a single actuator. The negative peak of the spatial response is due to the negative gain of the actuator spatial model.

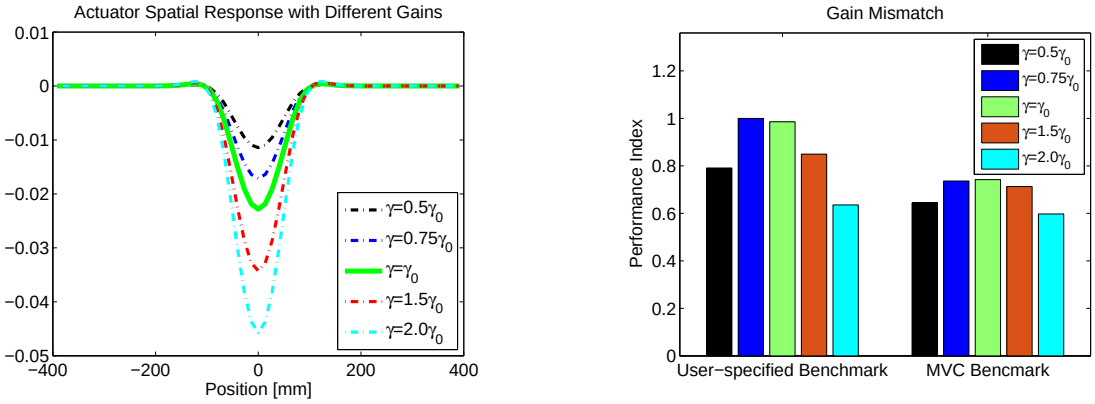

Figure 4.3: Performance indices for different levels of gain mismatch. Note that γ_0 is the nominal gain value used by the controller, γ is the actual gain value of the process plant.

since there are no negative side lobes in the spatial response shape. The controllers are properly tuned by using the two-dimensional loop shaping technique based on the nominal process model.

In order to investigate the sensitivity of proposed performance index in detecting the model-plant parametric mismatch, scenarios with different levels of mismatch for these spatial and temporal parameters are created. For convenience, we manually increase and decrease the parameter values in the plant while the parameter values in the process model used by the controller remain unchanged. In the following simulations, we denote $\gamma, \xi, \beta, \alpha, \tau, \tau_d$ without subscripts as the plant parameters. In addition, positive mismatches indicate that the plant parameters are greater than those in the model. For instance, positive gain mismatch means the plant gain is greater than the model gain used by the controller.

Figures 4.3-4.6 illustrate the simulation results with respect to various levels of parametric mismatch for each parameter in the spatial model. Note that in this simulation, the sampling time is 20 seconds and the

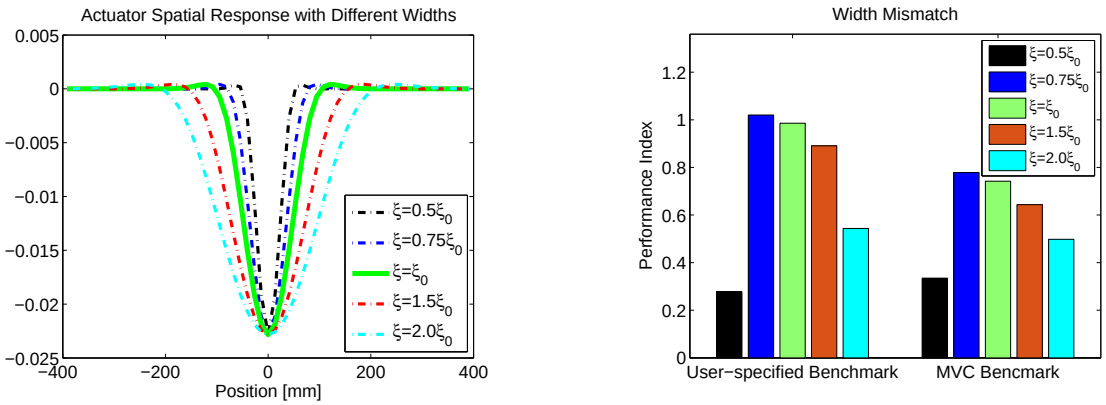

Figure 4.4: Performance indices for different levels of width mismatch. Note that ξ_0 is the nominal width value used by the controller, ξ is the actual width value of the process plant.

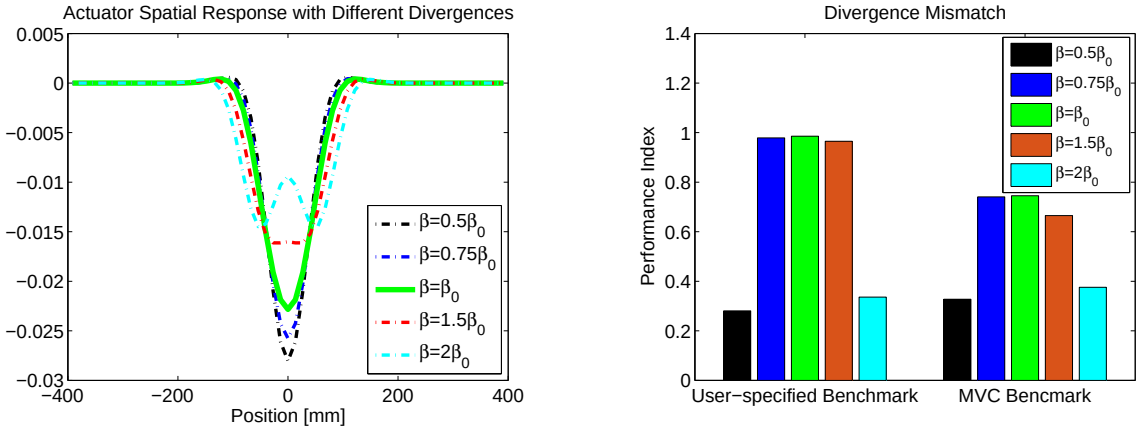

Figure 4.5: Performance indices for different levels of divergence mismatch. Note that β_0 is the nominal divergence value used by the controller, β is the actual divergence value of the process plant.

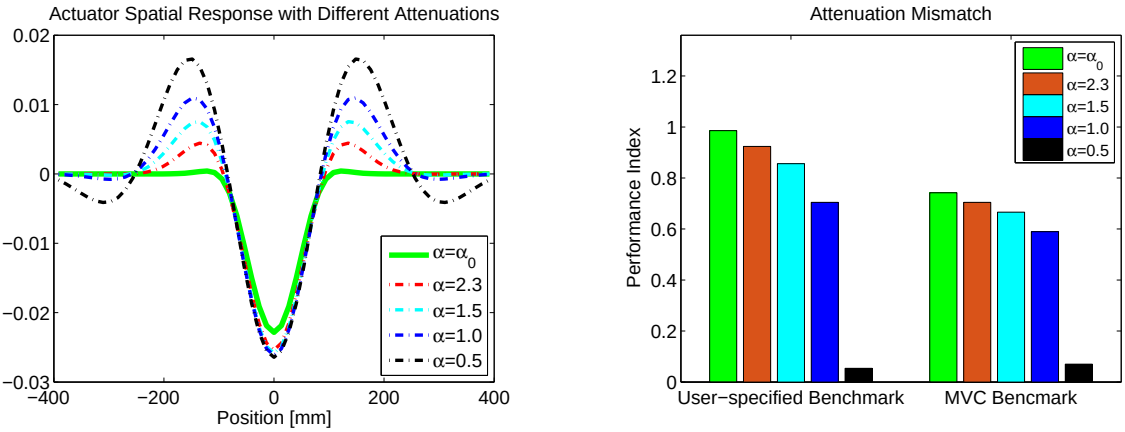

Figure 4.6: Performance indices for different levels of attenuation mismatch. Note that α_0 is the nominal attenuation value used by the controller, α is the actual attenuation value of the process plant.

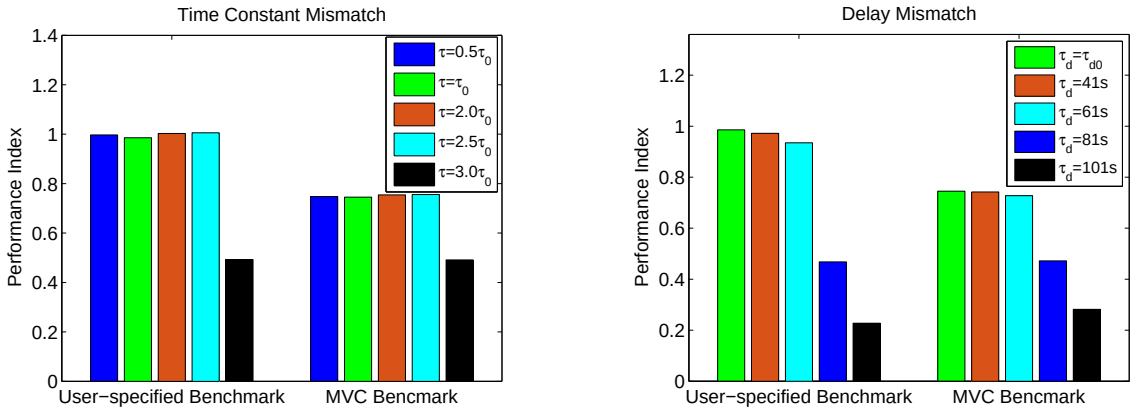

Figure 4.7: Performance indices for different levels of time constant and time delay mismatch. Note that τ_0 and τ_{d0} are the nominal time constant and time delay value used by the controller, τ and τ_d are the actual time constant and time delay value of the process plant.

data is selected after the initial transient behavior. The number of scans in the selected portion of data is 500. The left graph in each figure shows the comparison of spatial response shape of each mismatched plant with that of the nominal case, from which we can know the significance of distortion the corresponding parametric mismatch can cause. The right graph of each figure shows the corresponding calculated performance index for each case based on both MVC benchmark η_2 and user-specified benchmark $\eta_{2,user}$. One can see that in general the user-specified performance indices are higher than that based on the MVC benchmark, which agrees well with the previous analysis as the user-specified benchmark is more practical and less aggressive. These figures show that for most MPM, the performance indices based on both MVC benchmark and user-specified benchmark decrease as the degree of MPM increases. However, the performance indices with gain and width mismatches with $\gamma = 0.75\gamma_0$ and $\xi = 0.75\xi_0$ show better performance than the case without MPM. It can be explained that the degree of mismatch is not severe and within the tolerance of implemented robust controller and these mismatched processes are more close to the models used by the controller. However, for the cases with large mismatches, all performance indices drop. Besides, the performance index is sensitive to the divergence mismatch but not so sensitive to the attenuation mismatch. Figure 4.7 shows the performance indices for the time constant and time delay mismatches. One can see that the performance indices are able to detect the drop in performance due to the time constant or delay mismatch as well, but not so sensitive as the spatial parameters. Note that for some cases (e.g. width mismatch with $\xi = 0.75\xi_0$), the indices show a slightly better performance compared with the nominal case. Table I shows the partitioned variances for each simulated case, in which σ_T, σ_{CD}, σ_{Res} refer to the total variance, CD variance (variance of the steady-state

Table 4.1: Variance partition for each simulated case

γ MPM	σ_T	σ_{CD}	σ_{Res}	ξ MPM	σ_T	σ_{CD}	σ_{Res}
$\gamma = 0.50\gamma_0$	0.2575	0.0687	0.1888	$\xi = 0.50\xi_0$	0.3715	0.1812	0.1903
$\gamma = 0.75\gamma_0$	0.2454	0.0523	0.1930	$\xi = 0.75\xi_0$	0.2391	0.0453	0.1937
$\gamma = 1.50\gamma_0$	0.2511	0.0453	0.2059	$\xi = 1.50\xi_0$	0.2621	0.0643	0.1979
$\gamma = 2.00\gamma_0$	0.2739	0.0485	0.2253	$\xi = 2.00\xi_0$	0.2979	0.1017	0.1961
β MPM	σ_T	σ_{CD}	σ_{Res}	α MPM	σ_T	σ_{CD}	σ_{Res}
$\beta = 0.50\beta_0$	0.3804	0.1861	0.1943	$\alpha = 2.3$	0.2496	0.0505	0.1991
$\beta = 0.75\beta_0$	0.2434	0.0459	0.1975	$\alpha = 1.5$	0.2595	0.0543	0.2052
$\beta = 1.50\beta_0$	0.2571	0.0459	0.1975	$\alpha = 1.0$	0.2756	0.0594	0.2162
$\beta = 2.00\beta_0$	0.3497	0.1579	0.1918	$\alpha = 0.5$	1.8128	0.2307	1.5758
τ MPM	σ_T	σ_{CD}	σ_{Res}	τ_d MPM	σ_T	σ_{CD}	σ_{Res}
$\tau = 0.5\tau_0$	0.2428	0.0480	0.1948	$\tau_d = 41$	0.2448	0.0473	0.1976
$\tau = 2.0\tau_0$	0.2406	0.0472	0.1933	$\tau_d = 61$	0.2480	0.0491	0.1989
$\tau = 2.5\tau_0$	0.2447	0.0480	0.1967	$\tau_d = 81$	0.3093	0.1060	0.2033
$\tau = 3.0\tau_0$	0.3007	0.1059	0.1948	$\tau_d = 101$	0.4271	0.2224	0.2047

Note: For the normal case, $\sigma_T = 0.2439$, $\sigma_{CD} = 0.0476$, $\sigma_{Res} = 0.1962$.

profile) and residual variance. Note that there is no MD variance since the MD profile has been removed beforehand. By comparing these results with the previous performance indices one can see, mostly, the larger variance in either CD or residual than the nominal case will correspond to worse control performance. Therefore we can conclude that the proposed performance indices are not only affected by the CD variance, but also the residual variance.

To demonstrate the advantage of performance index η_2 over η_1, another simulation is carried out with gain mismatch $\gamma = 2.0\gamma_0$ and a spatial sinusoidal disturbance (with frequency greater than the closed-loop spatial bandwidth) added to the output. Sinusoidal disturbance is commonly encountered in practice when there are malfunctions in process devices. The performance index is expected to drop relative to the normal case due to the presence of gain mismatch, however, it is desirable for the high frequency spatial disturbance to affect the index as little as possible. Simulation results under this situation are illustrated in Figure 4.8. The performance index η_1 with both positive gain mismatch and high frequency spatial disturbance remains almost the same as the normal case, while it drops a little for the case with gain mismatch only. Thus it is not straightforward to observe the performance deterioration in the presence of high frequency spatial disturbance if we are using performance index η_1. However, for performance index η_2, the presence of high frequency spatial disturbance has almost no affect, and the drop in the performance index is due to the gain mismatch. Moreover, one may find from Figure 4.8 that the performance index η_1 is not so sensitive to the mismatch as the index η_2 since the drop due to gain mismatch is much smaller compared with η_2. Therefore,

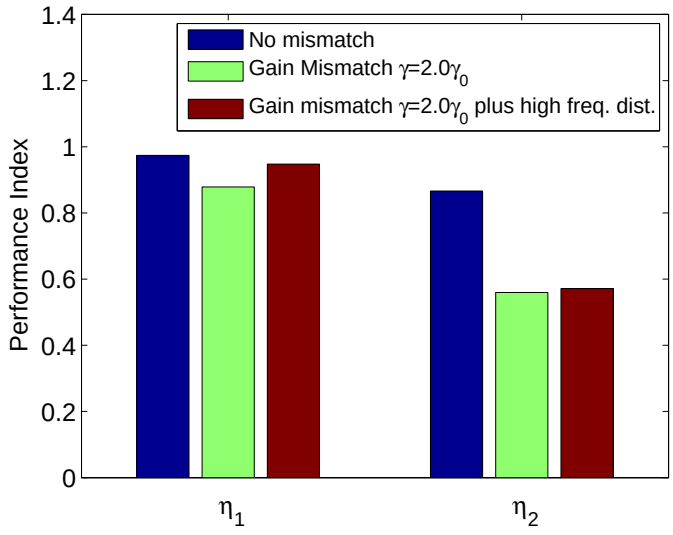

Figure 4.8: Comparison of performance index η_1 and η_2 with high frequency spatial disturbance

we can achieve reliable assessment based on performance index η_2. As mentioned in the previous section, the misleading conclusion from η_1 is a result of the deterministic high frequency disturbance inflating both the covariance of the benchmark and the actual output in (4.13). The ratio between the two covariance matrices will be very close to one.

4.6.2 Industrial example

In this subsection, data sets from a paper mill are used to validate the effectiveness of the proposed techniques. The number of actuators and CD bins in this example are 114 and 402, respectively. The width of each actuator zone is 60 mm and the width of each CD bin is 16.79 mm. Figure 4.9a illustrates the measured dry weight profile without MD variations. Note that the edges of the profile that were not controlled have been removed. Figure 4.9b shows the corresponding actuator (ProFlow) profile with lower bound 10% and upper bound 90%. The sampling interval is 16 seconds with time-delay 45 seconds and the number of scans is 551. The implemented controller is a multivariate CD-MPC. In this data set, an unknown spatial disturbance is acting on the output profile and is attenuated by the controller through manipulating the actuators. Performance monitoring with a moving window of size 200 scans is applied to the measured output profile, and the corresponding performance indices over moving windows is demonstrated in Figure 4.10a. Both user-specified benchmark ($\eta_{2,user}$ in the blue solid line) and MVC benchmark (η_2 in the red dash-dotted line and η_1 in the black dashed line) are used in the calculation of these performance indices. The VMA model

proposed in Section 4.5 is estimated repeatedly for each window in order to the compute those performance indices. For each window, on average, it takes only 1.68 seconds to identify the VMA model, which is much less than the sampling interval and thus fast enough for online monitoring. Note that performance indices are calculated only after the 200th scan since the width of each window is 200 scans. It can be observed that all these performance indices show consistent patterns except their levels. The performance index η_2 shows the worst performance since it is based on the aggressive MVC benchmark. The high level of η_1 is due to that the spatially uncontrollable components in the denominator and numerator of (4.13) are the majority. The user-specified benchmark $\eta_{2,user}$ also shows higher performance index than η_2, which makes sense since $\eta_{2,user}$ is based on a more practical and less aggressive benchmark.

For this industrial example, the user-specified benchmark is specified based on the implemented controller. Thus good control performance is expected to have $\eta_{2,user}$ close to one. However, from Figure 4.10a we find that all these performance indices are less than 0.7, which is not satisfactory. In order to investigate the root causes, we generated the steady-state profile of both the dry weight and actuator as well as the power spectrum of averaged dry weight profile, which are shown in Figure 4.10b-d. From the spectrum plot, it is obvious that some low-frequency components are left in the controllable range which contributes to the poor performance. These low frequency components are due to the large fluctuations of the dry weight profile in the first 60 bins and those around the 280th bin. From the averaged actuator profile, we find that the actuator saturation in the first few zones and around the 85th zone explains the reason that those fluctuations in the output profile were not rejected. Therefore, the actuator saturation due to the spatial disturbance is one root cause of the low performance index. However, further diagnosis or data pre-processing techniques are required to know if the model-plant mismatch is also one of the root causes. For instance, in order to reduce the false positives on the model-plant mismatch diagnosis, we may select a portion of data in which there are no severe actuator saturation, irregular disturbances or poorly tuned control to apply the performance monitoring algorithm. Alternatively, approaches on deriving performance lower bounds for constrained control (such as the work by Wang and Boyd [107]) could potentially be used to improve the MVC and user-specified benchmarks. In this work, we combine the MVC and user-specified benchmarks with our MPM detection approach to address this issue.

Note that the computational complexity associated with the performance index is an important concern for online performance monitoring. For both simulator and industrial examples studied in this work, the computation speed is fast enough (less than 3 seconds for each window), compared with the sampling in-

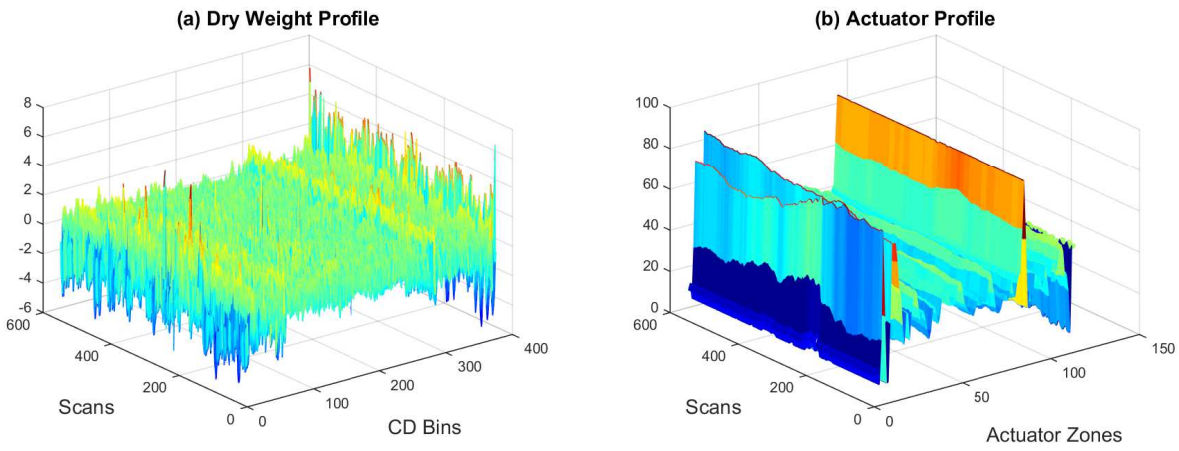

Figure 4.9: Three-dimensional plot of input-output profiles from industrial data set. (a): The dry weight profile (g/m^2) with 376 measurement bins with MD trend removed; (b): The actuator profile (%) of 114 actuator zones.

terval (more than 15 seconds for most paper machines). Thus the proposed algorithms for computing the performance indices are efficient enough for online performance monitoring.

4.7 Summary

In this chapter, a spatial and temporal MVC benchmark for both steady-state and residual profiles are analyzed for the CD process of paper machines. Performance indices are proposed based on the steady-state and residual MVC benchmark. The sensitivity of these performance indices with respect to large spatial high-frequency disturbances are analyzed and compared. Furthermore, the corresponding user-specified benchmark is put forward by taking into account the desirable closed-loop dynamics in both temporal and spatial directions. A novel technique is employed to improve the efficiency of computations associated with the multivariate time series model identification. The proposed technique decomposes the coefficient matrices into a series of simple multiplications between scalars and basis matrices. These basis matrices are constructed based on the special structure of coefficient matrices. Data sets from a CD simulator are used to test the sensitivity of proposed performance indices with respect to various types of mismatch existing in the CD process as well as to spatial high-frequency disturbances. Finally, an industrial data set is introduced to test the effectiveness of proposed performance monitoring technique. It is observed that in this data set, the actuator saturation due to the large amplitude of spatial disturbances is a cause for the low control performance.

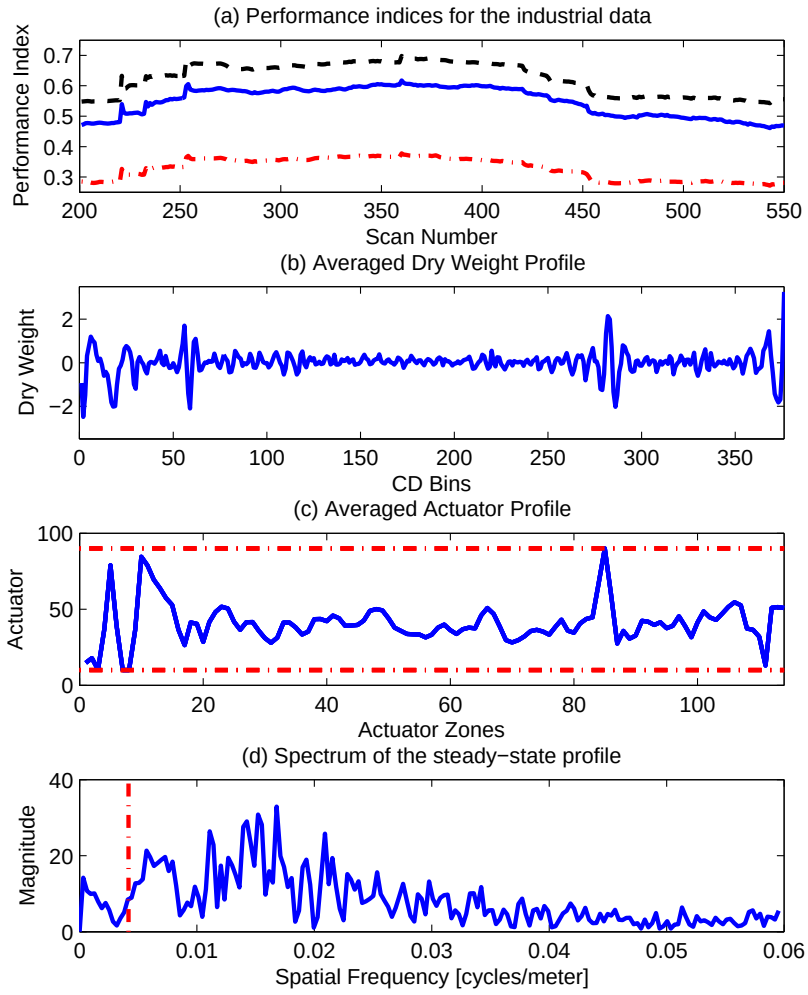

Figure 4.10: The analysis of the industrial data. (a): The moving window performance indices for the measured data. Blue solid line: $\eta_{2,user}$; Red dash-dotted line: η_2; Black dashed line: η_1; (b): The steady-state of the entire dry weight profile; (c): The steady-state of the entire actuator profile with lower bound and upper bound (red dash-dotted line); (d): The spectrum of the averaged dry weight profile and the approximated spatial bandwidth (red dash-dotted line).

Chapter 5

Model-plant Mismatch Detection for CD Processes

5.1 Introduction

In this chapter, we focus on extending the MD MPM detection method to CD processes. As shown in Chapter 3, routine closed-loop identification forms one of the main building blocks for the proposed MPM detection algorithm. Due to the large number of actuators and measurement sensors, closed-loop identifications of CD processes have not been extensively explored. However, two assumptions widely employed by the industry, separability between spatial and temporal responses and identical models for all CD actuators, can greatly facilitate the CD identifications. Under the first assumption, a CD process model is essentially a high-dimensional (linear version of) Hammerstein model with a static (spatial) part in connection with a dynamic part [108]. Various identification toolboxes developed for Hammerstein models would be inspiring for the CD process identification. With the second assumption, the spatial static model is further simplified as a sparse Toeplitz-structured matrix. Based on these two observations, we will present a closed-loop identification method for CD processes, by extending our previous ARX-OE method to high-dimensional models. In addition, we will show a CD MPM detection framework that is based on routine operating data and can discriminate the MPM (we use MPM exclusively to refer to the mismatches in spatial and temporal models) from changes in unmeasured disturbance models. The MPM idea is similar to that for MD processes, differing in that for CD processes we have more models to monitor.

This chapter is organized as follows. A preliminary description of the closed-loop CD process is given in Section 5.2. Section 5.3 is devoted to the development of routine CD closed-loop identification method, which includes convergence and consistency analysis of the proposed algorithm. We demonstrate the procedures of implementing one-class SVM to MPM detection in Section 5.4. Two illustrative examples are

provided in Section 5.5 to show the effectiveness of the proposed CD closed-loop identification approach, as well as the advantage of our MPM detection scheme. This chapter ends with a conclusion in Section 5.6.

5.2 Preliminaries

5.2.1 CD process model

We focus on the following single-array CD process that is widely employed in paper machine control,

$$\mathscr{S}_1 : \mathbf{y}(t) = g^o(q)\mathbf{G}^o\mathbf{u}(t-d) + \mathbf{v}(t), \tag{5.1}$$

where $\mathbf{y}(t) \in \mathbb{R}^m$ and $\mathbf{u}(t) \in \mathbb{R}^n$ represent the CV and MV profiles, respectively. $\mathbf{v}(t) \in \mathbb{R}^m$ is a colored measurement noise vector. $g^o(q)$ is a FOPTD filter with unit gain, i.e.,

$$g^o(q) = \frac{1-f^o}{1-f^o q}, \tag{5.2}$$

where $f^o = exp(-T_s/T_p)$ with T_p and T_s being the time constant and sampling interval, respectively. $\mathbf{G}^o \in \mathbb{R}^{m\times n}$ is a steady-state gain matrix which represents the spatial responses of actuator array at steady state. d is the discrete time-delay. Note that in (5.1) we use a superscript "o" to denote the true process. The spatial model $\mathbf{G}^o$ is assumed to be Toeplitz-structured. As a result, $\mathbf{G}^o$ is decomposed as follows,

$$\mathbf{G}^o = \sum_{k=1}^{p^o} c_k^o \mathbf{E}_k, \tag{5.3}$$

where c_k^o is a scalar standing for the k-th elements in $\mathbf{G}^o$ and $\mathbf{E}_k$ is the corresponding k-th basis matrix. Taking $m = 6, n = 3, p^o = 2$ as an example, we have

$$\mathbf{G}^o = \begin{bmatrix} c_1^o & c_3^o & 0 \\ c_2^o & c_2^o & 0 \\ c_3^o & c_1^o & c_3^o \\ 0 & c_2^o & c_2^o \\ 0 & c_3^o & c_1^o \\ 0 & 0 & c_2^o \end{bmatrix}, \mathbf{E}_1 = \begin{bmatrix} 1 & 0 & 0 \\ 0 & 0 & 0 \\ 0 & 1 & 0 \\ 0 & 0 & 0 \\ 0 & 0 & 1 \\ 0 & 0 & 0 \end{bmatrix}, \mathbf{E}_2 = \begin{bmatrix} 0 & 0 & 0 \\ 1 & 1 & 0 \\ 0 & 0 & 0 \\ 0 & 1 & 1 \\ 0 & 0 & 0 \\ 0 & 0 & 1 \end{bmatrix}, \mathbf{E}_3 = \begin{bmatrix} 0 & 1 & 0 \\ 0 & 0 & 0 \\ 1 & 0 & 1 \\ 0 & 0 & 0 \\ 0 & 1 & 0 \\ 0 & 0 & 0 \end{bmatrix}.$$

With above decomposition we can identify the spatial model $\mathbf{G}^o$ by estimating the parameters $\mathbf{c}^o = [c_1^o \ \dots \ c_{q^o}^o]^T$ instead of those in the nonlinear function (1.2). Note that the separability between temporal dynamic model

$g^o(q)$ and spatial static model $\mathbf{G}^o$ connects the typical CD process with Hammerstein models [109], which inspires the closed-loop identification method proposed in this chapter.

5.2.2 CD noise model

Most literature on CD system identification only considers the situations with $\mathbf{v}(t)$ being Gaussian white noise [83]. However, in practice, the physical nature of measurement devices (e.g. traveling back and forth in the cross direction) makes $\mathbf{v}(t)$ a colored noise in both spatial and temporal directions. Researchers have made a few attempts to model the CD measurement noise in certain ways so as to reflect the correlations in these two directions [81, 110, 111]. Several noise models, varying from simple to complex, have been available in the literature to precisely represent the realistic noise encountered in the industry. A common practice is to use a multivariate band-diagonal AR or ARMA structure so that the temporal correlation is modeled through each filter on the diagonal and the spatial correlation is represented by interactions among off-diagonal entries [111]. An alternative is to choose the noise model as diagonal while enforcing the innovation sequence to have non-diagonal covariance matrix [81]. For the latter method, the spatial correlation of colored noise $\mathbf{v}(t)$ is reflected by the covariance matrix. From the viewpoint of system identification proposed in this chapter, the latter method is favored since it admits inversing the noise model matrix without concerning the issue of invertability of the noise matrix that often arises in the former method. Moreover, analogous to the temporal dynamic model, we assume that all output channels possess the same noise model in the temporal direction[4]. In this manner,

$$\mathbf{v}(t) = H^o(q)\mathbf{I}\mathbf{e}^o(t), \tag{5.4}$$

where $H^o(q)$ is a scalar monic transfer function that is stable and inversely stable, $\mathbf{I} \in \mathbb{R}^{m\times m}$ is an identity matrix, and $\mathbf{e}^o(t) \in \mathbb{R}^m$ is a zero-mean Gaussian white noise vector with covariance

$$\mathbb{E}[\mathbf{e}^o(t)\mathbf{e}^o(t-s)^T] = \delta_{s,t}\Sigma \in \mathbb{R}^{m\times m}. \tag{5.5}$$

Note that here Σ can be non-diagonal and structured to represent the spatial correlations of CD measurement noise. In general, it is difficult to acquire prior information about the true noise model structure $H^o(q)$ in

[4]This assumption can be easily relaxed to allow for different noise models in each output channel and the identification method presented here is still applicable with slight modifications.

(5.4). For closed-loop identification especially the direct identification approach, incorrect specification of the noise model often leads to bias in the process model estimate [15]. In this chapter, we propose a novel closed-loop identification method for the CD process model to address this issue.

5.2.3 High-order ARX approximation of the CD process model

It is well-known that any stable linear transfer function can be approximated arbitrarily well by a high-order FIR model [15, 112]. Inspired by this fact we can represent the CD process model (5.1)-(5.4) with a sufficiently high-order ARX structure, in order to avoid the bias issue in direct closed-loop identification stemming from misspecification of the noise model structure. Specifically, we can re-write the CD model as follows, given the particular diagonal noise model in (5.4) and the decomposition of $\mathbf{G}^o$ in (5.3),

$$\mathscr{S}_2 : A^o(q,\mathbf{a}^o)\mathbf{y}(t) = B^o(q,\mathbf{b}^o)\sum_{k=1}^{q^o} c_k^o \mathbf{E}_k \mathbf{u}(t-d) + \mathbf{e}^o(t), \tag{5.6}$$

where $A^o(q,\mathbf{a}^o) = 1/H^o(q)$ is a scalar polynomial showing the FIR representation of the inverse of noise model. We have

$$A^o(q,\mathbf{a}^o) = 1 + \sum_{k=1}^{n_a^o} a_k^o q^{-k}, \;\; \mathbf{a}^o = [a_1^o \; \ldots \; a_{n_a^o}^o]^T. \tag{5.7}$$

The polynomial $B^o(q,\mathbf{b}^o) = A^o(q,\mathbf{a}^o)g^o(q)$ is also parameterized with a FIR form,

$$B^o(q,\mathbf{b}^o) = \sum_{k=0}^{n_b^o} b_k^o q^{-k}, \;\; \mathbf{b}^o = [b_1^o \; \ldots \; b_{n_b^o}^o]^T. \tag{5.8}$$

We further define the parameter vector, $\theta^{oT} = [\mathbf{a}^{oT} \; \mathbf{b}^{oT} \; \mathbf{c}^{oT}] \in \mathbb{R}^{n_a^o+n_b^o+1+q^o}$. Strictly speaking, $A^o(q,\mathbf{a}^o)$ and $B^o(q,\mathbf{b}^o)$ shall be of infinite orders as they are the infinite series expansions of rational functions. However, under the stability assumption of $A^o(q,\mathbf{a}^o)$ and $B^o(q,\mathbf{b}^o)$, their coefficients decay to be negligible after sufficient lags. Therefore, in practice, it makes sense to use a finitely truncated form to perform the corresponding identifications. One can refer to [88, 89] for a rigorous treatment of the more general case with infinite impulse response coefficients. With above manipulations the CD process model is transformed into an ARX-Hammerstein structure, which is much easier to handle than the original Box-Jenkins-Hammerstein structure. However, the price to pay is the increased number of parameters to estimate in the high-order representation, which places more stringent requirements on the informativeness of closed-loop data.

5.2.4 The presence of feedback

The current optimization method is based on quadratic programming proposed in [12]. Typical constraints in the MPC algorithm include actuator limits, maximum change between successive control actions, constraints on the averaged actuator profile in an array and bounds for bending limits. According to [113], when some of these constraints are active and varying, the MPC will display a piecewise linear or even nonlinear behavior, depending on the formulation of objective functions. Hence, we denote the feedback as

$$\mathbf{u}(t) = \mathbf{k}(\mathbf{u}^{t-1}, \mathbf{y}^t, t), \tag{5.9}$$

where $\mathbf{u}^{t-1} = \{\mathbf{u}(1), \ldots, \mathbf{u}(t-1)\}$ and $\mathbf{y}^t$ is defined in an analogous way. Note that for closed-loop identification with routine operating data where external excitations and setpoint changes are absent, nonparametric identification methods often yield the controller inverse as a process model estimate [94]. One remedy to prevent this is to impose the true time-delay to (5.6) when performing the high-order ARX identification. Therefore, we assume that the true time-delay is available throughout the derivations in this chapter. However, we stress that in practice, this stringent assumption can be relaxed and our mismatch detection scheme works even when the true time-delay is not available. In that case we just incorporate *a priori* knowledge of the true time-delay into the identification algorithm.

Another important concern in routine closed-loop identification is the identifiability. It has been discovered in [86, 93, 94] and in previous chapters that for linear feedback control, higher orders in the regulator and larger time-delay in the process generally enhance the informativeness of closed-loop data. The specific relationships among these factors have been fully investigated in these references. However, as commented in [15] (p. 432), time-varying or nonlinear regulators in (5.9) are usually enough to guarantee the informativeness of routine closed-loop data. The detailed conditions ensuring CD closed-loop identifiability will be presented later in this chapter.

5.3 Routine CD closed-loop identification

In this section we present a novel closed-loop routine CD identification approach that gives convergent and consistent estimates with routine closed-loop data. Our stress in this section is on the high-order ARX representation (5.6) of the original CD process. The basic techniques here adopt a similar idea as the separable

least-squares [114]: alternately identifying the spatial model $\mathbf{G}_0$ and temporal model $\{A_0(q), B_0(q)\}$, until the parameters converge. When identifying the spatial (or temporal) parameters, we fix the temporal (or spatial) parameters to the latest values.

5.3.1 Model parameterization

Based on previous analysis on $g^o(q)$, we parameterize the temporal model with a first-order model structure in the following form

$$g(q,\theta_T) = \frac{h}{1-fq},\ \theta_T \in \Omega_T, \tag{5.10}$$

where $\theta_T = [h\ f]^T$ is the temporal parameter and Ω_T is a compact set. Note that the time-delay d is absorbed into the input signal in (5.1). For the iterative identification algorithm in this work we mostly deal with the high-order ARX representation (5.6) of the original CD process. This model is parameterized as

$$\mathscr{M}:\ A(q,\mathbf{a})\mathbf{y}(t) = B(q,\mathbf{b})\mathbf{G}(\mathbf{c})\mathbf{u}(t-d) + \mathbf{e}(t), \tag{5.11}$$

with

$$A(q,\mathbf{a}) = 1 + \sum_{k=1}^{n_a} a_k q^{-k},\ \ B(q,\mathbf{b}) = \sum_{k=0}^{n_b} b_k q^{-k},\ \ \mathbf{G}(\mathbf{c}) = \sum_{k=1}^{p} c_k \mathbf{E}_k, \tag{5.12}$$

where $\mathbf{a} = [a_1\ \dots\ a_{n_a}]^T$, $\mathbf{b} = [b_0\ \dots\ b_{n_b}]^T$ and $\mathbf{c} = [c_1\ \dots\ c_p]^T$. n_a and n_b are the orders of the ARX model. q is the selected spatial order. The temporal model $\{A(q,\mathbf{a}),\ B(q,\mathbf{b})\}$ are assumed to be scalar transfer functions.

Now let us derive the predictor form of (5.11). We start with the i-th output channel $\mathbf{y}_i(t)$ and then generalize the results to the overall output. Define $\bar{\mathbf{u}}^k(t) = \mathbf{E}_k\mathbf{u}(t) \in \mathbb{R}^m$, $k = 1,\dots,p$. With the high-order ARX parameterization (5.11), the one-step-ahead prediction for the i-th output is

$$\hat{\mathbf{y}}_i(t|t-1) = -[A(q,\mathbf{a})-1]\mathbf{y}_i(t) + B(q,\mathbf{b})\sum_{k=1}^{p} c_k \bar{\mathbf{u}}_i^k(t-d),\ i = 1,\dots,m. \tag{5.13}$$

Straightforward calculations yield

$$\hat{\mathbf{y}}_i(t|t-1) = \psi_{y_i}(t)\mathbf{a} + \psi_{\bar{u}_i}(t-d)\mathbf{C}\mathbf{b},\ i = 1,\dots,m, \tag{5.14}$$

where

$$\begin{aligned}
\mathbf{C} &= diag\{\mathbf{c},\mathbf{c},\ldots,\mathbf{c}\},\\
\psi_{y_i}(t) &= [-\mathbf{y}_i(t-1)\ \ldots\ -\mathbf{y}_i(t-n_a)],\\
\psi_{\bar{u}_i}(t) &= \left[\bar{\mathbf{u}}_i^1(t)\ \ldots\ \bar{\mathbf{u}}_i^q(t)|\ldots|\bar{\mathbf{u}}_i^1(t-n_b)\ \ldots\ \bar{\mathbf{u}}_i^q(t-n_b)\right].
\end{aligned}$$

It then follows that the predictor form of overall output is

$$\hat{\mathbf{y}}(t|t-1) = \left[\psi_y(t)\ \psi_{\bar{u}}(t-d)\right]\begin{bmatrix}\mathbf{a}\\ \mathbf{Cb}\end{bmatrix}, \tag{5.15}$$

where

$$\psi_y(t) = \begin{bmatrix}\psi_{y_1}(t)\\ \vdots\\ \psi_{y_m}(t)\end{bmatrix},\ \ \psi_{\bar{u}}(t) = \begin{bmatrix}\psi_{\bar{u}_1}(t)\\ \vdots\\ \psi_{\bar{u}_m}(t)\end{bmatrix}.$$

5.3.2 Parameter Estimation

Consider a set of input-output data generated according to $\mathscr{S}_2$ under the controller (5.9),

$$\mathbf{Z}^N = \{\mathbf{y}(1),\mathbf{u}(1),\ldots,\mathbf{y}(N),\mathbf{u}(N)\}. \tag{5.16}$$

Denote $\theta^T = [\mathbf{a}^T\ \mathbf{b}^T\ \mathbf{c}^T] \in \mathbb{R}^{n_a+n_b+1+p}$ stacking all temporal and spatial parameters. We can formulate the loss function of parameter estimation as,

$$V_N(\theta) = \frac{1}{N}\sum_{t=1}^{N}\varepsilon^T(t,\theta)\varepsilon(t,\theta), \tag{5.17}$$

where $\varepsilon(t,\theta) \in \mathbb{R}^m$ is the prediction error,

$$\varepsilon(t,\theta) = \mathbf{y}(t) - \hat{\mathbf{y}}(t|t-1). \tag{5.18}$$

The optimal parameter estimate $\hat{\theta}_N$ is obtained by

$$\hat{\theta}_N = \arg\min_{\theta\in\Omega} V_N(\theta), \tag{5.19}$$

where $\Omega = \Omega_a \oplus \Omega_b \oplus \Omega_c$ is a compact and convex set. Ω_a, Ω_b and Ω_c are respectively compact and convex sets containing $\mathbf{a}$, $\mathbf{b}$ and $\mathbf{c}$. Note that solving the optimization problem (5.19) directly is not straightforward due to the coupling $\mathbf{Cb}$ in (5.15) which results in a nonconvex optimization. However, the separable structure of $\mathbf{C}$ and $\mathbf{b}$ motivates the usage of the separable least-squares technique. Fixing one parameter of $\mathbf{Cb}$, solving optimization with respect to the other is convex and this scheme leads to the iterative optimization approach. We will show later that under weak conditions this iterative identification scheme is convergent.

Another important observation of (5.18)-(5.19) is the non-identifiability issue featured for Hammerstein models. This is due to the fact that any pair $(\mathbf{b}/l, l\mathbf{c})$ yields the same model, $\forall l \neq 0$. In order to address this problem, a normalization of $\mathbf{b}$ or $\mathbf{c}$ has to be in place. In fact, for open-loop Hammerstein models that can be transformed into separable linear least-squares forms, the iterative identification algorithm can guarantee the convergence to stationary points, provided that a normalization is performed after each iteration [115]. This statement, with modifications, holds in our situation if certain conditions are satisfied. We will elaborate this argument in Theorem 5.3.1.

Our iterative identification algorithm to solve (5.19) is as follows. Denote the intial values of $\mathbf{a}$ and $\mathbf{b}$ as $\hat{\mathbf{a}}^i$ and $\hat{\mathbf{b}}^i$, respectively. We use $\hat{\mathbf{a}}^k$ to denote the estimate of $\mathbf{a}$ in the k-th iteration. It also holds true for the estimates of $\mathbf{b}$ and $\mathbf{c}$. Define the maximum iteration number as K. In each iteration k, $k = 1,\ldots,K$, first fix the spatial parameter to $\hat{\mathbf{c}}^{k-1}$ and perform a high-order ARX identification to (5.11) by solving

$$\{\hat{\mathbf{a}}^k, \hat{\mathbf{b}}^k\} = \arg\min_{a\in\Omega_a, b\in\Omega_b} V_N(\mathbf{a}, \mathbf{b}, \hat{\mathbf{c}}^{k-1}). \tag{5.20}$$

Note that the above optimization is an ordinary least-squares problem which is easy to solve. Before identifying spatial parameters, we choose to normalize $\hat{\mathbf{b}}^k$ after solving (5.20) by

$$\rho_k = sign\left(\hat{\mathbf{b}}^k(1)\right), \;\; \hat{\mathbf{b}}^k = \rho_k \frac{\hat{\mathbf{b}}^k}{\|\hat{\mathbf{b}}^k\|}, \tag{5.21}$$

to eliminate the parameter non-identifiability due to the coupling of $\mathbf{b}$ and $\mathbf{c}$. Then fix the temporal parameters

to $\{\hat{\mathbf{a}}^k, \hat{\mathbf{b}}^k\}$ and estimate the spatial parameter in (5.11) with another linear least-squares,

$$\hat{\mathbf{c}}^k = \arg\min_{\mathbf{c}\in\Omega_c} V_N(\hat{\mathbf{a}}^k, \hat{\mathbf{b}}^k, \mathbf{c}). \tag{5.22}$$

We then move forward to next iteration and carry out the same procedures as above. The estimated parameters after K iterations are defined as $\hat{\mathbf{a}} = \hat{\mathbf{a}}^K$, $\hat{\mathbf{b}} = \hat{\mathbf{b}}^K$, $\hat{\mathbf{c}} = \hat{\mathbf{c}}^K$ and denote $\hat{\theta}_N = [\hat{\mathbf{a}}^T\ \hat{\mathbf{b}}^T\ \hat{\mathbf{c}}^T]^T$. Note that to obtain an estimate for true temporal and spatial parameters, some extra identifications have to follow up. To this end, we first filter the input-output data by

$$\tilde{\mathbf{y}}(t) = A(q,\hat{\mathbf{a}})\mathbf{y}(t),\ \ \tilde{\mathbf{u}}(t) = A(q,\hat{\mathbf{a}})\mathbf{G}(\hat{\mathbf{c}})\mathbf{u}(t). \tag{5.23}$$

One can see that ideally, i.e., if $A(q,\hat{\mathbf{a}}) = A^o(q)$ and $\mathbf{G}(\hat{\mathbf{c}}) = \mathbf{G}^o$, from (5.1), (5.6), (5.11), it follows that, $\tilde{\mathbf{y}}(t) = g^o(q)\tilde{\mathbf{u}}(t-d) + \mathbf{e}^o(t)$. As will be shown in Theorem 5.3.1, $\hat{\mathbf{a}}$ and $\hat{\mathbf{c}}$ converge to the true parameter values asymptotically in the sample number N. Thus it is reasonable to estimate the temporal model $g^o(q)$ with filtered input $\tilde{\mathbf{u}}(t)$ and output $\tilde{\mathbf{y}}(t)$. We stress that if *a priori* information about the true temporal model structure is available, as in the CD process, a parsimonious model in (5.10) can be efficiently estimated by an output-error identification. Otherwise, we can estimate an FIR structure for the temporal model to eliminate the bias. For the CD process, we perform a multiple-experiment output-error identification to $g(q,\theta_T)$ in (5.10),

$$\tilde{\mathbf{y}}(t) = g(q,\theta_T)\tilde{\mathbf{u}}(t-d) + \mathbf{e}(t), \tag{5.24}$$

and denote the parameter estimate as $\hat{\theta}_T = [\hat{h}\ \hat{f}]^T$. The next procedure is to re-scale the spatial and temporal parameters by

$$\hat{\mathbf{c}} = \hat{\mathbf{c}}\hat{f}/(1-\hat{g}). \tag{5.25}$$

The rational behind the re-scaling step (5.25) is that $g(q,\theta_T)$ is discretized from a continuous first-order transfer function and shall have a unit step response at steady-state (cf. (5.2)). With the acquired $\hat{\mathbf{c}}$, we can easily identify the spatial parameter θ_S in (1.2) by standard nonlinear least-squares. The entire algorithm is summarized in Table 5.1.

Table 5.1: The implementation of routine CD closed-loop iterative identification

Algorithm of routine CD closed-loop identification	
Input:	Set $\hat{\mathbf{a}}^0 \leftarrow \mathbf{a}^i$, $\hat{\mathbf{b}}^0 \leftarrow \mathbf{b}^i$ and $\hat{\mathbf{c}}^0 \leftarrow \mathbf{c}^i$. $K \leftarrow$ maximum iteration number.
Loop:	**for** $k = 1, \ldots,$ K, **do**
1:	Fix the spatial parameter $\hat{\mathbf{c}}^{k-1}$, and estimate parameters of the high-order ARX part in (5.11) by solving the least-squares problem (5.20);
2:	Normalize $\hat{\mathbf{b}}^k$ as in (5.21);
3:	Fix the temporal parameter $\{\hat{\mathbf{a}}^k, \hat{\mathbf{b}}^k\}$, and estimate the spatial parameter in (5.11) by solving the nonlinear least-squares problem (5.22);
End for	
4:	$\hat{\mathbf{a}} = \hat{\mathbf{a}}^K$, $\hat{\mathbf{b}} = \hat{\mathbf{b}}^K$, $\hat{\mathbf{c}} = \hat{\mathbf{c}}^K$. Filter the input-output data as in (5.23);
5:	Estimate the temporal model $g(q, \theta_T)$ with $\tilde{\mathbf{y}}(t)$ and $\tilde{\mathbf{u}}(t)$ by an output-error identification (5.24);
6:	Re-scale $\hat{\mathbf{c}}$ based on (5.25) and identify the spatial parameter θ_S in (1.2);
Output:	Parameter estimates $\hat{\theta}_S$, $\hat{\theta}_T$, $\hat{\mathbf{a}}$ and noise covariance.

5.3.3 Convergence and consistency analysis

Now let us consider the convergence and consistency of the proposed iterative identification algorithm. Before presenting the main results, we need certain restrictions on the quality of closed-loop data. We have discussed the closed-loop identifiability problem in Section 5.2 for a generic process that is free of any external excitations. It shows that high-order linear, time-varying or nonlinear regulators are beneficial for direct identification by enriching the information content in routine operating data. Now we are in a place to explore the detailed requirements on CD closed-loop data arising from these conditions. Specifically, we have the following assumptions.

Assumption 5.3.1. The input-output data $\mathbf{Z}^N$ is bounded and generated according to the stable closed-loop system $\mathscr{S}_1$ (or equivalently $\mathscr{S}_2$) and (5.9), where $N >> n_a^o + n_b^o$ and $\mathbf{e}^o(t)$ is Gaussian white noise vector. In addition, it is assumed that the model structure (5.11)-(5.12) is uniformly stable $\forall \theta \in \Omega$.

Assumption 5.3.2. The parameterized model (5.11)-(5.12) has the same structure as the true model (5.6)-(5.8), i.e., $n_a = n_a^o$, $n_b = n_b^o$ and $q = q^o$, and the true model is contained in the selected model structure $\theta^o \in \Omega$. Moreover, we assume the polynomial pairs $\{A^o(q), B^o(q)\}$ and $\{A(q, \mathbf{a}), B(q, \mathbf{b})\}$ are coprime.

Assumption 5.3.3. Assume that the closed-loop data $\mathbf{Z}^N$ is informative enough for the relevant closed-loop identification. This assumption involves the following aspects:

(a). The closed-loop input data $\mathbf{u}^N$ is strongly persistently exciting with orders at least n_b over the basis

matrices $\mathbf{E}_k, k = 1, \ldots, p$. In other words,

$$rank\ \Phi_u = p(n_b+1),\ \ \Phi_u = \begin{bmatrix} \psi_{\bar{u}}(1) \\ \vdots \\ \psi_{\bar{u}}(N) \end{bmatrix}, \tag{5.26}$$

that is, Φ_u has full column rank for any large N. This is similar to the persistent excitation requirement for input signals in open-loop identification.

(b). There does not exist a common linear time-invariant feedback relationship between inputs and outputs over all channels. It is formally stated as

$$\overline{\mathbb{E}}\,\|R(q)\mathbf{G}(\mathbf{c})\mathbf{u}(t-d)+S(q)\mathbf{y}(t)\|^2 > 0,\ \ \forall \mathbf{c} \in \Omega_c, \tag{5.27}$$

where $R(q)$ and $S(q)$ are arbitrary scalar linear filters, and $\overline{\mathbb{E}}$ is the generalized expectation operator. Note that this condition is equivalently stating that all output channels do not share the same feedback regulator.

Note that the above assumptions are fairly loose. In particular, for Assumption 3a, it is easy to meet the persistent exciting requirement (5.26) since in closed-loop the input signal is filtered white noise that contains enough excitations to make Φ_u full column rank, especially when N is large. For Assumption 3b, all input-output channels have to share the same regulator in order to make (5.27) invalid. This assumption becomes more convincing given that most CD MPC has complex dynamics due to the complexity in the associated optimization and constraints [112].

We present the following theorem showing the convergence of proposed iterative CD closed-loop identification and asymptotic properties of the parameter estimator.

Theorem 5.3.1. *Consider the data* $\mathbf{Z}^N$ *generated according to the stable closed-loop system* (5.6) *and* (5.9). *Suppose that Assumptions* (5.3.1)-(5.3.3) *are true. We further assume that the parameter estimates* $\hat{\mathbf{a}}^k \neq 0$, $\hat{\mathbf{b}}^k \neq 0$, $\hat{\mathbf{c}}^k \neq 0$ *during all iterations. Then the following statements on the algorithm 5.1 of routine CD closed-loop identification hold:*

(i) For the iterative identification algorithm 5.1 with normalization (5.20)-(5.22)*, the parameter estimate sequence* $\{\hat{\theta}_N^k\}$ *is convergent to stationary points of* $V_N(\theta)$ *for any large* $N >> n_a + n_b$ *if it converges,*

i.e.,

$$\hat{\theta}_N^k \to \hat{\theta}_N, \ \ as\ k \to \infty, \tag{5.28}$$

where $\nabla V_N(\hat{\theta}_N) = 0$.

(ii) The loss function $V_N(\theta)$ *converges uniformly to the limit function* $\overline{V}(\theta)$ *asymptotically in the sample number, namely,*

$$\sup_{\theta \in \Omega} |V_N(\theta) - \overline{V}(\theta)| \to 0, \ \ w.p.1\ as\ N \to \infty, \tag{5.29}$$

where $\overline{V}(\theta) = \overline{\mathbb{E}}[\varepsilon^T(t,\theta)\varepsilon(t,\theta)]$. *As a result,*

$$\hat{\theta}_N \to \theta^*, \ \ w.p.1\ as\ N \to \infty, \tag{5.30}$$

where $\theta^* = \arg\min_{\theta \in \Omega} \overline{V}(\theta)$.

(iii) The parameter estimate $\hat{\theta}_N$ *is consistent, that is,*

$$\hat{\theta}_N \to \theta^o, \ \ w.p.1\ as\ N \to \infty, \tag{5.31}$$

where θ^o *is the true parameter value.*

Proof. Please see C.1.

Remark 5.3.1. Note that the convergence in (i) of Theorem 5.3.1 the iterative identification algorithm still holds even when the assumptions on the informativeness of closed-loop data are not satisfied [116]. Moreover, it is shown in [115] that the accumulated points of $\{\hat{\theta}_N^k\}$ are stationary points of $V_N(\hat{\theta})$ if a general convergence on the sequence $\{\hat{\theta}_N^k\}$ cannot be achieved.

5.4 Application of one-class SVM to CD mismatch detection

We can attain consistent parameter estimates for the spatial, temporal and noise models with the iterative closed-loop identification approach presented previously. This serves as the major building block for our SVM based mismatch detection framework. Specifically, we will implement the mismatch detection method simultaneously to each of these models to examine the corresponding model changes. With this in mind, the following presentation is exclusively devoted to showing the detection of mismatch for the temporal model.

All procedures below apply to the detection of mismatch for noise model and spatial model as well. In practice, we have to monitor these three models in parallel so as to distinguish the noise model change from MPM and raise mismatch alarms appropriately.

5.4.1 SVM training

We use the temporal models estimated from moving windows in the training data as the training models, denoted as $\{\mathbf{x}_1,\ldots,\mathbf{x}_l\}$. l is the number of moving windows in the training data set. Each $\mathbf{x}_i$ stands for an FIR coefficient vector of one estimated temporal model from the i-th moving window,

$$\mathbf{x}_i = [\hat{x}_i^1 \ \ldots \ \hat{x}_i^{n_g}]^T, \tag{5.32}$$

where $\hat{x}_i^k$, $k = 1,\ldots,n_g$, is the k-th FIR coefficient and n_g is the order. Applying (3.20)-(3.21) to the training data $\{\mathbf{x}_1,\ldots,\mathbf{x}_l\}$ yields a one-class SVM prediction model (3.24). Notice that in principle, larger training data set provides better descriptions of the boundary of the nominal cluster. However, in practice, we may encounter situations where only very limited training data sets are available, as in the MD MPM detection case. One remedy to overcome this issue is to use historical data. However, this idea would fail if the historical data is not accessible or was not saved, which is not uncommon in the industry. Another solution to this problem is enlarging the training data by re-sampling according to the probability distribution of parameter estimates. To this end, here we propose a simple re-sampling technique. It has been shown in [117] that parameter estimates from the separable nonlinear least-squares method are Gaussian distributed (if the noise is Gaussian) and this arguments can also be extended to our iterative closed-loop identification algorithm with minor modifications. Based on this statement, we can construct rough estimators for the mean μ_k and variance σ_k of each FIR coefficient $\hat{x}^k$,

$$\hat{\mu}_k = \mu(\hat{x}_1^k,\ldots,\hat{x}_l^k), \ \ \hat{\sigma}_k = \sigma(\hat{x}_1^k,\ldots,\hat{x}_l^k), \ \ k = 1,\ldots,n_g, \tag{5.33}$$

where a common choice for $\mu(\cdot)$ and $\sigma(\cdot)$ are the sample mean and sample variance. It is apparent that if the number of training models is small due to limited training data, the variance estimator in (5.33) is conservative relative to the true variance. A proper scaling factor α_T (subscript T means temporal) of $\hat{\sigma}_k$ is necessary. The rule of thumb in selecting α_T is: if we have a large set of training data, α_T is small;

otherwise, α_T is large. One can also expect that larger scaling factor makes the mismatch detection algorithm less sensitive to mismatch and vice versa. After scaling the variance estimator, we can re-sample from the obtained density function to generate a large number of training models and then train a one-class SVM based on these augmented data. Note that in the case where plenty of historical data are available, the re-sampling strategy may not be necessary.

5.4.2 SVM prediction

Similar to the SVM training stage, we slide moving windows along the test data and perform a closed-loop identification in each window. Then use the trained SVM model to predict whether the currently estimated model can be classified into the initial cluster of normal model estimates. Given the test data point $\mathbf{x}$ (a FIR coefficient vector), $p(\mathbf{x})$ in (3.24) computes the functional distance of this point to the initial cluster and such distance is known as a score. We can use the sign of this score to classify $\mathbf{x}$. Positive scores mean the underlying test points can be grouped into the initial cluster and thus show no mismatch. Otherwise, they are seen as indications of mismatches. Define I_t as the sign of score for the test moving window at time t. The users, in practice, tend to be very cautious in raising the MPM alarm since the subsequent closed-loop identification is expensive. Therefore, the accumulated number of negative scores over last few moving windows is a more reasonable metric to indicate the occurrence of MPM. This accumulated metric is defined as

$$s_{MPM} := \frac{I_-}{n_T}, \tag{5.34}$$

where $I_- := \{I_i = -1 : i \in T_t\}$ with $T_t := \{t - n_T, \ldots, t-1, t\}$. Here the user-defined term n_T means that the last n_T moving windows will be used to compute s_{MPM}. The users can specify a conservative threshold on s_{MPM}, e.g, 0.95, to be circumspect on raising MPM alarms.

5.5 Examples

In this section, we will provide examples from a single-array CD process of paper machines to verify the proposed iterative CD closed-loop routine identification algorithm and the one-class SVM mismatch detection approach. These examples are conducted on Honeywell paper machine simulators which highly resemble practical paper machines.

Table 5.2: Tuning parameters of the CD MPC

Tuning parameters	Values	Tuning parameters	Values
CV target weight	0.40	MV temporal movement weight	0.25
MV target weight	0.17	MV spatial picketing weight	0.14
CV target value	42	MV target value	0
Prediction horizon	25	Control horizon	4
Actuator bend limit	30	Actuator upper/lower average	± 1
Actuator change rate limit	15	Actuator upper/lower limit	± 20

5.5.1 Example 1: Iterative CD closed-loop routine identification

For this particular CD process, the opening of autoslice (MV) is manipulated to alter the amount of pulp slurry distributed across the sheet, which ultimately affects the dry weight (CV) of the paper sheet being produced. There are 222 measurement boxes and 74 actuators along the cross direction. The selected sampling interval is 12 seconds and the continuous time constant is 126.4352 seconds. After discretization, the true CD process has temporal and spatial parameters as follows:

$$f^o = 0.9095, \;\; \theta_S^o = [0.3802 \;\; 268.6414 \;\; 0.10 \;\; 1.5]^T, \;\; d = 2.$$

The controller that is being used in the simulation is CD MPC. Please refer to [12] for details on the explicit formulation of this MPC. Note that there are four types of constraints involved in the adopted MPC: bend limits for neighboring actuators, bound limits for the actuator average profile, upper and lower limits for the actuator profile, and limits of the change rate of actuators. Tuning parameters specified for the MPC are demonstrated in Table 5.2. The true noise is chosen as a high-pass filter

$$\mathbf{v}^o(t) = \frac{1 - 0.6q^{-1} + 0.3q^{-2} - 0.1q^{-3}}{1 + 0.4q^{-1} + 0.1q^{-2} + 0.05q^{-3}} \mathbf{I}\mathbf{e}^o(t),$$

where $\mathbf{e}^o(t)$ is Gaussian white noise with zero mean and non-diagonal covariance matrix Σ. The variance at each output channel is 0.01. The relevant simulation parameters are demonstrated in Table 5.3 (note that Table 5.3 also contains several MPM detection parameters that will be used in Example 5.5.2). We further assume that there is no MPM in this simulation. To verify the effectiveness of the proposed closed-loop CD identification algorithm with routine operating data, we leave the setpoint unchanged during the entire simulation, i.e., the noise is the only external signal to the system. We also suppose that the true process delay is available and is incorporated into the identification algorithm to avoid estimating the inverse of controller

Table 5.3: Simulation and MPM detection parameters for Example 1 and Example 2

Parameters	Values	Parameters	Values
Actuator zone width	62.5194 mm	CD bin windth	20.8398 mm
Sampling interval	12 seconds	Iteration number	5
Initial temporal θ_T^i	[0.82 0.18]	Initial spatial θ_S^i	[0.3 200 0.2 4.0]
Window size	80 min	Window step size	20 min
Training data size	800 min	Temporal α_T	3
Spatial α_S	1.5	Noise α_N	3
Time noise model changes	1200^{th} min	Time MPM occurs	1600^{th} min

as the process model. With the above setting, the simulation of closed-loop system lasts for 120 minutes (600 samples of input-output data). Plots of input and output data from simulation are shown in Figure 5.1 below. Initially, the controller manipulates the actuator array to attenuate the steady-state disturbances acting on the output. After this transient part the whole closed-loop system enters a steady-state mode and thus we select the last 400 samples of data to perform the closed-loop identification.

The initial spatial and temporal parameters for the identification algorithm are shown in Table 5.3. We find that similar to most open-loop Hammerstein model identifications, our algorithm converges very fast to the local minimum in just a few iterations. The maximum iteration number is set to $K = 5$. For the temporal model, we choose $n_a = 20$, $n_b = 50$. The spatial order is selected as $p = 30$. The users may require trial-and-error in implementing our algorithm in practice and empirical insights into the noise characteristics are valuable in choosing these orders. In addition, proper regularizations are necessary in executing this algorithm in order to smooth the estimated FIR coefficients. The regularization can also ensure the numerical stability incurred with the high-order least-squares problem (5.20) when the regressor matrix has large condition number. Table 5.3 summarizes relevant parameters chosen for these two examples studied in this section.

The top-left plot of Fig. 5.2 demonstrates the impulse response of the estimated inverse of noise model versus that of the true inverse of noise model. As expected, these two lines are fairly close to each other which indicates that the estimated noise model is accurate. After steps 4-6 in Algorithm 5.1, the estimated values of temporal and spatial parameters are

$$\hat{f} = 0.9060, \;\; \hat{\theta}_S = [0.3442 \;\; 277.0566 \;\; 0.0694 \;\; 1.7889]^T.$$

One can see that these parameter estimates are very precise. In the SVM-based mismatch detection, we

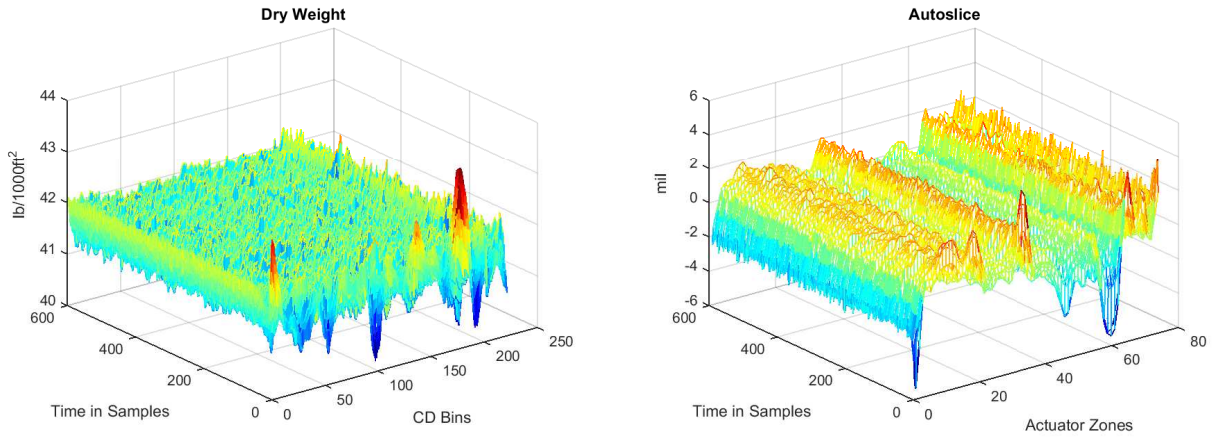

Figure 5.1: Simulated input-output data for the closed-loop CD process

are more interested in the FIR coefficients of these models. The next two plots on the left side of Fig. 5.2 demonstrate the computed impulse responses of both spatial and temporal models against those of the true models. It is apparent that all these estimated impulse responses coefficients approximate the true ones with high accuracy. More importantly, the noise model and process model can be independently estimated, which paves a way to discriminate the MPM from noise model change. As an additional test, we change the noise model into a low-pass filter

$$\mathbf{v}^o(t) = \frac{1+0.7q^{-1}+0.4q^{-2}}{1-0.5q^{-1}+0.1q^{-2}}\mathbf{I}\mathbf{e}^o(t),$$

and repeat the closed-loop identification procedures above. The corresponding identification results are shown in the right plot of Fig. 5.2. Once again, the estimated impulse responses are very close to the true responses. These results verify the effectiveness of our proposed CD closed-loop identification method.

5.5.2 Example 2: One-class SVM model-plant mismatch detection

In this example, we continue studying the previous closed-loop CD simulation but shift our attention to the mismatch detection. The main simulation parameters stay the same as those in Example 5.5.1. Table 5.3 also lists other parameters that are specific to the CD MPM detection algorithm. It is worth pointing out that here we choose a relatively small spatial scaling factor α_S to increase the sensitivity of our MPM detection algorithm in detecting spatial mismatches. During the steady-state operation, the spatial mismatch is relatively important as it directly determines the steady-state control performance. In this example, we put our emphasis on the spatial mismatch detection.

The simulation logic for this example is elaborated as follows. Initially there is neither MPM nor noise

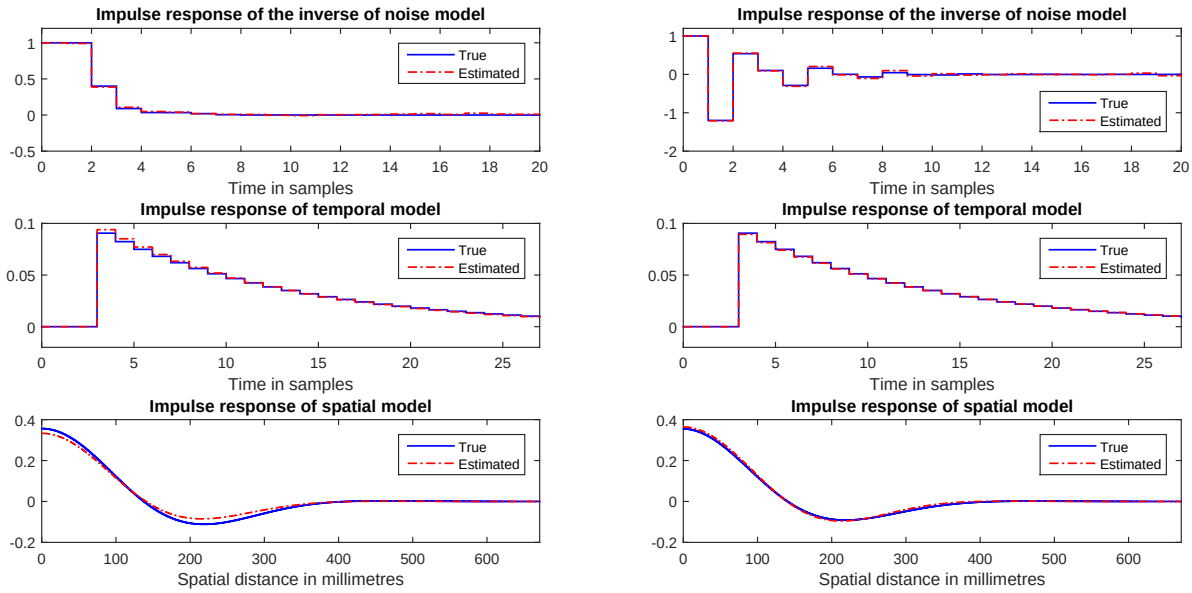

Figure 5.2: CD closed-loop iterative identification results: noise model is a high-pass filter (left); noise model is a low-pass filter (right);

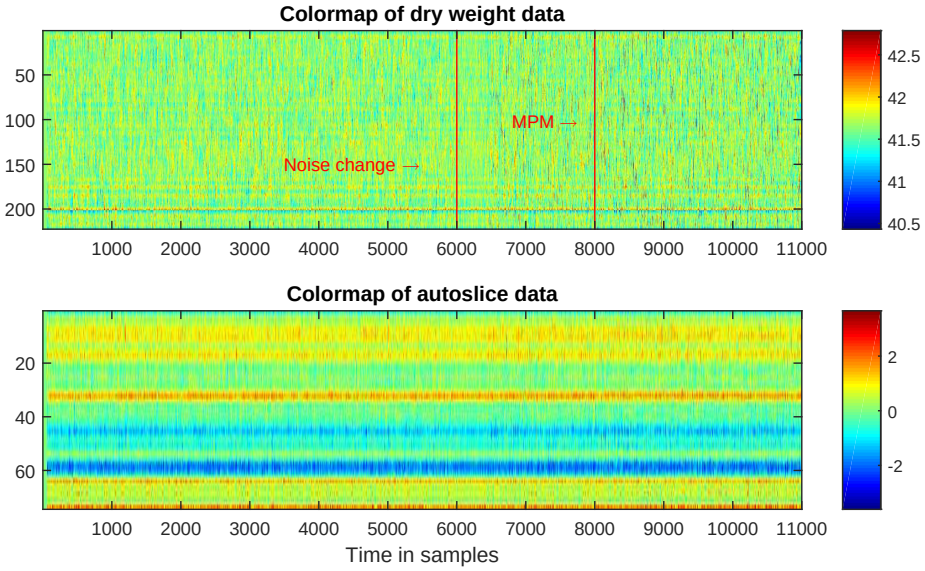

Figure 5.3: The colormap of simulated input-output data for CD MPM detection

model change and the noise model is chosen as $H^o(q) = (1-0.6q^{-1})/(1+0.4q^{-1})$. After disposing the initial transient part due to attenuating the steady-state disturbance, we use the first 4000 samples of data (cf. Table 5.3) as the training data. Apply moving windows to the training data and identify spatial, temporal and noise models from each moving window. Each of these moving windows contain 400 samples and a step size of 100 samples. Once this step is complete we train one-class SVMs separately to these models and obtain the corresponding prediction functions. Notice that this procedure involves scaling the initial cluster and re-sampling. From then on, the SVMs start to predict mismatches. After 6000 samples, we *gradually* switch the noise model into $H^o(q) = (1+0.7q^{-1})/(1-0.5q^{-1})$. At the 8000^{th} sample, the width parameter of true plant begins to increase, *gradually* to 1.5 times of the original value after 300 samples. Then the true width parameter settles at the new value thereafter. As a comparison, we add an online user-specified performance index to monitor the output variance [118]. Note that throughout this simulation there is no setpoint change or any other external excitation.

The colormaps of simulated input and output data are shown in Fig. 5.3. We highlight the time at which we begin to introduce the noise model change and spatial MPM. It is clear that the output variance inflates after introducing the noise model change and increases furthermore after adding the MPM. Fig. 5.4 illustrates the spatial and temporal parameter estimates over all moving windows where the red dash-dotted line in each plot shows the true parameter value over time. The blue lines display the estimated parameter values in each moving window. Although these parameter estimates are subject to large variance due to low excitation levels in the routine closed-loop data, it still provides valuable insights for the operators on which parameter may have drifted. Moreover, this closed-loop identification algorithm can easily carry over to the data collected during closed-loop identification experiment. This means that if a closed-loop identification is necessary, we only need to start injecting external excitations to the system, with the closed-loop identification algorithm operating continuously.

Fig. 5.5 displays the detailed mismatch detection results. As expected, the user-specified performance index is extremely sensitive to the changes in output variance, whether they are caused by noise model change or by MPM. It starts to drop obviously after the noise change even before the MPM is added. This is the main drawback of using user-specified or other variance-based performance index to examine the happening of MPM: they are not able to distinguish noise model change from MPM. In contrast, the scores obtained from SVM predictions can clearly indicate whether it is a noise model change or a MPM. Since it monitors three models independently, we can significantly reduce the number of false alarms on MPM due to noise

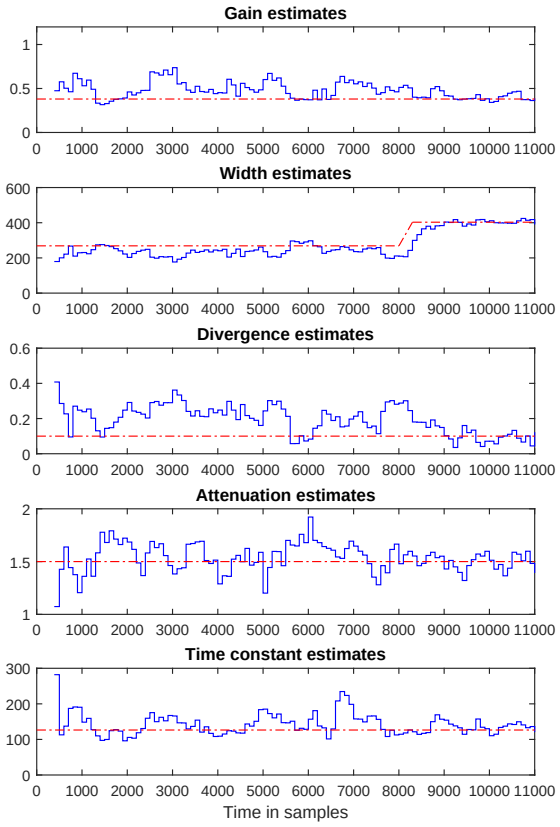

Figure 5.4: Process parameter estimates over moving windows

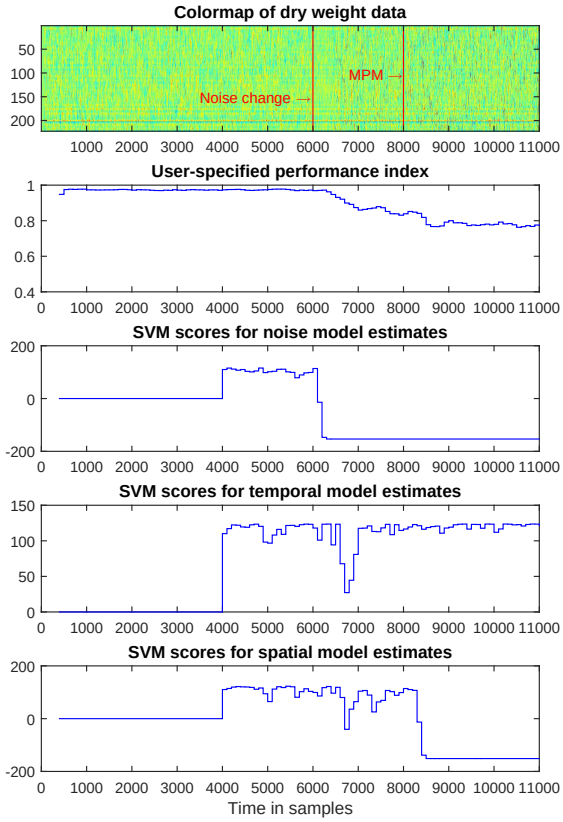

Figure 5.5: MPM and noise model change detection results

model changes. Notice that occasionally there may be several negative scores which implies a mismatch in the underlying moving window. These outliers shall not affect our decisions regarding the MPM. As pointed out in Section 3.5.3 and Section 5.4.2, we shall use the accumulated score metric (5.34) to raise the mismatch alarm, instead of any single negative score observed occasionally.

5.6 Summary

In this chapter, we present a novel closed-loop identification method that can provide consistent parameter estimates for the CD process. It is applicable to the routine operating data that lack external excitations, given that a set of weak conditions on the informativeness of closed-loop data are satisfied. For the CD MPM detection, we split the routine operating data into training and test stages. The closed-loop identification

method is implemented in moving windows continuously over both stages. We then develop one-class SVM models based on the clusters of model estimates from the training data. Such SVM models are then used to predict classifications of models estimated from the test data. From the predictions, we are able to detect the presence of MPM. Moreover, this approach enables us to monitor the changes in process and noise models separately, thus our detection results on MPM are robust to noise model changes. Two simulation examples are presented to validate the effectiveness of the proposed methods.

Chapter 6

Closed-loop Optimal Input Design for CD Processes

6.1 Introduction

For CD processes, most existing input design results focus on the open-loop case, see [71]. The main drawback of open loop input design is the resultant production loss as the normal operations of the process risk being interrupted. Results on closed-loop optimal input design for CD processes are scarce, with current industrial practice of using spatial-bump-temporal-PRBS signals as excitation signals for closed-loop identification (denoted as "bump excitation" in this work) [72].

In this chapter, we design excitation signals for the CD process with optimal input design techniques. In particular, we focus primarily on input design for the steady-state CD process model, in light of the fact that mostly the CD process operates at steady-state. The major challenge lies in how to represent the closed-loop CD process with a parsimonious parametric model to avoid large input-output dimensions. Inspired by [82], we propose to develop a scalar noncausal model for the closed-loop CD process to resolve this issue. Furthermore, we demonstrate that a causal model can be obtained and it is equivalent to the noncausal model in the sense of same output spectrum. It is further shown that the maximum likelihood estimate and parameter covariance matrix of the causal-equivalent model converge to those of the noncausal model asymptotically with probability one. In this sense, the optimal excitation signal can be designed based solely on the causal model.

This chapter is outlined as follows. In Section 6.2, we present the CD steady-state model. In Section 6.3, we illustrate detailed procedures to develop a scalar causal-equivalent model for the closed-loop CD process. In Section 6.4, the optimal input design procedures are demonstrated based on the causal-equivalent model, followed by a simulation example in Section 6.5 to verify the proposed results.

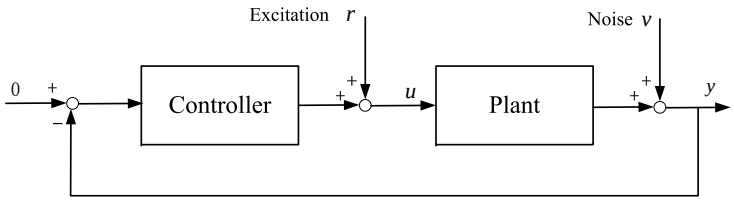

Figure 6.1: The closed-loop optimal input design configuration

6.2 Preliminaries

6.2.1 Open-loop CD process model

In this work, we consider the following classical CD process model,

$$\mathbf{y}(t) = g(q)\mathbf{G}\mathbf{u}(t) + \mathbf{v}(t), \tag{6.1}$$

where $\mathbf{y}(t) \in \mathbb{R}^m$ and $\mathbf{u}(t) \in \mathbb{R}^m$ are the CV and MV profiles. Note that here we assume, without loss of generality, that the dimensions of output and input profiles are equal. The results in this chapter can be easily extended to the more general case in which theirs dimensions are different. $\mathbf{v}(t)$ is the colored measurement noise. $\mathbf{G} \in \mathbb{R}^{m\times m}$ is the steady-state gain matrix. In this chapter, we pose the following assumptions on the structure of $\mathbf{G}$ matrix. The diagram of closed-loop optimal input design for steady-state CD processes is shown in Fig. 6.1.

Assumption 6.2.1. All actuators of the CD process have the same symmetric impulse response in the spatial direction at steady-state. The columns of $\mathbf{G}$ matrix are indeed sampled version of these responses. Thus $\mathbf{G}$ matrix is Toeplitz-structured.

For the purpose of spatial optimal excitation signal design, the following steady-state CD process model is of interest,

$$\mathbf{y}_{ss} = \mathbf{G}_{ss}\mathbf{u}_{ss} + \mathbf{v}_{ss}, \tag{6.2}$$

where $\mathbf{y}_{ss} \in \mathbb{R}^m$ is the steady-state measured CV profile, and $\mathbf{u}_{ss} \in \mathbb{R}^m$ is the steady-state MV profile. $\mathbf{G}_{ss} = \mathbf{G}$ is the steady-state process gain. $\mathbf{v}_{ss} = \phi\mathbf{e} \in \mathbb{R}^m$ is the steady-state output disturbance, where $\mathbf{e} \in \mathbb{R}^m$ is the spatial noise. For convenience, we suppose that the spatial filter ϕ is also Toeplitz-structured and sparse as $\mathbf{G}_{ss}$.

6.2.2 Closed-loop steady-state CD process model

Designing closed-loop dither signals requires an explicit expression of the controller to formulate the objective function of input design. It is well-known that CD MPC may display time-varying or even nonlinear dynamics if any constraint is active. Thus input design for closed-loop MPC systems involving active constraints is non-trivial. In this work, to simplify this problem we introduce the following assumption.

Assumption 6.2.2. The MPC is assumed to operate in a linear mode with no active constraints.

A typical MPC cost for CD process is expressed as [12]

$$\begin{aligned}\min_{\Delta\mathbf{u}(k)} J(k) \quad = \quad & \min_{\Delta\mathbf{u}(k)} \left\{ \sum_{j=1}^{H_p} \left[\hat{\mathbf{y}}(k+j) - \mathbf{y}_{sp}(k+j)\right]^T \mathbf{Q}_1 \left[\hat{\mathbf{y}}(k+j) - \mathbf{y}_{sp}(k+j)\right] + \right. \\ & \left. \sum_{j=0}^{H_u-1} \left[\Delta\mathbf{u}(k+j)^T \mathbf{Q}_2 \Delta\mathbf{u}(k+j) + \mathbf{u}(k+j)^T \mathbf{Q}_3 \mathbf{u}(k+j)\right] \right\}, \end{aligned} \tag{6.3}$$

where H_p and H_u are the prediction and control horizons. $\mathbf{y}_{sp}(k)$ is the target value for output at time k. $\hat{\mathbf{y}}(k)$ is the predicted output value at time k. $\Delta\mathbf{u}(k)$ is the changes in actuator profile at time k and $\mathbf{u}(k)$ is the input profile. $\mathbf{Q}_1$, $\mathbf{Q}_2$ and $\mathbf{Q}_3$ are diagonal weighting matrices for controlled properties, changes in actuator array and the actuator array, respectively.

With Assumption 6.2.2, the closed expression of MPC is shown to be [12]

$$\mathbf{K}_{ss} = -\mathbf{Q}_3^{-1} \alpha_K \mathbf{G}_{ss} \mathbf{Q}_1, \tag{6.4}$$

where $\mathbf{Q}_1$ is the weight matrix in MPC objective function penalizing the deviation of CV profile from its setpoint. $\mathbf{Q}_3$ is the corresponding weight matrix to penalize the offset of steady-state MV from its target. α_K is a constant determined from the dynamic model of actuators. In practice the weighting matrices $\mathbf{Q}_1$ and $\mathbf{Q}_3$ are often chosen to be diagonal. Assuming that $\mathbf{Q}_1$ and $\mathbf{Q}_3$ are diagonal, the controller $\mathbf{K}_{ss}$ then has a matrix structure similar to that of gain matrix $\mathbf{G}_{ss}$. The structural similarity between $\mathbf{K}_{ss}$ and $\mathbf{G}_{ss}$ will be used in the derivations below.

Remark 6.2.1. While Assumption 6.2.2 seems to be a restrictive assumption in practical implementation of our algorithm, industrial experience reveals that a well-tuned CD MPC normally operates without active constraints. Extension of our study to incorporate active constraints will be a consideration in our future work.

Combining (6.2) and (6.4), we can easily arrive at the following closed-loop CD process (cf. Fig. 6.1)

$$\mathbf{y}_{ss} = (\mathbf{I}+\mathbf{G}_{ss}\mathbf{K}_{ss})^{-1}\mathbf{G}_{ss}\mathbf{K}_{ss}\mathbf{r}+(\mathbf{I}+\mathbf{G}_{ss}\mathbf{K}_{ss})^{-1}\mathbf{v}_{ss}, \tag{6.5}$$

$$\mathbf{u}_{ss} = (\mathbf{I}+\mathbf{K}_{ss}\mathbf{G}_{ss})^{-1}\mathbf{r}-(\mathbf{I}+\mathbf{K}_{ss}\mathbf{G}_{ss})^{-1}\mathbf{K}_{ss}\mathbf{v}_{ss}, \tag{6.6}$$

where $\mathbf{r}\in\mathbb{R}^m$ is the spatial excitation signal to be designed.

6.2.3 Spatial optimal input design for the CD process

When it comes to spatial optimal input design, the parameters of interest here are those in the gain matrix $\mathbf{G}_{ss}$ (or more specifically, the parameters in a column of $\mathbf{G}_{ss}$). However, optimal input design directly based on the closed-loop model (6.5)-(6.6) is non-trivial due to the large input-output dimensions as well as the large number of parameters in $\mathbf{G}_{ss}$. To circumvent this problem, we propose to use a scalar transfer function along the spatial coordinate to represent the steady-state response of CD actuators. In this sense, the original optimal input design aimed for the MIMO CD model can be re-formulated into that for the scalar spatial model, which significantly reduces the complexity. However, the disadvantage is that this scalar spatial transfer function has to be noncausal to capture the responses of actuators on both sides (see Fig. 6.2), analogous to the 'past' and 'future' in the conventional time coordinate. We provide theoretical basis showing that the noncausal model can be further converted to a causal-equivalent model such that the input design can be performed based on this causal model.

6.3 Causal scalar transfer function representation of the CD process

6.3.1 Noncausal scalar model of the closed-loop CD process

From the aforementioned structure of $\mathbf{G}_{ss}$ as well as Assumption 6.2.1, one is readily able to extract a scalar noncausal FIR model from any single column of $\mathbf{G}_{ss}$ to represent the spatial impulse response of an actuator

$$g(\lambda,\lambda^{-1}) = g_{-n}\lambda^{-n}+\ldots+g_0+\ldots+g_n\lambda^n, \tag{6.7}$$

where $n<m$ is a truncated index representing significant coefficients. The positive and negative powers of λ denote the anti-causal and causal shifts, respectively. The $g_i,\ i=-n,\ldots,n$, are spatial impulse response

coefficients and in general symmetry of these coefficients is enforced, i.e., $g_i = g_{-i}$. Since in most cases the noncausal FIR model (6.7) has a high order (i.e., n is large), a parsimonious noncausal transfer function is necessary to simplify this model. First the following assumption is present.

Assumption 6.3.1. The complex trigonometric polynomial (6.7) has real and symmetric coefficients. Moreover, this polynomial is positive at any points on the unit circle $|\lambda| = 1$.

Remark 6.3.1. Assumption 6.3.1 is posed to facilitate the conversion of the noncausal model into a causal equivalent model in the following sections. Although this assumption does not admit a physical motivation or interpretation, it is a fairly loose condition as most practical actuator impulse response shapes in spatial direction can satisfy this condition or be approximated by a curve satisfying such requirement.

With this assumption it follows from the Fejér-Riesz Theorem that we can factorize $g(\lambda, \lambda^{-1})$ as

$$g_{-n}\lambda^{-n} + \ldots + g_0 + \ldots + g_n\lambda^n = M(\lambda)M(\lambda^{-1}),\ \forall \omega, \tag{6.8}$$

where $\lambda = e^{j\omega}$. Here $M(\lambda^{-1})$ has the following expression

$$M(\lambda^{-1}) = m_0 + m_1\lambda^{-1} + \ldots + m_n\lambda^{-n},$$

where $m_i, i = 1, \ldots, n$, are the coefficients. An immediate observation is that the frequency response of the left-hand side of (6.8) is real and non-negative at any frequency, which places certain restrictions on the scope of possible spatial impulse response shapes that we may investigate. However, as commented in 6.3.1, industrial experience shows that most actual actuator response shapes are able to satisfy or approximately satisfy this condition. The relationship between $\mathbf{G}_{ss}$ and $\mathbf{K}_{ss}$ from (6.4) affirms that if $\mathbf{G}_{ss}$ satisfies (6.8) then so does $\mathbf{K}_{ss}$.

After obtaining the causal FIR model $M(\lambda^{-1})$, the next step would be to find a parsimonious transfer function model (e.g., output-error model) to represent $M(\lambda^{-1})$. This process can be accomplished from the system identification toolbox in Matlab and the original noncausal $g(\lambda, \lambda^{-1})$ is approximated by $\bar{g}(\lambda, \lambda^{-1})$

as follows

$$\bar{g}(\lambda,\lambda^{-1}) = \frac{B(\lambda)B(\lambda^{-1})}{A(\lambda)A(\lambda^{-1})}, \tag{6.9}$$

$$B(\lambda^{-1}) = b_0 + b_1\lambda^{-1} + \ldots + b_{n_b}\lambda^{-n_b}, \tag{6.10}$$

$$A(\lambda^{-1}) = 1 + a_1\lambda^{-1} + \ldots + a_{n_a}\lambda^{-n_a}, \tag{6.11}$$

where n_a and n_b are the orders of $B(\lambda^{-1})$ and $A(\lambda^{-1})$, respectively. In a similar fashion, the noncausal transfer function form of the controller is assumed to be

$$\bar{k}(\lambda,\lambda^{-1}) = \frac{F(\lambda)F(\lambda^{-1})}{E(\lambda)E(\lambda^{-1})}, \tag{6.12}$$

$$F(\lambda^{-1}) = f_0 + f_1\lambda^{-1} + \ldots + f_{n_f}\lambda^{-n_f}, \tag{6.13}$$

$$E(\lambda^{-1}) = 1 + e_1\lambda^{-1} + \ldots + e_{n_e}\lambda^{-n_e}, \tag{6.14}$$

where n_e and n_f are the orders of $E(\lambda^{-1})$ and $F(\lambda^{-1})$, respectively. From (6.9)-(6.14), the original high-dimensional MIMO steady-state closed-loop model (6.5)-(6.6) can be replaced by scalar but noncausal transfer functions[5]

$$y(x) = \frac{\bar{g}}{1+\bar{g}\bar{k}}r(x) + \frac{1}{1+\bar{g}\bar{k}}v(x), \tag{6.15}$$

$$u(x) = \frac{1}{1+\bar{g}\bar{k}}r(x) - \frac{\bar{k}}{1+\bar{g}\bar{k}}v(x), \tag{6.16}$$

where x stands for the spatial coordinate. Note that the input and output sensitivity functions have the same noncausal transfer function representation as shown above.

6.3.2 Causal equivalent closed-loop models

The closed-loop scalar noncausal model of the CD process (6.15)-(6.16) is still not in a form convenient for traditional optimal input design algorithms. In this subsection we develop a method to find causal-equivalent models for the noncausal transfer functions such as $\bar{g}(\lambda,\lambda^{-1})$. First, the following Lemma is necessary.

Lemma 6.3.1. *Suppose that $\bar{g}_1(\lambda,\lambda^{-1})$ and $\bar{g}_2(\lambda,\lambda^{-1})$ satisfy the conditions in Assumption 6.3.1. Then the sum $\bar{g}_1(\lambda,\lambda^{-1}) + \bar{g}_2(\lambda,\lambda^{-1})$ also has a factorization as* (6.8)*.*

[5] In the sequel, we will omit the subscript and use the argument x to indicate the steady-state input and output sequence.

Proof. Since the conditions in Assumption 6.3.1 apply to polynomials $\bar{g}_1(\lambda,\lambda^{-1})$ and $\bar{g}_2(\lambda,\lambda^{-1})$, we have

$$\begin{aligned}\bar{g}_1(e^{j\omega},e^{-j\omega}) &\geq 0,\ \forall\omega,\\ \bar{g}_2(e^{j\omega},e^{-j\omega}) &\geq 0,\ \forall\omega,\end{aligned}$$

Thus it follows that

$$\bar{g}_1(e^{j\omega},e^{-j\omega})+\bar{g}_2(e^{j\omega},e^{-j\omega}) \geq 0,\ \forall\omega. \tag{6.17}$$

Besides, the coefficient sequence of (6.17) is real and symmetric. From the Fejér-Riesz Theorem there always exists an $M(\lambda)$ such that (6.8) is satisfied. ■

Defining $\bar{S}=\frac{1}{1+\bar{g}\bar{k}}$, from (6.15)-(6.16), we have

$$\bar{S}=\frac{A(\lambda)A(\lambda^{-1})E(\lambda)E(\lambda^{-1})}{A(\lambda)A(\lambda^{-1})E(\lambda)E(\lambda^{-1})+B(\lambda)B(\lambda^{-1})F(\lambda)F(\lambda^{-1})}. \tag{6.18}$$

From Lemma 6.3.1, it follows that the denominator of (6.18) can be factorized to be the product of a causal FIR filter and its anti-causal form. Therefore, the closed-loop transfer functions (6.15)-(6.16) can be simplified as

$$y(x) = \bar{S}_1(\lambda,\lambda^{-1})r(x)+\bar{S}_2(\lambda,\lambda^{-1})v(x), \tag{6.19}$$

$$u(x) = \bar{S}_2(\lambda,\lambda^{-1})r(x)-\bar{S}_3(\lambda,\lambda^{-1})v(x), \tag{6.20}$$

where $\bar{S}_i(\lambda,\lambda^{-1}), i=1,2,3$, has a structure similar to that of (6.9) and (6.12). Further notice that ϕ can also be represented by a noncausal transfer function as is assumed in previous sections. In other words, the spatial noise $\mathbf{v}_{ss}$ has the following expression

$$v(x)=\bar{h}(\lambda,\lambda^{-1})e(x)=\frac{D(\lambda)D(\lambda^{-1})}{C(\lambda)C(\lambda^{-1})}e(x), \tag{6.21}$$

where $\{e(x)\}$ is a spatial white noise sequence. To find a causal-equivalent transfer function for (6.19)-(6.21), we establish the following theorem.

Theorem 6.3.1. *Consider a stochastic process with the output sequence* $\{y(x), x = 1, \ldots, m\}$ *generated according to the following noncausal Box-Jenkins model*

$$y(x) = \frac{M(\lambda)M(\lambda^{-1})}{N(\lambda)N(\lambda^{-1})} r(x) + \frac{R(\lambda)R(\lambda^{-1})}{S(\lambda)S(\lambda^{-1})} e(x), \tag{6.22}$$

where $\{e(x), x = 1, \ldots, m\}$ *is a Gaussian white noise sequence. The polynomials with arguments* λ^{-1} *and* λ *are the causal and anti-causal parts, respectively. Assume that all polynomials have no zeros on the unit circle and are minimum phase. Then there exist causal polynomials* $\tilde{M}_y(\lambda^{-1})$, $\tilde{N}_y(\lambda^{-1})$, $\tilde{R}_y(\lambda^{-1})$, $\tilde{S}_y(\lambda^{-1})$ *and a white noise sequence* $\{\tilde{e}_y(x)\}$ *as well as a stochastic sequence* $\{\tilde{y}(x)\}$ *which has the same spectra as* $\{y(x)\}$ *such that,*

$$\tilde{y}(x) = \frac{\tilde{M}_y(\lambda^{-1})}{\tilde{N}_y(\lambda^{-1})} r(x) + \frac{\tilde{R}_y(\lambda^{-1})}{\tilde{S}_y(\lambda^{-1})} \tilde{e}_y(x). \tag{6.23}$$

Proof. Multiplying both sides of (6.22) by using $N(\lambda)N(\lambda^{-1})S(\lambda)S(\lambda^{-1})$, we obtain

$$\begin{aligned} N(\lambda)N(\lambda^{-1})S(\lambda^{-1})S(\lambda)y(x) = M(\lambda)M(\lambda^{-1})S(\lambda) \\ S(\lambda^{-1})r(x) + N(\lambda)N(\lambda^{-1})R(\lambda)R(\lambda^{-1})e(x). \end{aligned} \tag{6.24}$$

Define the roots of causal polynomials $M(\lambda^{-1})$, $N(\lambda^{-1})$, $R(\lambda^{-1})$, $S(\lambda^{-1})$ to be, respectively, α_i, β_i, γ_i and δ_i. Let

$$\pi_M = \prod_i \frac{\lambda^{-1} - \alpha_i}{\lambda - \alpha_i},\ \pi_N = \prod_i \frac{\lambda^{-1} - \beta_i}{\lambda - \beta_i},\ \pi_R = \prod_i \frac{\lambda^{-1} - \gamma_i}{\lambda - \gamma_i},\ \pi_S = \prod_i \frac{\lambda^{-1} - \delta_i}{\lambda - \delta_i}.$$

Notice that $N(\lambda)N(\lambda^{-1})\pi_N = N^2(\lambda^{-1})$ and the same also holds for $M(\lambda)$, $R(\lambda)$, and $S(\lambda)$. Multiplying both sides of (6.24) by $\pi_M\pi_S$, after some manipulations, we have

$$N^2(\lambda^{-1})S^2(\lambda^{-1})\tilde{y}(x) = M^2(\lambda^{-1})S^2(\lambda^{-1})r(x) + R^2(\lambda^{-1})\tilde{e}_y(x), \tag{6.25}$$

where $\tilde{y}(x) = \frac{\pi_M}{\pi_N} y(x)$, $\tilde{e}_y(x) = \frac{\pi_M\pi_S}{\pi_N\pi_R} e(x)$. Since π_M, π_N, π_R and π_S are all-pass filters, $\{\tilde{e}_y(x)\}$ is a Gaussian white noise sequence with the same spectra as $\{e(x)\}$ but may correspond to different realizations. Besides, $\{\tilde{y}(x)\}$ has the same spectra as $\{y(x)\}$. Therefore, (6.23) is verified by pairing $\tilde{M}(\lambda^{-1}) = M^2(\lambda^{-1})$ and so on with (6.25). ■

Remark 6.3.2. From Theorem 6.3.1 one may interpret the equivalence between $\{\tilde{y}(x)\}$ and $\{y(x)\}$ in terms

of the spectra, although realizations might be different. However, this equivalence greatly facilitates the maximum likelihood estimation for the original noncausal model by reducing it into a causal-equivalent form. The rationale for performing identification in this manner has been explained in [82] for an ARX model. The conclusion is that the log-likelihood function of the noncausal model converges to that of the causal model with probability one as the sample number tends to infinity. This result can also be extended to the noncausal Box-Jenkins model in (6.22).

Similarly, the input signal $u(x)$ in (6.20) can also be represented through causal filters

$$\tilde{u}(x) = \frac{\tilde{M}_u(\lambda^{-1})}{\tilde{N}_u(\lambda^{-1})} r(x) + \frac{\tilde{R}_u(\lambda^{-1})}{\tilde{S}_u(\lambda^{-1})} \tilde{e}_u(x), \tag{6.26}$$

where $\{\tilde{u}(x)\}$ and $\{u(x)\}$ have the same spectra. The equations (6.23) and (6.26) are necessary for the optimal input design in the sequel.

6.3.3 Covariance matrix equivalence of the causal and noncausal model parameter estimates

It is well-known that if the white noise is Gaussian distributed, the prediction error method with properly chosen criterion coincides with the maximum likelihood estimation. In [82], it is shown that the log-likelihood function of the noncausal ARX model and that of the corresponding causal ARX model converge to the same value as the sample number tends to infinity. In this subsection we will demonstrate a similar statement for Box-Jenkins models with closed-loop data.

Theorem 6.3.2. *Consider the following noncausal process model (θ is the parameter in a compact set Ω)*

$$y(x) = \bar{g}(\lambda, \lambda^{-1}, \theta) u(x) + \bar{h}(\lambda, \lambda^{-1}, \theta) e(x), \tag{6.27}$$

where $\bar{g}$ is defined in (6.9)-(6.11) *and $\bar{h}$ is defined in* (6.21). *$e(x)$ is Gaussian white noise. Suppose that the data is generated in closed-loop with controller* (6.12)-(6.14) *and that all relevant transfer functions are uniformly stable. Denote $\mathscr{L}_y^m(y)$ as the log-likelihood function of the noncausal model* (6.27) *and $\mathscr{L}_{\tilde{y}}^m(\tilde{y})$ as the log-likelihood function of the causal-equivalent model of* (6.27) *obtained similarly as* (6.23). *Then, as*

$m \to \infty$ (m is the spatial sample number, i.e., the number of measurement bins),

$$\sup_{\theta\in\Omega} |\mathscr{L}_y^m(y) - \mathscr{L}_{\tilde{y}}^m(\tilde{y})| \xrightarrow{w.p.1} 0, \tag{6.28}$$

$$\sup_{\theta\in\Omega} \left\| \frac{d\mathscr{L}_y^m(y)}{d\theta} - \frac{d\mathscr{L}_{\tilde{y}}^m(\tilde{y})}{d\theta} \right\| \xrightarrow{w.p.1} 0. \tag{6.29}$$

Proof. The proof of (6.28) follows along Proposition 3 in [82] and the proof for (6.29). ■

We outline the proof for (6.29) in Theorem 6.3.2. First the following lemma is necessary.

Lemma 6.3.2. *Consider a set of uniformly stable causal or noncausal filters $G(\lambda,\theta), \theta \in \Omega$, and $H(\lambda,\theta), \theta \in \Omega$. Define $u(x),\ x = 1,\ldots,m$, as a bounded signal sequence, and $e(x),\ x = 1,\ldots,m$, as a sequence of Gaussian white noise with zero mean and variance σ^2. The signal $s(x),\ x = 1,\ldots,m$, is generated via*

$$s_\theta(x) = G(\lambda,\theta)u(x) + H(\lambda,\theta)e(x). \tag{6.30}$$

Then as $m \to \infty$, the sample variance of $s_x(\theta)$ converges uniformly in probability to the ensemble variance

$$\sup_{\theta\in\Omega} \left\| \frac{1}{m}\sum_{x=1}^{m} s_\theta(x)s_\theta^T(x) - \frac{1}{m}\sum_{x=1}^{m} \mathbb{E}s_\theta(x)s_\theta^T(x) \right\| \to 0, w.p.1. \tag{6.31}$$

Note that (6.31) is an extension of Theorem 2B.1 in [15] to noncausal models. The proof follows a similar line and is thus omitted here. Based on Lemma 6.3.2, as $m \to \infty$, the following statements hold

- $\frac{d\mathscr{L}_y^m(y,\theta)}{d\theta}$ converges uniformly w.r.t. θ in probability;
- $\frac{d\mathscr{L}_{\tilde{y}}^m(\tilde{y},\theta)}{d\theta}$ converges uniformly w.r.t. θ in probability.

The reason is that both $\frac{d\mathscr{L}_y^m(y)}{d\theta}$ and $\frac{\mathscr{L}_{\tilde{y}}^m(\tilde{y},\theta)}{d\theta}$ can similarly be considered as generated from uniformly stable filters. Thus from Lemma 6.3.2 the above statements hold. On the other hand, from the proof of (6.28) in [82], one can see that both $\mathscr{L}_y^m(y)$ and $\mathscr{L}_{\tilde{y}}^m(\tilde{y},\theta)$ converge uniformly to the same value, denoted as $\sigma^2(\theta)$. Based on Theorem 7.17 in [119], with the above statements, we have, as $m \to \infty$,

$$\sup_{\theta\in\Omega} \left\| \frac{d\mathscr{L}_y^m(y,\theta)}{d\theta} - \frac{d\sigma^2(\theta)}{d\theta} \right\| \to 0, \text{ w.p.1}, \tag{6.32}$$

$$\sup_{\theta\in\Omega} \left\| \frac{d\mathscr{L}_{\tilde{y}}^m(\tilde{y},\theta)}{d\theta} - \frac{d\sigma^2(\theta)}{d\theta} \right\| \to 0, \text{ w.p.1}. \tag{6.33}$$

From the Triangle Inequality, the result (6.29) follows. It should be pointed out that in this proof the 'uniformity' of the convergence in probability is a necessary condition for the results to hold.

Remark 6.3.3. Theorem 6.3.2 implies that both the log-likelihood function and its derivative with respect parameter θ obtained from the noncausal and causal-equivalent models are identical asymptotically. Therefore, we can conclude that the parameter covariances from these two schemes coincide, and hence we may perform the optimal input design based solely on the causal-equivalent model.

6.4 Closed-loop optimal input design

In this section closed-loop optimal input design for the steady-state CD process is investigated. As mentioned above we can accomplish this task with the causal-equivalent representation of CD process. Note that in practice the noise model parameters are of less interest and thus we split the parameter θ as $\theta = [\rho^T \ \eta^T]^T$, where ρ is the process model parameter and η is the noise model parameter. For optimal input design our objective is to minimize the covariance of ρ by selecting the optimal excitation signal. From Theorem 6.3.2 the parameter covariance of ρ, P_ρ, is expressed as

$$P_\rho \sim \frac{1}{m}\left[\frac{1}{2\pi\lambda_0}\int_{-\pi}^{\pi}\frac{1}{|\tilde{h}(e^{j\omega},\eta_0)|^2}\frac{\partial\tilde{g}(e^{j\omega},\rho_0)}{\partial\rho}\ \Phi_{\tilde{u}}(\omega)\frac{\partial\tilde{g}^T(e^{-j\omega},\rho_0)}{\partial\rho}d\omega\right]^{-1}, \tag{6.34}$$

where λ_0 is the variance of noise $\tilde{e}_y(x)$. $\tilde{g}$ and $\tilde{h}$ are the causal equivalent forms of $\bar{g}$ and $\bar{h}$, respectively. The input spectrum $\Phi_{\tilde{u}}(\omega)$, according to (6.26), is related to the excitation spectrum $\Phi_r(\omega)$ via

$$\Phi_{\tilde{u}}(\omega) = \left|\frac{\tilde{M}_u(e^{-j\omega})}{\tilde{N}_u(e^{-j\omega})}\right|^2\Phi_r(\omega) + \left|\frac{\tilde{R}_u(e^{-j\omega})}{\tilde{S}_u(e^{-j\omega})}\right|^2\lambda_0. \tag{6.35}$$

The closed-loop optimal input design can be formulated as minimizing a function of the parameter covariance P_ρ subject to a set of constraints, e.g., input and output power constraints,

$$\min_{\Phi_r(\omega)} \quad f_0(P_\rho(\Phi_r(\omega))) \tag{6.36}$$

$$s.t. \quad \frac{1}{2\pi}\int_{-\pi}^{\pi}\Phi_u(\omega)d\omega \le c_u, \tag{6.37}$$

$$\frac{1}{2\pi}\int_{-\pi}^{\pi}\Phi_y(\omega)d\omega \le c_y, \tag{6.38}$$

where c_u and c_y are the power limits on input and output signals. The constraints (6.37)-(6.38) can be written in terms of the design variable $\Phi_r(\omega)$ by (6.35) and (6.23), respectively. As this optimization problem is still infinite-dimensional (since $\Phi_r(\omega)$ is a continuous function of ω), a technique known as finite dimensional parameterization [62] can be employed to reduce it into finite-dimensional. Specifically, $\Phi_r(\omega)$ can be parameterized by the definition of a spectrum

$$\Phi_r(\omega) = \sum_{k=-m_c}^{m_c} c_k e^{-j\omega k} \geq 0, \ \ \forall \omega, \tag{6.39}$$

where $c_k,\ k = -m_c, \ldots, m_c$, are the parameters, and m_c is the selected number of parameters. With (6.39) the original optimization problem can be cast into one with finite number of parameters. Note that the non-negativity constraint on the parameterized spectrum (6.39) at any frequency has to be satisfied while searching for the optimal c_k. This requirement can be fulfilled by using the KYP lemma and constructing a controllable and observable state-space realization for the spectrum [62]. After these modifications the resulting optimization problem is convex (choose $f_0(\cdot)$ to be a convex function, such as the trace of inverse function, negative log determinant function and negative maximum eigenvalue function) and can be readily solved by off-the-shelf solvers such as the CVX toolbox. In Example 6.5 below, we choose the negative log determinant function as $f_0(\cdot)$.

Remark 6.4.1. Note that the aforementioned optimal input design only considers the power constraints on the input and output (6.37)-(6.38). However, in practice, the hard constraints on CVs and MVs make more sense and this is still an open problem for frequency-domain optimal input design. Besides, specific to the CD process, the second-order bending constraints preventing 'picketing' on actuators are also important. These practical constraints are beyond the scope of this paper and will be investigated in future work.

Remark 6.4.2. A common issue for optimal input design is that the covariance matrix depends on the true parameter values, as shown in (6.34), which may not be accessible in practice. One remedy is the adaptive input design scheme: specifying an initial parameter value to design an optimal input signal, updating parameter estimates via identifications and using the updated parameter value to design a new optimal input. This process is performed iteratively until it converges.

Remark 6.4.3. The optimal input design approach proposed above is only meant for the CD steady-state model. In fact, the practically implemented input design for CD identification is two-dimensional involving both spatial and temporal variations. For the design of optimal input in the temporal direction, the mature

techniques developed in recent years for traditional dynamic systems can be applied directly. In this work, for simplicity, in the next chapter for integrated simulations, we use temporal PRBS signal as the time-domain variations and spatial optimal signal obtained above to composite the actual CD excitation signal.

6.5 Example

In this section we use a simulation example to validate the proposed CD process modeling and closed-loop optimal input design methods. In particular, we would compare the effect of optimally designed input on parameter estimates with that of bump excitation signal that is currently employed in the industry [72].

In practice, the spatial response shape of a single actuator is assumed to satisfy the nonlinear equation in (1.2) with four spatial parameters [12]. In this example, these parameters are specified with values, respectively, $\gamma = 0.3802$, $\xi = 268.6414$, $\beta = 0.10$, $\alpha = 3.5$. The response shape under impulse signal of amplitude 5 is illustrated as the red curve (upper plot) in Fig. 6.2. For convenience we assume that the CD process has 222 actuators and measurement bins. The controller is chosen to be CD-MPC with prediction horizon 25 samples and control horizon 5 samples (sampling interval is 12 seconds). The weighting matrices in the cost function is selected to be $Q_1 = 0.4I$ and $Q_3 = 0.1667I$. The parameter α_K in (6.4) is computed to be 12.3212. From Section 6.3 one is able to obtain noncausal scalar models for the CD process and the controller, respectively. The impulse response curves of these noncausal models are shown in Fig. 6.2 in the blue dash-dotted curves. Note that for simplicity we have chosen $n_b = n_f = 1$, $n_a = n_e = 2$. Higher order models improve the quality of estimates but also increase the computational cost in designing the optimal input. The noise variance is chosen to be 0.1 with noise model $\phi = I$ (output-error structure). Fig. 6.3 shows the optimal spectrum based on causal-equivalent models with $c_u = 50$. Notice that small process gain (the causal-equivalent model has even smaller gain) as in this case requires a large excitation signal to achieve a good signal-to-noise ratio.

To make a fair comparison between the optimal and bump excitations, we set a hard constraint ± 10 on the amplitude of excitation signals. For the optimally designed input, if any part of its amplitude violates this constraint, we set that part at the corresponding bound. For the bumped signal, the amplitudes of bumps alternate between -10 and 10. In order to further show the optimality of designed input, we generate another excitation signal that is a white noise sequence with the *same* variance as the optimal input. For each excitation signal we perform 100 Monte-Carlo simulations and a process model is identified in each

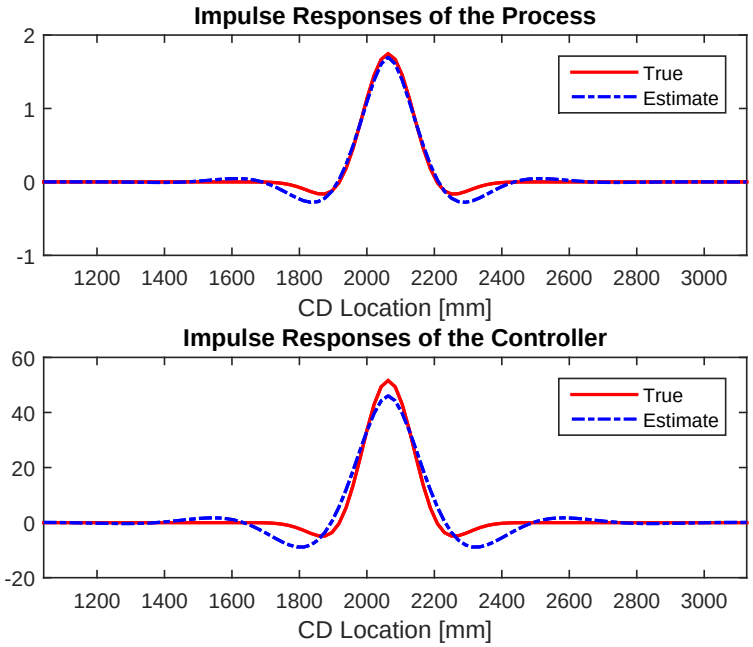

Figure 6.2: The impulse response of a single actuator (red solid line) and the impulse response of the estimated noncausal transfer function (blue dash-dotted line).

simulation. Fig. 6.4 shows the impulse responses of estimated models under these three excitation signals. It can been observed that estimates under the optimal input have the smallest variance while estimates under the bumped signal show the largest variance. Specifically, the averaged errors of estimated impulse responses relative to the true response are shown to be 0.0643, 1.3344 and 0.4479, respectively, for the optimal input, bumped input and white noise input. Thus we can conclude that our optimal input outperforms the bump excitation signal and white noise signal (with the same variance) in terms of the identification performance.

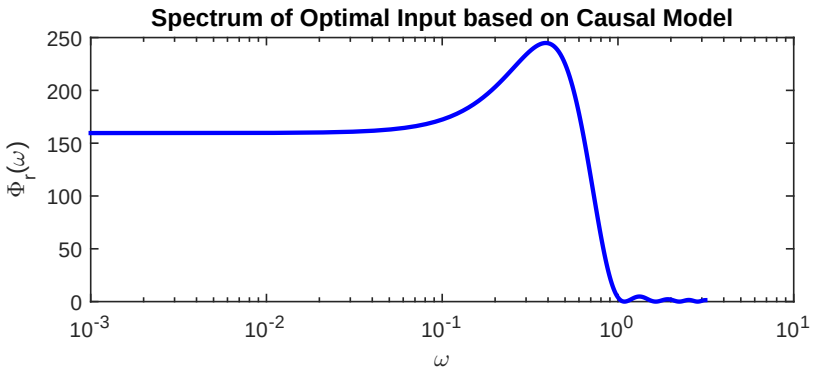

Figure 6.3: Spectrum of the optimal input based on causal-equivalent model of the CD process.

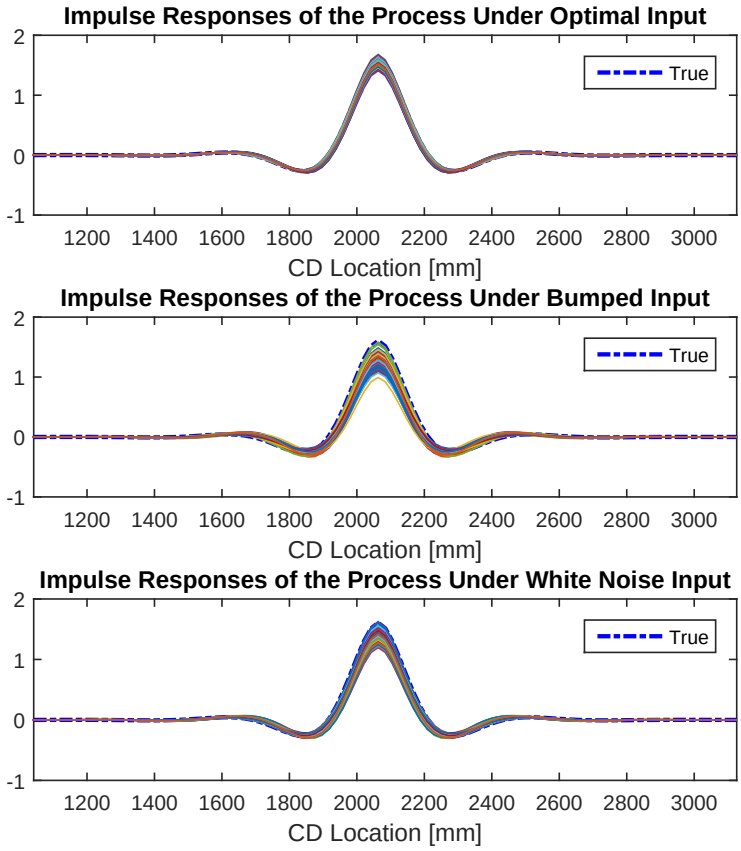

Figure 6.4: The impulse responses of the estimated process model in the closed-loop under the optimally designed input (upper plot), the bumped input (middle plot), and the white noise input (bottom plot) in 100 Monte-Carlo simulations.

6.6 Summary

We developed an approach to represent the closed-loop steady-state CD process model with noncausal scalar transfer functions. The advantage of using noncausal models is that it circumvents the problem of large dimensions associated with MIMO representations of CD processes. We then show that these noncausal transfer functions can be further represented by spectrally equivalent causal transfer functions. A closed-loop optimal input design framework is proposed based on these causal-equivalent models. An example is provided to validate the proposed approaches and demonstrate the advantage of optimal input in system identification performance over the industrial practice of using bump excitation as well as white noise excitation.

Chapter 7

CD Iterative Identification and Control

In this section we integrate controller performance assessment, model-plant mismatch detection, optimal input design and closed-loop identification together. The controller performance assessment and mismatch detection combine as the monitoring block and users can make overall decisions by observing the respective detection results. Notice that not all model-plant mismatches can significantly degrade the controller performance and also that the controller performance assessment technique is only applicable to steady-state data. In other words, the performance index from the controller performance assessment may not give much information about the transient performance. Therefore, our strategy is to use the diagnosis results from the MPM detection as the main factor in considering whether we inject closed-loop excitations. The controller performance assessment results serve as a side metric on how good the controller is performing at steady-state. The users can modify this strategy based on their own preference or demand.

The process in this example is a single-array CD process with dry weight as the measured profile and autoslice as the actuators. There are 222 measurement bins in the cross direction and 74 actuator zones. Parameters selected in this simulation example are shown in Table 7.1.

Table 7.1: Summary of parameters setup in adaptive control simulation

Parameters	Values	Parameters	Values
Moving window size	40 min	Actuator zone width	62.5194 mm
Window step size	5 min	Measurement bin width	20.8398 mm
Sampling interval	12 seconds	# of measurement bins	222
Training stage duration	4.17 hours	# of actuator zones	74
Identification duration	1.67 hours	Nominal spatial parameters	[0.38 268 0.1 1.5]
MPM inspection interval	1 hour	Nominal temporal parameters	[126 35.98]
Mismatch threshold	0.8	Spatial alpha ratio	$1.3 \sim 4$
# of ID iterations	10	Temporal alpha ratio	3

Note that the MPM inspection interval determines how many of last few SVM scores are used to discover the existence of mismatch. If the percentage of negative SVM scores is greater than the mismatch threshold,

then we would raise a mismatch alarm. The parameter spatial/temporal alpha ratio shows the extent to which we would like to enlarge the initial cluster of process model estimates from the training data. At the beginning of simulation we choose the initial parameters as $\theta_C^i = [0.3\ 200\ 0.2\ 4.0]^T$, $\theta_T^i = [60\ 2]^T$. In the case with mismatch and subsequent closed-loop identification we will update the initial values after identification into those obtained from the identification stage. Note also that our simulation is based on the assumption that the output noise is white. However, the underlying idea can be extended to the case where process output is affected by colored noise (cf. Section 5.3).

7.1 Case I: No model-plant mismatch

In this case study we examine our controller performance assessment, mismatch detection and closed-loop identification algorithms when there is no discrepancy between the true plant and plant model used by CD MPC. Initially there is a steady-state disturbance acting on the CD output profile and it is rapidly attenuated by the CD controller. We apply the whole adaptive control algorithm since the beginning of the simulation, however, the first few parameter estimates are discarded since they may not be reliable due to the non-stationary transient behavior during the rejection of steady-state disturbance. This logic is performed similarly for the following case studies when there exist model-plant mismatches. Fig. 7.1 demonstrates the sampled output and input data during the normal operation free of mismatches. Obviously the system enters into a steady-state mode after the initial transient part in compensating for the steady-state disturbance and there is no significant increase in the variations of output and input at steady-state. Fig. 7.2 displays the explicit parameter estimates at each moving windows, for both spatial and temporal models, from which we do not observe apparent trend of a parameter drifting away from the true parameter (shown in red dash-dotted line). There are some biases in several parameter estimates such as the gain and time constant and they come from the ridge regularization in the high-order ARX modeling step of iterative identifications. However, as remarked above regarding our mismatch detection method, the changes in parameter estimates are of importance rather than the accuracy of these parameter estimates relative to the true values. The adaptive control simulation results are illustrated in Fig. 7.3. One can see that the user-specified benchmark stays close to one all the time, and SVM scores for both spatial and temporal models are positive most of the time which implies that there is no mismatch existing in the profiles. The 2σ values for output and input are almost flat at a level after initial drops due to the rejection of steady-state disturbance.

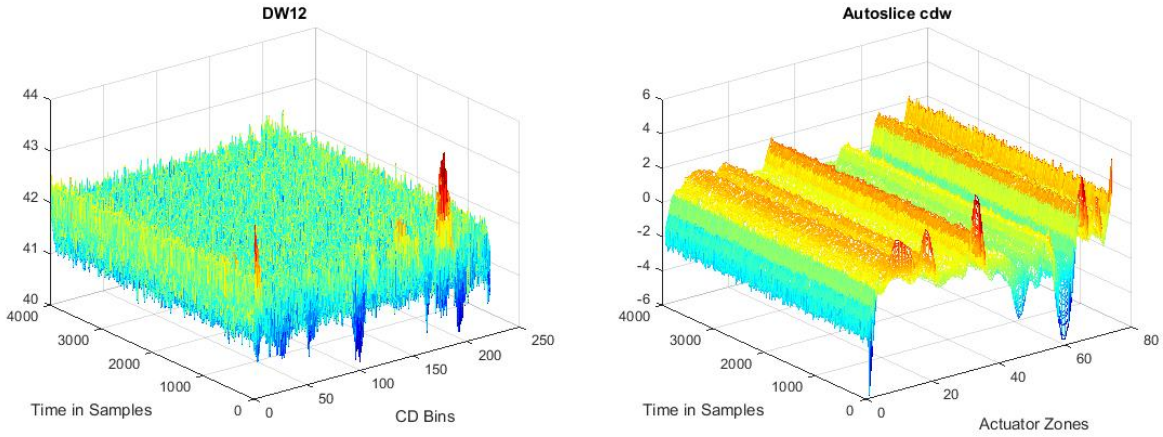

Figure 7.1: No mismatch: The collected output and input profiles

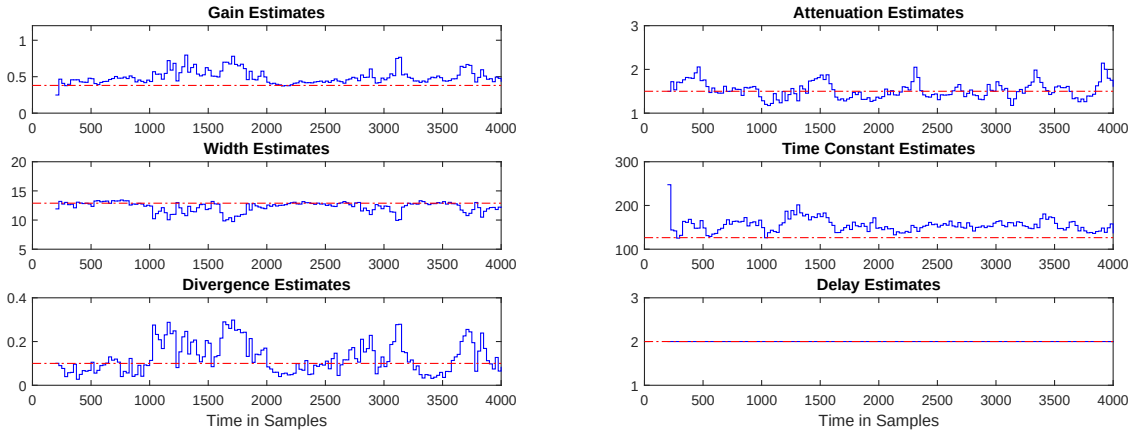

Figure 7.2: No mismatch: Estimates of parameters in each moving window

7.2 Case II: Gain mismatch

In this case study we concentrate on the effects of gain model-plant mismatch. For such purpose we let the simulator run for a while without any mismatch and then we manually introduce a gain mismatch to the simulation after 2000 samples. To be specific, initially both true plant gain and model gain are set to be equal, i.e., $\gamma_p = \gamma_m$, where γ_p is the gain of true plant, and $\gamma_m = 0.38$ is the process model gain. After obtaining 2000 samples (approximately 6.67 hours) of input-output data we create a model-plant mismatch by altering the true plant gain to $\gamma_p = 2\gamma_m$ gradually while keeping the model gain unchanged. The gathered input-output data and parameter estimates from moving windows are shown in Fig. 7.4 and Fig. 7.5, respectively. From the input-output profile plot we can see that the mismatch detection algorithm successfully finds the mismatch shortly after we introduce the mismatch. The identification experiment starts with injecting

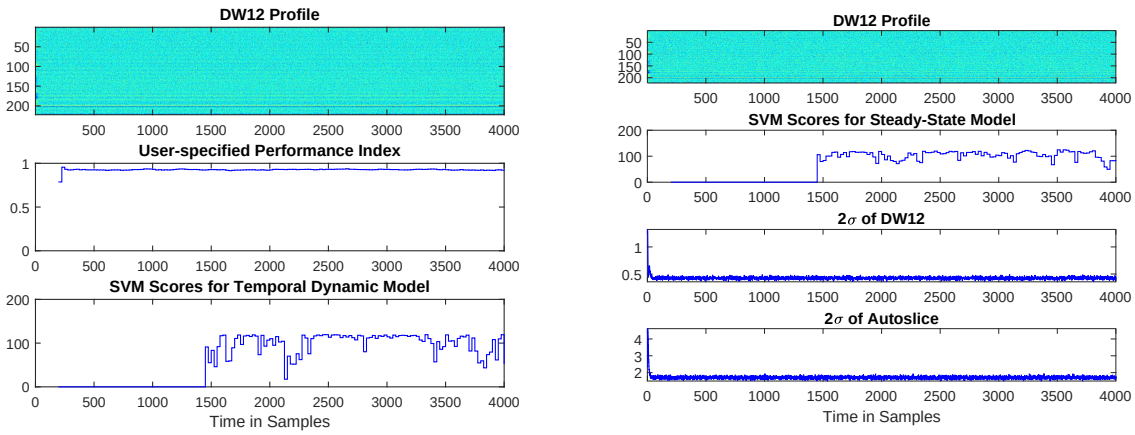

Figure 7.3: No mismatch: Adaptive CD MPC control results

excitation signals into the system and ends with identifying a new process model. The mismatch is more clearly shown in the gain parameter estimates plot Fig. 7.5 in which gain estimates move up to a new level after we create the mismatch. Fig. 7.6 presents some key metrics over the entire adaptive control simulation. One can find that the user-specified benchmark starts to drop after the mismatch takes place until the moving window does not cover non-stationary data after the closed-loop identification. Note that if a moving window contains portions of data from both excitation and routine operation periods, then one expects that the performance index is low since stationary data is required for the performance assessment algorithm to perform well. However, the closed-loop identification is still applicable as long as the data meets the requirements of quasi stationarity. After the mismatch is introduced both temporal and spatial SVMs return negative scores showing the possibility of mismatch. In fact, we obtain a series of negative scores especially from the spatial SVM reports and the percentage of negative scores in the last one hour of moving windows exceeds the threshold. Therefore, a decision is made stating that a mismatch indeed occurs and we then trigger an identification experiment. Note that after the identification experiment we collect an extra portion of routine operation data in order to resume a new SVM training. The updated process model is acquired by averaging the parameter estimates over the moving windows within the identification stage and is then deployed to the CD MPC (termed as controller retuning). We can compare the 2σ of input and output before identification experiment and after controller retuning to find the improvement of control performance of using updated CD controller.

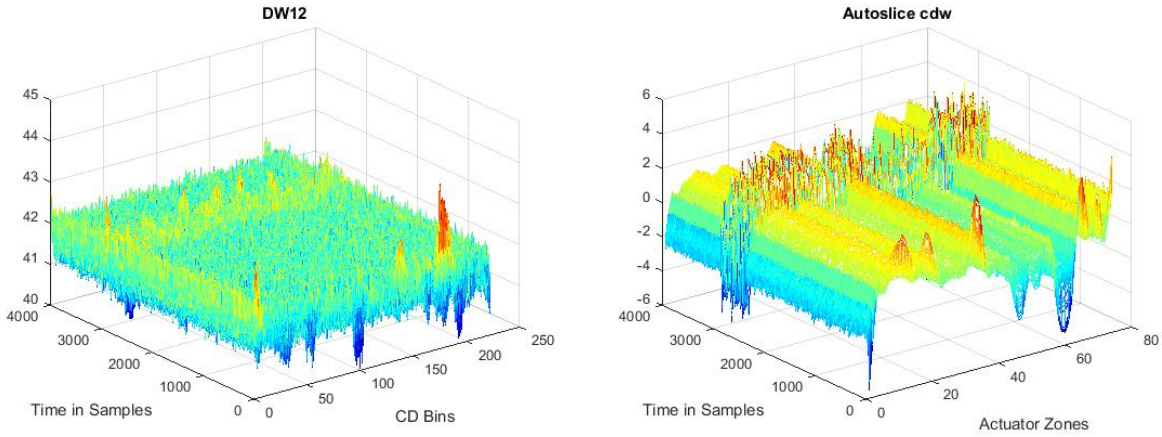

Figure 7.4: Gain mismatch: simulated output and input profile

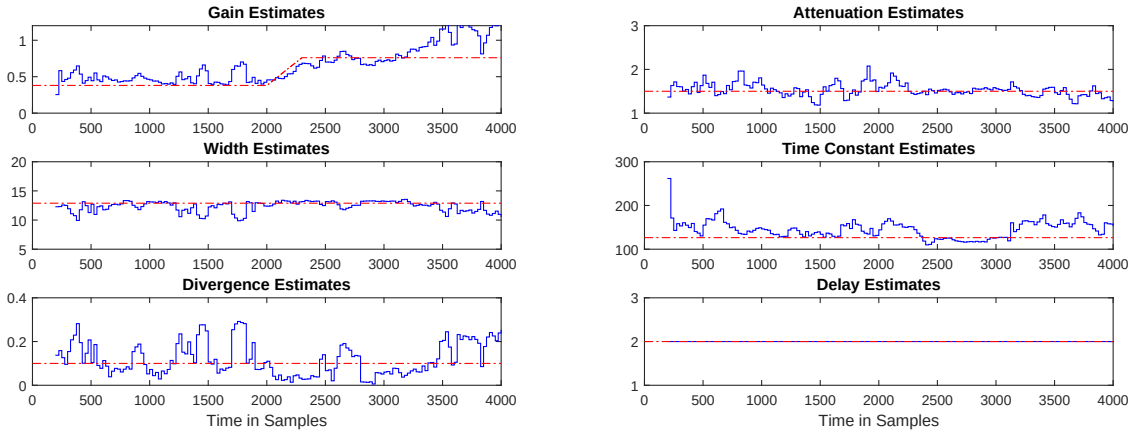

Figure 7.5: Gain mismatch: Estimates of parameters in each moving window

7.3 Case III: Width, divergence, and attenuation mismatches

Similar to the gain mismatch case, in this subsection we study the influences of the other three parametric mismatches on CD MPC performance. For the width mismatch we set $\xi_p = 1.3\xi_m$ after 2000 samples and remain ξ_m unchanged. The input-output data under this scenario is demonstrated in Fig. 7.7. Clearly these plots show the same pattern as the gain mismatch case, i.e., the adaptive control scheme consists of five stages: monitoring, mismatch detected, closed-loop identification, controller retuning and monitoring again at a new operation condition. The parameter estimates and adaptive control simulation results are shown in Fig. 7.8 and Fig. 7.9, respectively. For the divergence mismatch, we set $\beta_p = 3\beta_m$ after 2000 sample. The input-output data, parameter estimation results and adaptive control metrics are shown in Fig. 7.10, Fig. 7.11 and Fig. 7.12, respectively. Again, for the scenario of attenuation mismatch, we change $\alpha_p = 0.2\alpha_m$. Note

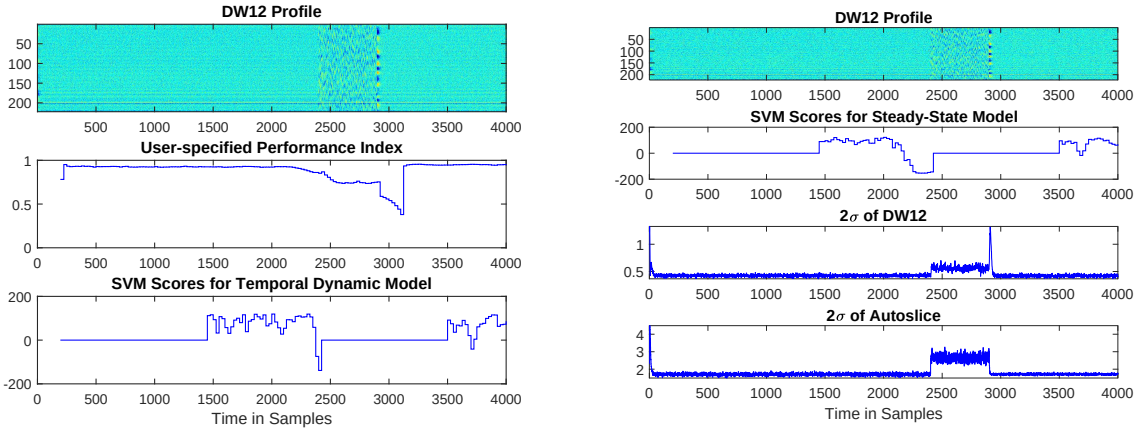

Figure 7.6: Gain mismatch: Adaptive CD MPC control results

that the effect of attenuation parameter is not significant in producing CD MPM, and thus we create a large mismatch here for an illustrative purpose. The corresponding simulation results are shown in Fig. 7.13, Fig. 7.14 and Fig. 7.15, respectively. In summary, for these three scenarios, our adaptive control algorithm is able to detect the mismatch even with routine operating data. Closed-loop excitation signals are injected into the system once the mismatch is observed. Careful examination of parameter estimates reveals that during the identification stage parameters can be accurately identified due to the high-quality excitation signal. We average the parameters within that period to attain a relatively reliable estimate of the true parameter and deploy it to the CD controller. Most of the time the input and output variations are reduced after retuning which implies a better control performance.

7.4 Case IV: Time constant mismatch

In the last case study we focus on the temporal parametric mismatch, i.e., time constant mismatch. Throughout the entire study we assume that the time delay is known *a priori* and is specified to the identification algorithm. The true time constant of plant remains unchanged in the first 2000 samples. After that we increase it to two times of the true parameter value but remain the time constant of process model unchanged. Fig. 7.16, Fig. 7.17 and Fig. 7.18 demonstrate the corresponding simulation results. Analogous to other simulations above we can see here that the mismatch detection algorithm is able to detect the mismatch and then correct it afterwards. Increase in the performance index and reduction of input and output variance show that the re-tuned control can improve the control performance.

7.5 Discussion of the simulation results

From the case studies above, one can see that for the normal case, both user-specified benchmark and SVM MPM detection method give consistent indications of good control performance without any false alarms on MPM. For the gain mismatch case, as the mismatch is significant, user-specified benchmark manages to detect the deterioration in control performance. Correspondingly, the MPM detection method also finds the changes in the process gain. Both indications suggest the triggering of an identification experiment, during which the output shows large fluctuations. Thus closed-loop identification is destructive to the continuous operation but fortunately, with our adaptive control scheme, the operator do not need to intentionally initiate a batch identification but rather just introduce the dither signal. With this method, we can thus avoid the cost on performing batch identification experiment. After ru-tuning the controller, the control performance recovers to an excellent level. For the other three spatial mismatches, one can see that the SVM MPM detection approach is rather sensitive to mismatches, while the performance index is not affected evidently. This suggests that despite of the presence of these mismatches, the inherent robustness of CD MPC can handle them to a great extent and thus the control performance is still satisfactory. For illustrative purposes, in our examples, we let these mismatches trigger the subsequent identifications. However, in practice, as the control performance is still high, it is not necessary to start the identification experiment under such scenarios. These examples imply that a combination of performance index and MPM detection results is more advisable in practice. For the last case study on time constant mismatch, notice that we intentionally introduce a large mismatch, and the control performance index still remains high. This coincides with the observations in the literature than the impact of time constant mismatch on control performance is much less compared with the impacts of other mismatches. A plausible explanation on this is that the performance index is proposed based on steady-state operating data where the effect of time constant on control performance is not significant.

7.6 Summary

This chapter presents several examples from CD and MD paper machine simulators to demonstrate the adaptive control framework. It is observed that the proposed control performance assessment and MPM detection approaches are applicable to routine operating data. Specifically, the user-specified performance index can detect significant mismatches while the SVM technique is sensitive to parametric mismatches. Therefore, a combination of these two techniques are recommended to raise alarms and trigger the subsequent closed-

loop identification experiment. In addition, it is shown that the proposed closed-loop identification can be continuously applied to both routine operating stage and experimental stage. The control performance can be recovered after re-tuning the MPC based on updated process models.

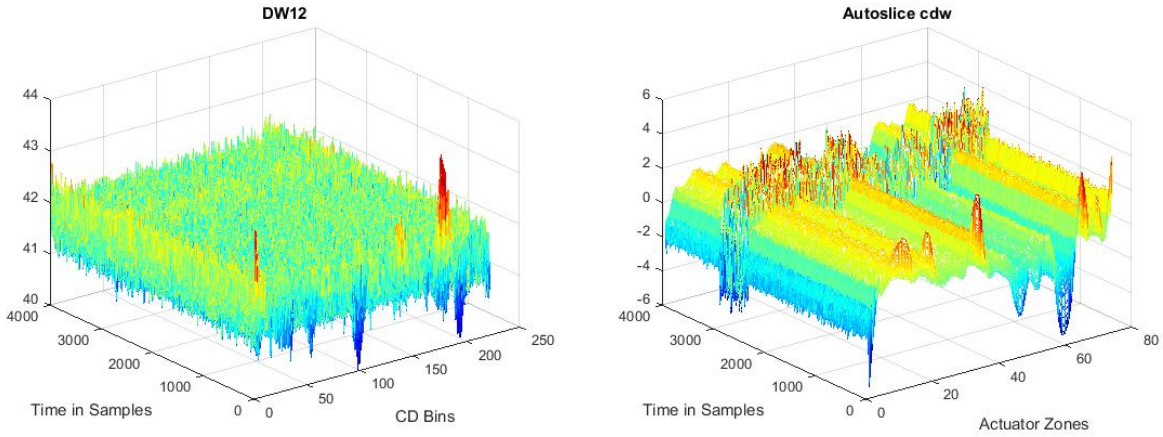

Figure 7.7: Width mismatch: The collected output and input profiles

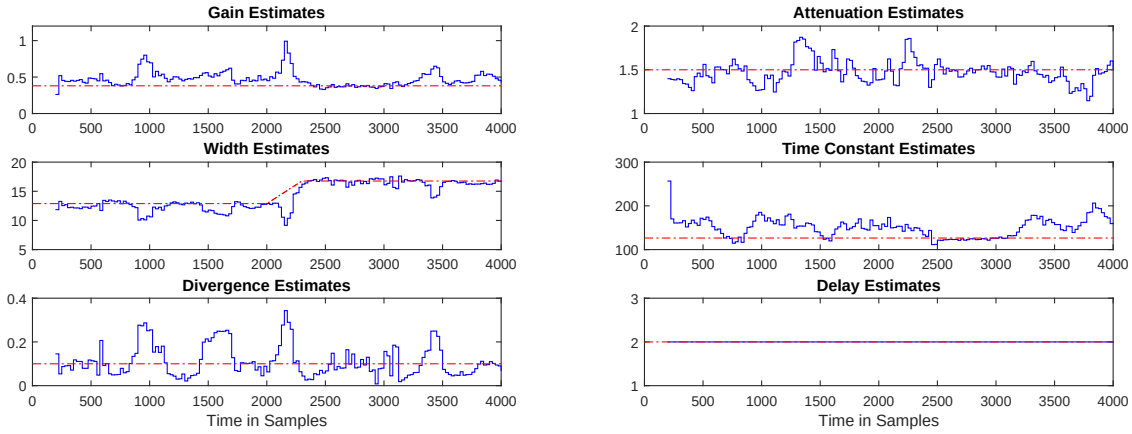

Figure 7.8: Width mismatch: Estimates of parameters in each moving window

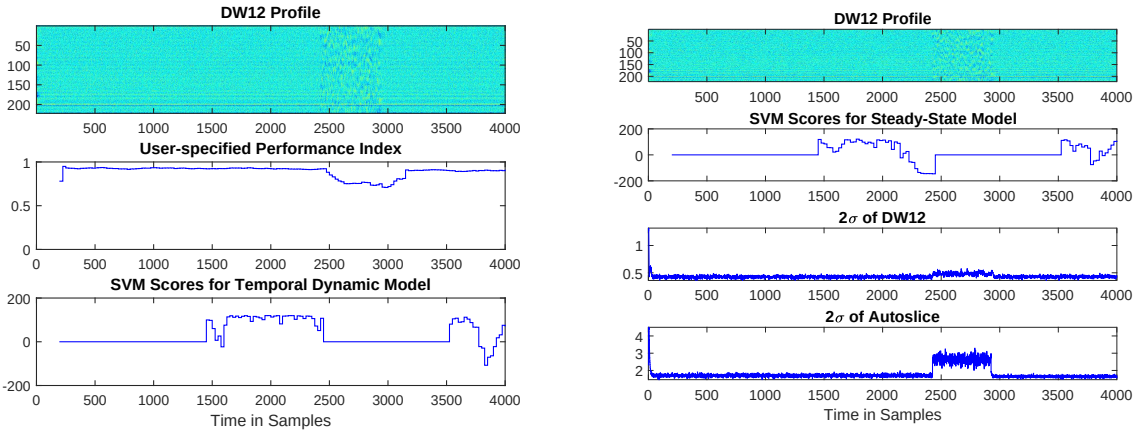

Figure 7.9: Width mismatch: Adaptive CD MPC control results

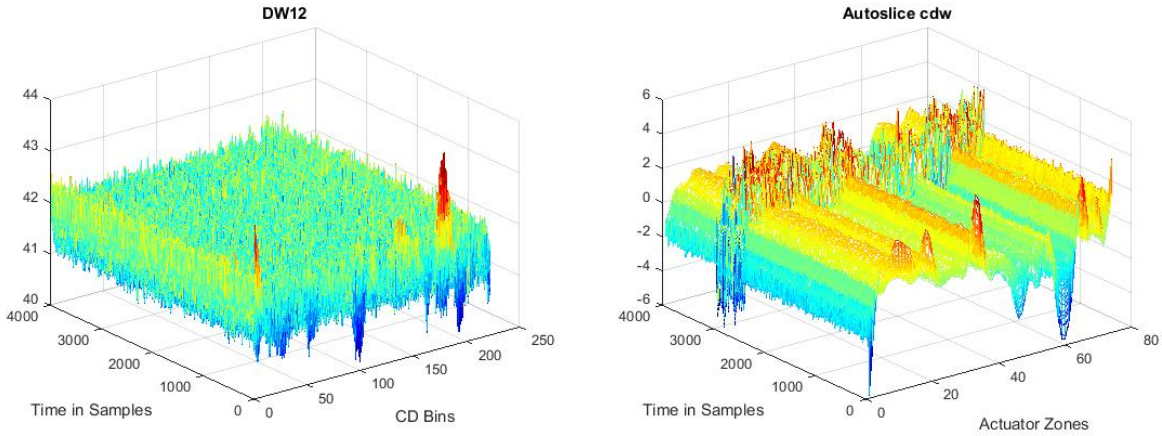

Figure 7.10: Divergence mismatch: The collected output and input profiles

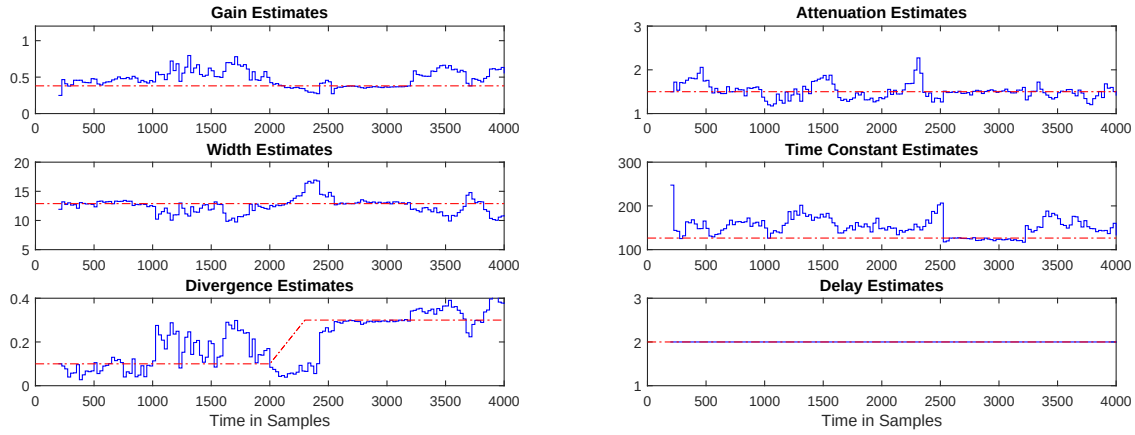

Figure 7.11: Divergence mismatch: Estimates of parameters in each moving window

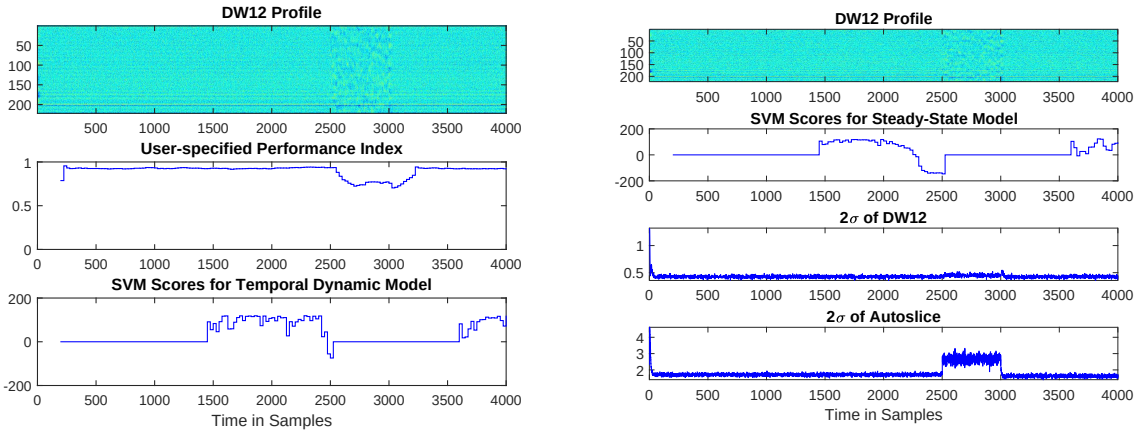

Figure 7.12: Divergence mismatch: Adaptive CD MPC control results

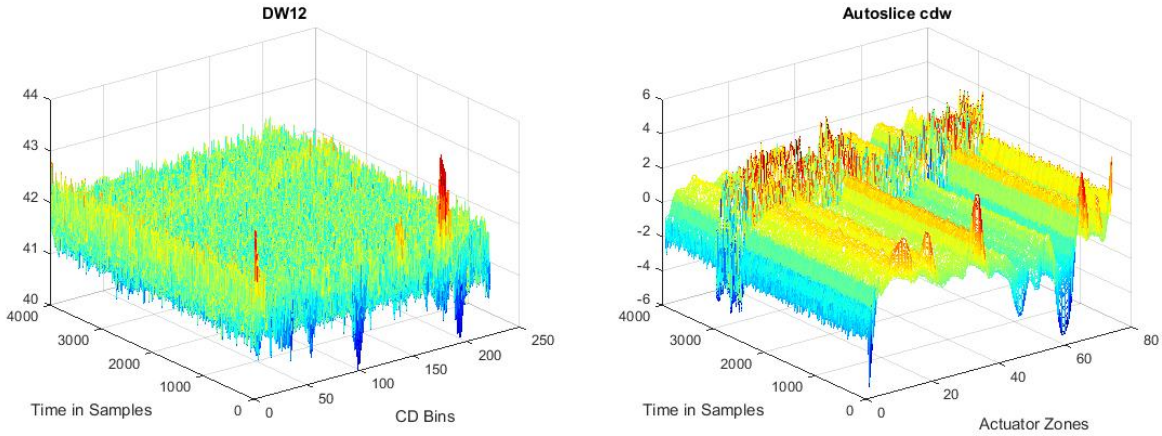

Figure 7.13: Attenuation mismatch: The collected output and input profiles

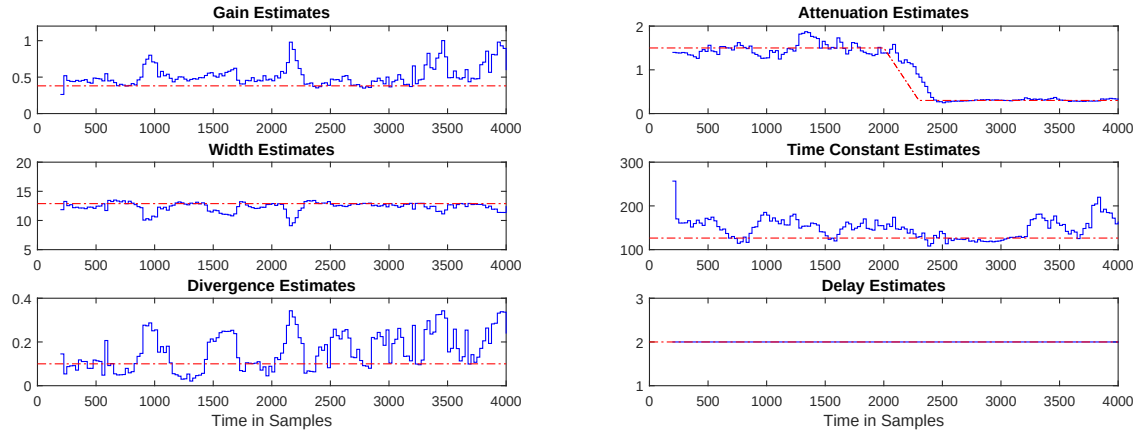

Figure 7.14: Attenuation mismatch: Estimates of parameters in each moving window

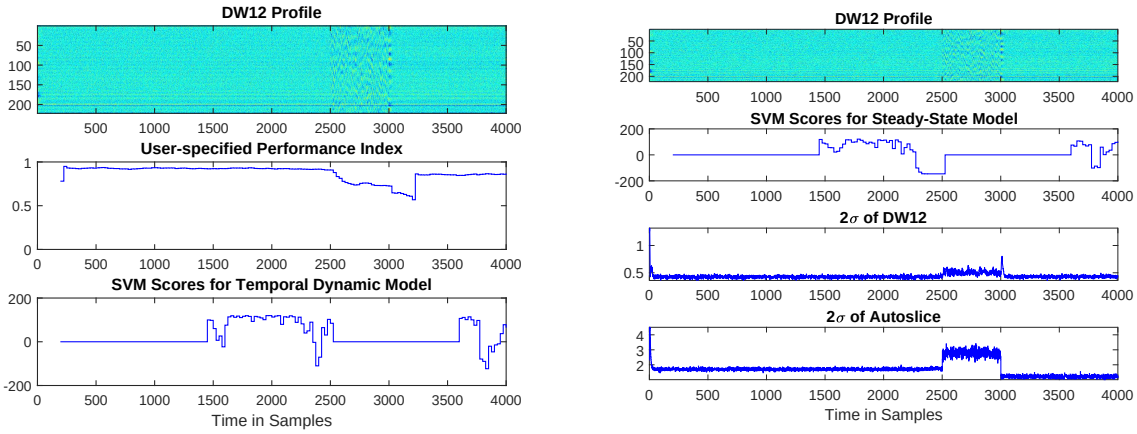

Figure 7.15: Attenuation mismatch: Adaptive CD MPC control results

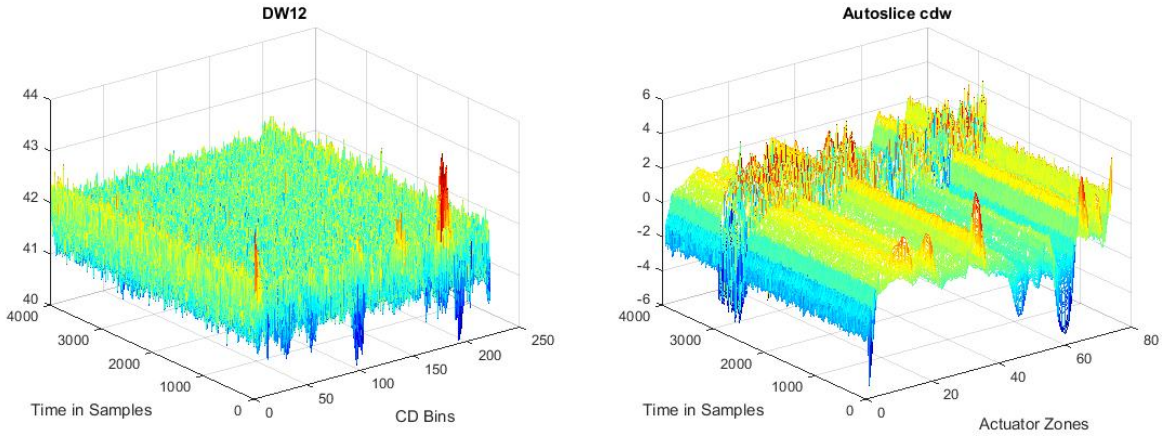

Figure 7.16: Time constant mismatch: The collected output and input profiles

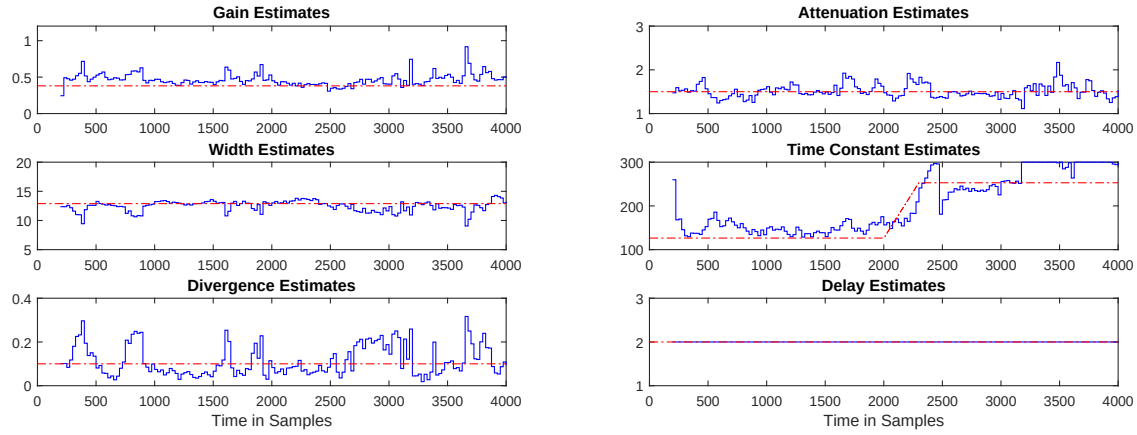

Figure 7.17: Time constant mismatch: Estimates of parameters in each moving window

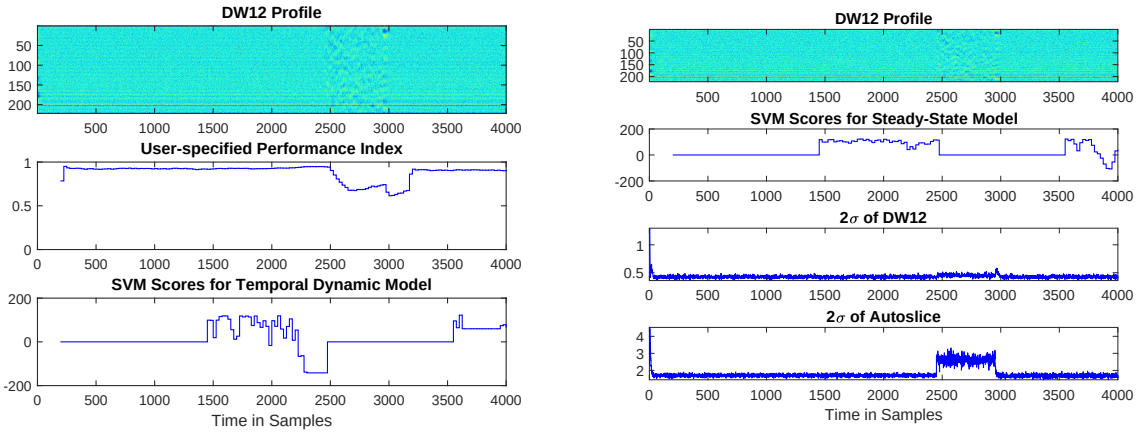

Figure 7.18: Time constant mismatch: Adaptive CD MPC control results

Chapter 8

Conclusions

This dissertation has detailed an adaptive MPC framework for both MD and CD processes. This entire adaptive control scheme consists of four building blocks, namely performance assessment, MPM detection, optimal input design and closed-loop identification. For MD processes, which can be represented by SISO or low-dimensional models, we mainly concentrate on the presentation of the proposed MPM detection and closed-loop identification methods. For CD processes, we extend the closed-loop identification and MPM detection method by accounting for high dimensions and structural features associated with the CD process. Besides, we propose a novel performance assessment technique and optimal input design approach that are computationally friendly and effective for adaptive control.

Specifically, for the closed-loop identification of MD processes, we present a novel ARX-OE method that is suitable for both routine operating data and experimental data. The proposed ARX-OE method avoids the bias issue due to the misspecification of noise model in direct identification method. There are two major steps in the proposed method. In the first step, the original model is approximated with a high-order ARX model and closed-loop identification is performed for the ARX model. In the second step, an OE identification is conducted with filtered input-output data based on the estimated ARX model from the first step. Theoretical analysis shows that the proposed ARX-OE method can provide consistent estimates for the parameters. We also present a thorough analysis on the informativeness of closed-loop data for this method.

For MD MPM detection, we apply the proposed ARX-OE method to routine operating data (split in to training and test sections) to obtain rough estimates for process and noise models. Model estimates from the training section are regarded as the normal cluster without MPM and a one-class SVM model is formed to depict this cluster. Model estimates from test data are examined by the SVM model to forecast the occurrence of MPM. This scheme can not only apply to routine data, but also discriminant the MPM from noise model changes, thus reducing the false alarms significantly. A resampling technique is proposed prior to performing the one-class SVM training to solve the small sample problem associated with the training data.

As for the CD process, we first demonstrate a practical approach for controller performance assessment as an extension of the MVC benchmark to large-scale systems. This CD MVC approach takes account of both spatial and temporal performance limitations associated with CD processes. Furthermore, to overcome the aggressiveness of this benchmark, we incorporate the information about tuning status of the CD controller, both in spatial and temporal directions, into a user-specified benchmark. An algorithm based on structured multivariate time series modeling is put forward to estimate the proposed CD performance index. Simple computation involved in this algorithm ensures the applicability of the proposed method for online performance monitoring.

We further extend the technique of MD MPM detection to CD processes. The main contribution is that we propose a novel CD closed-loop identification method based on separable least-squares and the closed-loop ARX-OE method. Conditions on the informativeness of closed-loop data are illustrated and it shows that most practical situations (e.g., complicated MPC constraints, presence of various disturbances and large time-delays) can provide informative enough data during routine operating stage. Furthermore, asymptotic analysis of the CD closed-loop identification shows that the proposed identification algorithm can converge to local minima and supply consistent estimates for the parameters. The SVM-based CD MPM detection method is then proposed that can monitoring spatial, temporal and noise models separately and operate with routine data that is absent of external excitations.

In terms of CD closed-loop optimal input design, we propose a noncausal method that is based on noncausal modeling of CD processes. This method can effectively address the complexity of input design for spatially distributed systems due to the large number of parameters. With noncausal modeling, a low-order scalar noncausal transfer function can be used to approximate the original high-dimensional CD model. It is shown that the covariance matrix of parameter estimates for this noncausal model is equivalent to that of a causal model. With this observation, a framework of closed-loop optimal input design is proposed based on the causal-equivalent model, which greatly reduces the difficulties in this process.

Finally, the proposed performance assessment, MPM detection, optimal input design and closed-loop identification methods are extensively tested on the CD and MD simulators. These simulators can provide high-fidelity simulations of practical operations of paper machines. The overall adaptive control scheme is also examined through examples by simulating various spatial and temporal parametric mismatches. These simulation results illustrate that the proposed framework can automatically account for process changes without human interventions. Thus with this adaptive control scheme, the industry can save enormous costs on

the maintenance of model-based controls. It is noted that the proposed scheme can also be easily transferred to other industrial processes.

Recommendations for future studies include further improvements on the closed-loop identification techniques for routine operating data especially when the controller is simple, e.g., PID controllers. A promising direction is to find more advanced and succinct representations than high-order ARX models to alleviate the requirements for the informativeness of closed-loop data. For example, the generalized orthonormal basis filter (GOBF) ARX models can serve as a better alternative than high-order ARX. Practical tricks such as using faster sampling rate to increase the time-delay can also enhance the quality of routine data. For closed-loop input design of noncausal CD processes, time domain approaches, especially the recent techniques developed based on graph theory, can be explored to meet physical constraints on inputs and outputs. Although there is potential for further improvement, our adaptive control scheme has reached to the stage of automatically monitoring the process and re-tuning controllers with feedback control in the loop and without user interruption.

Bibliography

[1] Stevo Mijanovic. *Paper machine cross-directional control near spatial domain boundaries*. PhD thesis, The University of British Columbia, Vancouver, Canada, 2004.

[2] Stephen R. Duncan. *The cross directional control of a web forming process*. PhD thesis, Imperial College London, London, UK, 1989.

[3] Rafael M. Morales and William P. Heath. The robustness and design of constrained cross-directional control via integral quadratic constraints. *IEEE Transactions on Control Systems Technology*, 19(6):1421–1432, 2011.

[4] Tapio Mäenpää. *Robust model predictive control for cross-directional processes*. Helsinki University of Technology, Helsinki, Finland, 2006.

[5] William P. Heath. Orthogonal functions for cross-directional control of web forming processes. *Automatica*, 32(2):183–198, 1996.

[6] Kristinn Kristinsson and Guy A. Dumont. Cross-directional control on paper machines using Gram polynomials. *Automatica*, 32(4):533–548, 1996.

[7] Petter Lundstrom, Sigurd Skogestad, and John C. Doyle. Two-degree-of-freedom controller design for an ill-conditioned distillation process using μ-synthesis. *IEEE Transactions on Control Systems Technology*, 7(1):12–21, 1999.

[8] Sigurd Skogestad, Manfred Morari, and John C. Doyle. Robust control of ill-conditioned plants: High-purity distillation. *IEEE Transactions on Automatic Control*, 33(12):1092–1105, 1988.

[9] Apostolos Rigopoulos and Yaman Arkun. Reduced order cross-directional controller design for sheet forming processes. *IEEE Transactions on Control Systems Technology*, 11(5):746–756, 2003.

[10] Dimitry Gorinevsky, Robert Vyse, and Michael Heaven. Performance analysis of cross-direction process control using multivariable and spectral models. *IEEE Transactions on Control Systems Technology*, 8(4):589–600, 2000.

[11] Gregory E. Stewart, Dimitry M. Gorinevsky, and Guy A. Dumont. Feedback controller design for a spatially distributed system: The paper machine problem. *IEEE Transactions on Control Systems Technology*, 11(5):612–628, 2003.

[12] Junqiang Fan. *Model predictive control for multiple cross-directional processes: Analysis, tuning and implementation*. PhD thesis, The University of British Columbia, Vancouver, Canada, 2003.

[13] Andrew P. Featherstone, Jeremy G. VanAntwerp, and Richard D. Braatz. *Identification and Control of Sheet and Film Processes*. Springer Science & Business Media, 2000.

[14] Jeremy G. VanAntwerp, Andrew P. Featherstone, Richard D. Braatz, and Babatunde A. Ogunnaike. Cross-directional control of sheet and film processes. *Automatica*, 43(2):191–211, 2007.

[15] Lennart Ljung. *System Identification: Theory for the User*. Springer, 1999.

[16] Michel Gevers, Xavier Bombois, Roland Hildebrand, and Gabriel Solari. Optimal experiment design for open and closed-loop system identification. *Communications in Information and Systems*, 11(3):197–224, 2011.

[17] S. Joe Qin. Control performance monitoring – A review and assessment. *Computers & Chemical Engineering*, 23(2):173–186, 1998.

[18] Biao Huang and Sirish L. Shah. *Performance Assessment of Control Loops: Theory and Applications*. Springer Science & Business Media, 1999.

[19] T.J. Harris, C.T. Seppala, and L.D. Desborough. A review of performance monitoring and assessment techniques for univariate and multivariate control systems. *Journal of Process Control*, 9(1):1–17, 1999.

[20] Sigurd Skogestad and Ian Postlethwaite. *Multivariable Feedback Control: Analysis and Design*, volume 2. Wiley New York, 2007.

[21] Thomas J. Harris. Assessment of control loop performance. *The Canadian Journal of Chemical Engineering*, 67(5):856–861, 1989.

[22] Thomas J. Harris, F. Boudreau, and John F. MacGregor. Performance assessment of multivariable feedback controllers. *Automatica*, 32(11):1505–1518, 1996.

[23] Jie Yu and S. Joe Qin. Statistical MIMO controller performance monitoring. Part II: Performance diagnosis. *Journal of Process Control*, 18(3):297–319, 2008.

[24] C.B. Lynch and Guy A. Dumont. Control loop performance monitoring. *IEEE transactions on Control Systems Technology*, 4(2):185–192, 1996.

[25] Biao Huang, Sirish L. Shah, K. Ezra Kwok, and Jim Zurcher. Performance assessment of multivariate control loops on a paper-machine headbox. *The Canadian Journal of Chemical Engineering*, 75(1):134–142, 1997.

[26] N.F. Thornhill, M. Oettinger, and P. Fedenczuk. Refinery-wide control loop performance assessment. *Journal of Process Control*, 9(2):109–124, 1999.

[27] M.J. Grimble. Generalized minimum variance control law revisited. *Optimal Control Applications and Methods*, 9(1):63–77, 1988.

[28] M.J. Grimble and P. Majecki. Weighting selection for controller benchmarking and tuning. *Industrial Control Centre, University of Strathclyde, Technical Report PAM-12-TN-1-V1, Glasgow*, 2004.

[29] Andrzej Ordys, Damien Uduehi, and Michael A. Johnson. *Process Control Performance Assessment: from Theory to Implementation*. Springer Science & Business Media, 2007.

[30] Mohieddine Jelali. *Control Performance Management in Industrial Automation: Assessment, Diagnosis and Improvement of Control Loop Performance*. Springer Science & Business Media, 2012.

[31] Byung-Su Ko and Thomas F. Edgar. Performance assessment of constrained model predictive control systems. *AIChE Journal*, 47(6):1363–1371, 2001.

[32] Ashraf AlGhazzawi and Barry Lennox. Model predictive control monitoring using multivariate statistics. *Journal of Process Control*, 19(2):314–327, 2009.

[33] Stephen R. Duncan, Guy A. Dumont, and Dimitry M. Gorinevsky. Evaluating the performance of cross-directional control systems. In *Proceedings of the 1999 American Control Conference*, volume 5, pages 3092–3096, 1999.

[34] Stephen R. Duncan, Guy A. Dumont, and Dimitry M. Gorinevsky. Performance monitoring for cross-directional control systems. *Proceedings of the Control Systems Conference*, pages 173–177, 2000.

[35] A.R. Taylor and Stephen R. Duncan. Bayesian methods for control loop performance assessment in cross-directional control. *IFAC Proceedings Volumes*, 38(1):434–439, 2005.

[36] Mahdi Yousefi. *Performance assessment and online input design for closed-loop identification of machine directional properties on paper machines*. Master Thesis, The University of British Columbia, Vancouver, Canada, 2014.

[37] Siyun Wang and Michael Baldea. Autocovariance-based MPC model mismatch estimation for SISO systems. In *2015 the 54th IEEE Conference on Decision and Control (CDC)*, pages 3032–3037, 2015.

[38] Viviane Botelho, Jorge Otávio Trierweiler, Marcelo Farenzena, and Ricardo Duraiski. Perspectives and challenges in performance assessment of model predictive control. *The Canadian Journal of Chemical Engineering*, 94(7):1225–1241, 2016.

[39] Rohit S. Patwardhan and Sirish L. Shah. Issues in performance diagnostics of model-based controllers. *Journal of Process Control*, 12(3):413–427, 2002.

[40] Nives Stanfelj, Thomas E. Marlin, and John F. MacGregor. Monitoring and diagnosing process control performance: The single-loop case. *Industrial & Engineering Chemistry Research*, 32(2):301–314, 1993.

[41] Parthasarathy Kesavan and Jay H. Lee. Diagnostic tools for multivariable model-based control systems. *Industrial & Engineering Chemistry Research*, 36(7):2725–2738, 1997.

[42] Fredrik Gustafsson and Stefan F. Graebe. Closed-loop performance monitoring in the presence of system changes and disturbances. *Automatica*, 34(11):1311–1326, 1998.

[43] Biao Huang. Multivariable model validation in the presence of time-variant disturbance dynamics. *Chemical Engineering Science*, 55(20):4583–4595, 2000.

[44] Michele Basseville. On-board component fault detection and isolation using the statistical local approach. *Automatica*, 34(11):1391–1415, 1998.

[45] Biao Huang, Ashish Malhotra, and Edgar C. Tamayo. Model predictive control relevant identification and validation. *Chemical Engineering Science*, 58(11):2389–2401, 2003.

[46] Qiang Zhang and Shao-Yuan Li. Performance monitoring and diagnosis of multivariable model predictive control using statistical analysis. *Chinese Journal of Chemical Engineering*, 14(2):207–215, 2006.

[47] Jeremy S. Conner and Dale E. Seborg. Assessing the need for process re-identification. *Industrial & Engineering Chemistry Research*, 44(8):2767–2775, 2005.

[48] Abhijit S. Badwe, Ravindra D. Gudi, Rohit S. Patwardhan, Sirish L. Shah, and Sachin C. Patwardhan. Detection of model-plant mismatch in MPC applications. *Journal of Process Control*, 19(8):1305–1313, 2009.

[49] Christopher A. Harrison and S. Joe Qin. Discriminating between disturbance and process model mismatch in model predictive control. *Journal of Process Control*, 19(10):1610–1616, 2009.

[50] Abhijit S. Badwe, Rohit S. Patwardhan, Sirish L. Shah, Sachin C. Patwardhan, and Ravindra D. Gudi. Quantifying the impact of model-plant mismatch on controller performance. *Journal of Process Control*, 20(4):408–425, 2010.

[51] Zhijie Sun, S. Joe Qin, Ashish Singhal, and Larry Megan. Performance monitoring of model-predictive controllers via model residual assessment. *Journal of Process Control*, 23(4):473–482, 2013.

[52] Suraj Yerramilli and Arun K. Tangirala. Detection and diagnosis of model-plant mismatch in MIMO systems using plant-model ratio. *IFAC-PapersOnLine*, 49(1):266–271, 2016.

[53] Graham C. Goodwin and Robert L. Payne. *Dynamic System Identification: Experiment Design and Data Analysis*. Academic Press, 1977.

[54] Raman K. Mehra. Optimal input signals for parameter estimation in dynamic systems–Survey and new results. *IEEE Transactions on Automatic Control*, 19(6):753–768, 1974.

[55] Martin B. Zarrop. *Optimal experiment design for dynamic system identification*. PhD thesis, Imperial College London, London, UK, 1977.

[56] Lennart Ljung and Zhen-Dong Yuan. Asymptotic properties of black-box identification of transfer functions. *IEEE Transactions on Automatic Control*, 30(6):514–530, 1985.

[57] Lennart Ljung. Asymptotic variance expressions for identified black-box transfer function models. *IEEE Transactions on Automatic Control*, 30(9):834–844, 1985.

[58] Michel Gevers and Lennart Ljung. Optimal experiment designs with respect to the intended model application. *Automatica*, 22(5):543–554, 1986.

[59] Håkan Hjalmarsson, Michel Gevers, and Franky D. Bruyne. For model-based control design, closed-loop identification gives better performance. *Automatica*, 32(12):1659–1673, 1996.

[60] Stephen P. Boyd, Laurent E.I. Ghaoui, Eric Feron, and Venkataramanan Balakrishnan. *Linear Matrix Inequalities in System and Control Theory*. SIAM, 1994.

[61] Xavier Bombois, Håkan Hjalmarsson, and Gérard Scorletti. Identification for robust H_2 deconvolution filtering. *Automatica*, 46(3):577–584, 2010.

[62] Henrik Jansson and Håkan Hjalmarsson. Input design via lmis admitting frequency-wise model specifications in confidence regions. *IEEE transactions on Automatic Control*, 50(10):1534–1549, 2005.

[63] Henrik Jansson. *Experiment design with applications in identification for control*. PhD thesis, Royal Institute of Technology (KTH), 2004.

[64] Afrooz Ebadat. *On application oriented experiment design for closed-loop system identification*. PhD thesis, Kungliga Tekniska högskolan, 2015.

[65] Patricio E. Valenzuela, Cristian R. Rojas, and Håkan Hjalmarsson. A graph theoretical approach to input design for identification of nonlinear dynamical models. *Automatica*, 51:233–242, 2015.

[66] R. Isermann and M. Münchhof. *Identification of Dynamic Systems: An Introduction with Applications*. Springer, Berlin and Heidelberg, 2011.

[67] Yucai Zhu and Przemyskaw Stec. Simple control-relevant identification test methods for a class of ill-conditioned processes. *Journal of Process Control*, 16(10):1113–1120, 2006.

[68] Osmel R. Vaillant, Andre S.R. Kuramoto, and Claudio Garcia. Effectiveness of signal excitation design methods for identification of ill-conditioned and highly interactive processes. *Industrial & Engineering Chemistry Research*, 52(14):5120–5135, 2013.

[69] Mark L. Darby and Michael Nikolaou. Identification test design for multivariable model-based control: An industrial perspective. *Control Engineering Practice*, 22:165–180, 2014.

[70] Andrea Micchi and Gabriele Pannocchia. Comparison of input signals in subspace identification of multivariable ill-conditioned systems. *Journal of Process Control*, 18(6):582–593, 2008.

[71] Mohammed Ammar and Guy A. Dumont. Input design minimizing the μ-gap in cross-directional models of paper machines. In *Proceedings of the 2006 American Control Conference*, pages 3795–3800, 2006.

[72] Danlei Chu, J.U. Backström, C. Gheorghe, A. Lahouaoula, and C. Chung. Intelligent closed loop CD alignment. In *Proceedings of Control Systems*, pages 161–166, 2010.

[73] Urban Forssell and Lennart Ljung. Closed-loop identification revisited. *Automatica*, 35(7):1215–1241, 1999.

[74] Wee S. Lee, Brian D. Anderson, Iven M. Mareels, and Robert L. Kosut. On some key issues in the windsurfer approach to adaptive robust control. *Automatica*, 31(11):1619–1636, 1995.

[75] Jiandong Wang, Tongwen Chen, and Biao Huang. Closed-loop identification via output fast sampling. *Journal of Process Control*, 14(5):555–570, 2004.

[76] Michel Gevers, Lennart Ljung, and Paul Van den Hof. Asymptotic variance expressions for closed-loop identification. *Automatica*, 37(5):781–786, 2001.

[77] Ali Esmaili, John F. MacGregor, and Paul A. Taylor. Direct and two-step methods for closed-loop identification: a comparison of asymptotic and finite data set performance. *Journal of Process Control*, 10(6):525–537, 2000.

[78] Ivar Gustavsson, Lennart Ljung, and Torsten Söderström. Identification of processes in closed loop–identifiability and accuracy aspects. *Automatica*, 13(1):59–75, 1977.

[79] Paul M.J. Vandenhof and Ruud J.P. Schrama. An indirect method for transfer-function estimation from closed-loop data. *Automatica*, 29(6):1523–1527, 1993.

[80] Urban Forssell and Lennart Ljung. A projection method for closed-loop identification. *IEEE Transactions on Automatic Control*, 45(11):2101–2106, 2000.

[81] Luis G. Bergh and John F. MacGregor. Spatial control of sheet and film forming processes. *The Canadian Journal of Chemical Engineering*, 65(1):148–155, 1987.

[82] R. Bhushan Gopaluni, Mohammed Loewen, Philip D .and Ammar, Guy A. Dumont, and Michael S. Davies. Identification of symmetric noncausal processes: cross-directional response modelling of paper machines. In *Proceedings of the 45th IEEE Conference on Decision and Control*, pages 6744–6749, 2006.

[83] Dimitry M. Gorinevsky and Cristian Gheorghe. Identification tool for cross-directional processes. *IEEE Transactions on Control Systems Technology*, 11(5):629–640, 2003.

[84] Mohammed E. Ammar and Guy A. Dumont. Automatic tuning of robust constrained cross-direction controllers. *International Journal of Adaptive Control and Signal Processing*, 30(11):1550–1567, 2016.

[85] Lee Rippon. *Sheet profile estimation and machine direction adaptive control*. Master Thesis, The University of British Columbia, Vancouver, Canada, 2017.

[86] Yuri A.W. Shardt and Biao Huang. Closed-loop identification condition for ARMAX models using routine operating data. *Automatica*, 47(7):1534–1537, 2011.

[87] Abhijit S. Badwe, Sachin C. Patwardhan, and Ravindra D. Gudi. Closed-loop identification using direct approach and high order ARX/GOBF-ARX models. *Journal of Process Control*, 21(7):1056–1071, 2011.

[88] Lennart Ljung and Bo Wahlberg. Asymptotic properties of the least-squares method for estimating transfer functions and disturbance spectra. *Advances in Applied Probability*, 24(02):412–440, 1992.

[89] Yucai Zhu and Håkan Hjalmarsson. The Box–Jenkins Steiglitz–McBride algorithm. *Automatica*, 65:170–182, 2016.

[90] Yucai Zhu. Multivariable process identification for MPC: the asymptotic method and its applications. *Journal of Process Control*, 8(2):101–115, 1998.

[91] Svante Björklund and Lennart Ljung. A review of time-delay estimation techniques. In *Proceedings of the 42nd IEEE Conference on Decision and Control*, volume 3, pages 2502–2507, 2003.

[92] S. Babji and Arun K. Tangirala. Time-delay estimation in closed-loop processes using average mutual information theory. *Control & Intelligent Systems*, 37(3):176–182, 2009.

[93] Michel Gevers, Alexandre Sanfelice Bazanella, and Xavier Bombois. Identification and the information matrix: How to get just sufficiently rich? *IEEE Transactions on Automatic Control*, 54(12):2828–2840, 2009.

[94] Torsten Söderström and Petre Stoica. *System Identification*. Prentice-Hall, Inc., 1988.

[95] Q. Li, J.R. Whiteley, and R.R. Rhinehart. A relative performance monitor for process controllers. *International Journal of Adaptive Control and Signal Processing*, 17(7-9):685–708, 2003.

[96] Corinna Cortes and Vladimir Vapnik. Support-vector networks. *Machine Learning*, 20(3):273–297, 1995.

[97] Ingo Steinwart and Andreas Christmann. *Support Vector Machines*. Springer Science & Business Media, 2008.

[98] Bernhard Schölkopf, John C. Platt, John Shawe-Taylor, Alex J. Smola, and Robert C. Williamson. Estimating the support of a high-dimensional distribution. *Neural Computation*, 13(7):1443–1471, 2001.

[99] Osvaldo J. Rojas, Graham C. Goodwin, and André Desbiens. Study of an adaptive anti-windup strategy for cross-directional control systems. In *Proceedings of the 41st IEEE Conference on Decision and Control*, volume 2, pages 1331–1336, 2002.

[100] G.E. Stewart, J.U. Backstrom, P. Baker, C. Gheorghe, and R.N. Vyse. Controllability in cross-directional processes: Practical rules for analysis and design. In *The 87th Annual meeting, PAPTAC*, pages 1–8, 2001.

[101] G.E. Stewart, J.U. Backström, P. Baker, C. Gheorghe, and R.N. Vyse. Controllability in cross-directional processes. *Pulp & Paper Canada*, 103(8):32–38, 2002.

[102] Zhijie Sun, Yu Zhao, and S. Joe Qin. Improving industrial MPC performance with data-driven disturbance modeling. In *Proceedings of the 50th IEEE Conference on Decision and Control and European Control Conference (CDC-ECC)*, pages 1922–1927, 2011.

[103] Junqiang Fan, Gregory E. Stewart, and Guy A. Dumont. Two-dimensional frequency analysis for unconstrained model predictive control of cross-directional processes. *Automatica*, 40(11):1891–1903, 2004.

[104] Dimitry Gorinevsky, Stephen Boyd, and Gunter Stein. Design of low-bandwidth spatially distributed feedback. *IEEE Transactions on Automatic Control*, 53(1):257–272, 2008.

[105] Bassam Bamieh, Fernando Paganini, and Munther A. Dahleh. Distributed control of spatially invariant systems. *IEEE Transactions on Automatic Control*, 47(7):1091–1107, 2002.

[106] Helmut Lütkepohl. *New Introduction to Multiple Time Series Analysis*. Springer Science & Business Media, 2005.

[107] Yang Wang and Stephen Boyd. Performance bounds and suboptimal policies for linear stochastic control via LMIs. *International Journal of Robust and Nonlinear Control*, 21(14):1710–1728, 2011.

[108] K.S. Narendra and P.G. Gallman. An iterative method for the identification of nonlinear systems using a Hammerstein model. *IEEE Transactions on Automatic Control*, 11(3):546–550, 1966.

[109] Fouad Giri and Er-Wei Bai. *Block-oriented Nonlinear System Identification*, volume 1. Springer, 2010.

[110] James B. Rawlings and I-Lung Chien. Gage control of film and sheet-forming processes. *AIChE Journal*, 42(3):753–766, 1996.

[111] Apostolos Rigopoulos, Yaman Arkun, and Ferhan Kayihan. Identification of full profile disturbance models for sheet forming processes. *AIChE Journal*, 43(3):727–739, 1997.

[112] Yucai Zhu. Estimation of an N–L–N Hammerstein–Wiener model. *Automatica*, 38(9):1607–1614, 2002.

[113] Alberto Bemporad, Manfred Morari, Vivek Dua, and Efstratios N. Pistikopoulos. The explicit linear quadratic regulator for constrained systems. *Automatica*, 38(1):3–20, 2002.

[114] Gene Golub and Victor Pereyra. Separable nonlinear least squares: the variable projection method and its applications. *Inverse Problems*, 19(2):R1–R26, 2003.

[115] Er-Wei Bai and Duan Li. Convergence of the iterative Hammerstein system identification algorithm. *IEEE Transactions on Automatic Control*, 49(11):1929–1940, 2004.

[116] Gene H. Golub and Victor Pereyra. The differentiation of pseudo-inverses and nonlinear least squares problems whose variables separate. *SIAM Journal on Numerical Analysis*, 10(2):413–432, 1973.

[117] Kaushik Mahata and Torsten Söderström. Large sample properties of separable nonlinear least squares estimators. *IEEE Ttransactions on Signal Processing*, 52(6):1650–1658, 2004.

[118] Qiugang Lu, Michael G. Forbes, R. Bhushan Gopaluni, Philip D. Loewen, Johan U. Backström, and Guy A. Dumont. Performance assessment of cross-directional control for paper machines. *IEEE Transactions on Control Systems Technology*, 25(1):208–221, 2017.

[119] Walter Rudin. *Principles of Mathematical Analysis.* New York, NY: McGraw-Hill, Inc., 1976.

[120] Stephen R. Duncan and K.W. Corscadden. Mini-max control of cross-directional variations on a paper machine. *IEE Proceedings-Control Theory and Applications*, 145(2):189–195, 1998.

[121] Lennart Ljung. Convergence analysis of parametric identification methods. *IEEE Transactions on Automatic Control*, 23(5):770–783, 1978.

Appendix A

Proofs for Chapter 2

A.1 Proof of Theorem 2.4.1

Let us begin by defining an auxiliary term, $\varepsilon(t,\rho)$, as follows

$$\varepsilon(t,\rho) = [G_0 - G(q,\rho)]u(t) + \frac{1}{A(q,\eta_0)}e(t).$$

Notice that with the presence of feedback, one may consider $u(t)$ to be generated by passing the reference signal $r(t)$ and external noise $e(t)$ through a set of uniformly stable filters. Note, from Assumptions 2.2.2 and 2.2.3, that $A(q,\eta_0)$ is inversely stable and thus $\varepsilon(t,\rho)$ meets the conditions of Theorem 2B.1 in [15]. Therefore,

$$\varepsilon(t,\rho,\hat{\eta}_N) = A(q,\hat{\eta}_N)\varepsilon(t,\rho), \;\; \varepsilon(t,\rho,\eta_0) = A(q,\eta_0)\varepsilon(t,\rho),$$

and

$$V_N(\rho,\hat{\eta}_N) = \frac{1}{N}\sum_{t=1}^{N}\frac{1}{2}\left[A(q,\hat{\eta}_N)\varepsilon(t,\rho)\right]^2, \;\; V_N(\rho,\eta_0) = \frac{1}{N}\sum_{t=1}^{N}\frac{1}{2}\left[A(q,\eta_0)\varepsilon(t,\rho)\right]^2.$$

Furthermore, we can decompose the loss function as

$$\begin{aligned} V_N(\rho,\hat{\eta}_N) \;\; = \;\; & \frac{1}{N}\sum_{t=1}^{N}\left\{\frac{1}{2}\left[A(q,\eta_0)\varepsilon(t,\rho)\right]^2 + \frac{1}{2}\left[(A(q,\hat{\eta}_N) - A(q,\eta_0))\varepsilon(t,\rho)\right]\right. \\ & \left.\cdot\left[A(q,\eta_0)\varepsilon(t,\rho)\right] + \frac{1}{2}\left[(A(q,\hat{\eta}_N) - A(q,\eta_0))\varepsilon(t,\rho)\right]\left[A(q,\hat{\eta}_N)\varepsilon(t,\rho)\right]\right\}. \end{aligned}$$

Due to the Theorem 2B.1 in [15], we have

$$\sup_{\rho\in\Omega_\rho}\left\|\frac{1}{N}\sum_{t=1}^{N}\frac{1}{2}\left[A(q,\eta_0)\varepsilon(t,\rho)\right]^2 - \overline{V}(\rho,\eta_0)\right\| \to 0, \;\; \text{w.p.1, as } N\to\infty,$$

where

$$\overline{V}(\rho,\eta_0)=\overline{\mathbb{E}}\frac{1}{2}\left[A(q,\eta_0)\varepsilon(t,\rho)\right]^2.$$

Since $\varepsilon(t,\rho)$ is bounded uniformly, from Lemma 2.3.1, it follows that

$$\sup_{\rho\in\Omega_\rho}\left\|\frac{1}{N}\sum_{t=1}^{N}\left[\left(A(q,\hat{\eta}_N)-A(q,\eta_0)\right)\varepsilon(t,\rho)\right]\left[A(q,\eta_0)\varepsilon(t,\rho)\right]\right\|\to 0,\ \text{ w.p.1, as } N\to\infty,$$
$$\sup_{\rho\in\Omega_\rho}\left\|\frac{1}{N}\sum_{t=1}^{N}\left[\left(A(q,\hat{\eta}_N)-A(q,\eta_0)\right)\varepsilon(t,\rho)\right]\left[A(q,\hat{\eta}_N)\varepsilon(t,\rho)\right]\right\|\to 0,\ \text{ w.p.1, as } N\to\infty.$$

Applying the triangular inequality yields,

$$\begin{aligned}\sup_{\rho\in\Omega_\rho}\left\|V_N(\rho,\hat{\eta}_N)-\overline{V}(\rho,\eta_0)\right\| \le & \sup_{\rho\in\Omega_\rho}\left\|\frac{1}{N}\sum_{t=1}^{N}\frac{1}{2}\left[A(q,\eta_0)\varepsilon(t,\rho)\right]^2-\overline{\mathbb{E}}\frac{1}{2}\left[A(q,\eta_0)\varepsilon(t,\rho)\right]^2\right\| \\ & +\sup_{\rho\in\Omega_\rho}\left\|\frac{1}{2N}\sum_{t=1}^{N}\left[\left(A(q,\hat{\eta}_N)-A(q,\eta_0)\right)\varepsilon(t,\rho)\right]\left[A(q,\eta_0)\varepsilon(t,\rho)\right]\right\| \\ & +\sup_{\rho\in\Omega_\rho}\left\|\frac{1}{2N}\sum_{t=1}^{N}\left[\left(A(q,\hat{\eta}_N)-A(q,\eta_0)\right)\varepsilon(t,\rho)\right]\left[A(q,\hat{\eta}_N)\varepsilon(t,\rho)\right]\right\| \\ \to 0,\ & \text{ w.p.1, as } N\to\infty.\end{aligned}$$

Hence the conclusion of Theorem 2.4.1 in (2.20) can be achieved.

A.2 Proof of Theorem 2.4.3

Assume that in (2.14) the model structure $G(q,\rho)$ contains the true process model $G_0(q)$. Following a similar line of the proof for Theorem 9.1 in [15], the optimum $\hat{\rho}_N$ in (2.17) satisfies

$$\mathbf{V}_N'(\hat{\rho}_N,\hat{\eta}_N)=0.$$

Re-writing the above equation using a first-order Taylor expansion at ρ_0, we have

$$0=\mathbf{V}_N'(\rho_0,\hat{\eta}_N)+\mathbf{V}_N''(\xi_N,\hat{\eta}_N)(\hat{\rho}_N-\rho_0),\ \ \xi_N\in[\hat{\rho}_N,\ \rho_0].$$

Thus the asymptotic distribution $\sqrt{N}(\hat{\rho}_N - \rho_0)$ can be determined by

$$\sqrt{N}(\hat{\rho}_N - \rho_0) = -[\mathbf{V}''_N(\xi_N, \hat{\eta}_N)]^{-1}\sqrt{N}\mathbf{V}'_N(\rho_0, \hat{\eta}_N). \tag{A.1}$$

In what follows we will study the distribution $\sqrt{N}\mathbf{V}'_N(\rho_0, \hat{\eta}_N)$ first, followed by an analysis on the asymptotic behavior of $\mathbf{V}''_N(\xi_N, \hat{\eta}_N)$.

(1) Asymptotic Analysis of $\sqrt{N}\mathbf{V}'_N(\rho_0, \hat{\eta}_N)$

From the definition (2.17) we have

$$-\mathbf{V}'_N(\rho_0, \hat{\eta}_N) = \frac{1}{N}\sum_{t=1}^{N} \psi(t, \rho_0, \hat{\eta}_N)\varepsilon(t, \rho_0, \hat{\eta}_N), \tag{A.2}$$

where $\psi(t, \rho, \hat{\eta}_N)$ is the derivative of the predictor (2.15) with respect to the parameter ρ, i.e.,

$$\psi(t, \rho_0, \hat{\eta}_N) = \mathbf{G}'_\rho(\rho_0)u(t, \hat{\eta}_N). \tag{A.3}$$

The specific expression of $\varepsilon(t, \rho_0, \hat{\eta}_N)$ in (A.2) is

$$\varepsilon(t, \rho_0, \hat{\eta}_N) = \frac{A(q, \hat{\eta}_N)}{A_0(q)}e(t). \tag{A.4}$$

Instead of studying $-\sqrt{N}\mathbf{V}'_N(\rho_0, \hat{\eta}_N)$ in (A.2), we can analyze its asymptotic distribution by studying

$$\frac{1}{\sqrt{N}}\sum_{t=1}^{N} \psi(t, \rho_0, \eta_0)\varepsilon(t, \rho_0, \hat{\eta}_N), \tag{A.5}$$

since the mean-squared error between them approaches zero as N goes to infinity. This can be verified based on Lemma 2.3.1. From (2.24), the signal $u(t, \eta_0)$ can be represented by

$$u(t, \eta_0) = A_0(q)S_0(q)r(t) - S_0(q)K(q)e(t), \tag{A.6}$$

where $\{r(t)\}$ and $\{e(t)\}$ are independent sequences. It can be observed from (A.3) and (A.4) that

$$\frac{1}{\sqrt{N}}\sum_{t=1}^{N} \psi(t, \rho_0, \eta_0)\varepsilon(t, \rho_0, \hat{\eta}_N) \quad = \quad \mathbf{Z}_1(N) + \mathbf{Z}_2(N),$$

where

$$\begin{aligned}\mathbf{Z}_1(N) &= \frac{1}{\sqrt{N}}\sum_{t=1}^{N}\psi(t,\rho_0,\eta_0)e(t),\\ \mathbf{Z}_2(N) &= \frac{1}{\sqrt{N}}\sum_{t=1}^{N}\psi(t,\rho_0,\eta_0)\frac{A(q,\hat{\eta}_N)-A_0(q)}{A_0(q)}e(t).\end{aligned}$$

Note that the derivation of (9A.25) in [15] applies to both open-loop and closed-loop data. Thus we have

$$Cov[\sqrt{N}\mathbf{V}'_N(\rho_0,\hat{\eta}_N)] = \mathbf{Q},$$

where

$$\mathbf{Q} = \lim_{N\to\infty} N\cdot\mathbb{E}\{\mathbf{V}'_N(\rho_0,\hat{\eta}_N)[\mathbf{V}'_N(\rho_0,\hat{\eta}_N)]^T\}. \tag{A.7}$$

With the above notions, the $\mathbf{Q}$ in (A.7) is shown to be

$$\begin{aligned}\mathbf{Q} &= \lim_{N\to\infty}\mathbb{E}[\mathbf{Z}_1(N)+\mathbf{Z}_2(N)][\mathbf{Z}_1(N)+\mathbf{Z}_2(N)]^T\\ &= \lim_{N\to\infty}\mathbb{E}[\mathbf{Z}_1(N)\mathbf{Z}_1^T(N)]+\mathbb{E}[\mathbf{Z}_2(N)\mathbf{Z}_2^T(N)]+\mathbb{E}[\mathbf{Z}_1(N)\mathbf{Z}_2^T(N)]+\mathbb{E}[\mathbf{Z}_2(N)\mathbf{Z}_1^T(N)].\end{aligned} \tag{A.8}$$

For the first term of (A.8), by substituting (A.6) into (A.3) we have

$$\psi(t,\rho_0,\eta_0) = \phi_r(t)-\phi_e(t), \tag{A.9}$$

where

$$\phi_r(t) = \mathbf{G}'_\rho(\rho_0)S_0A(\eta_0)r(t), \tag{A.10}$$

$$\phi_e(t) = \mathbf{G}'_\rho(\rho_0)KS_0e(t). \tag{A.11}$$

Notice that $\phi_r(t)$ is a deterministic signal. Furthermore from our previous assumption, the process model G_0 always contains at least one delay and so does $\mathbf{G}'_\rho(\rho_0)$. Therefore, $\psi(t,\rho_0,\eta_0)$ is independent of $e(t)$. From

Lemma 2.4.2, it is easy to see that

$$\begin{aligned}\lim_{N\to\infty}\mathbb{E}[\mathbf{Z}_1(N)\mathbf{Z}_1^T(N)] &= \lim_{N\to\infty}\frac{1}{N}\sigma_e^2\sum_{t=1}^{N}\mathbb{E}[\psi(t,\rho_0,\eta_0)\psi^T(t,\rho_0,\eta_0)]\\ &= \sigma_e^2\overline{\mathbb{E}}[\psi(t,\rho_0,\eta_0)\psi^T(t,\rho_0,\eta_0)]\\ &= \sigma_e^2\overline{\mathbb{E}}\phi_r(t)\phi_r^T(t)+\sigma_e^2\overline{\mathbb{E}}[\phi_e(t)\phi_e^T(t)]. \end{aligned}\tag{A.12}$$

For the second term of (A.8), based on a similar argument as that in [89], we consider the auto-covariance of

$$\tilde{\mathbf{Z}}_2(N)=\mathbf{Z}_2^{n(N)}\sqrt{N}(\hat{\eta}_N-\bar{\eta}_{n(N)}),\tag{A.13}$$

where

$$\mathbf{Z}_2^{n(N)}=\overline{\mathbb{E}}\left[\psi(t,\rho_0,\eta_0)\cdot[\Gamma_{n(N)}^T\ \ \mathbf{0}_{1\times n(N)}]\frac{1}{A_0(q)}e(t)\right],$$

and

$$\hat{\eta}_N\to\bar{\eta}_{n(N)},\ \text{ w.p.1, as } N\to\infty,$$

since the mean-squared error between (A.13) and $\mathbf{Z}_2(N)$ tends to zero as $N\to 0$. Note that the matrix $\mathbf{Z}_2^{n(N)}\in\mathbb{R}^{n_\rho\times n(N)}$ is deterministic and satisfies the condition of Theorem D.3 in [89], thus theorem D.3 can be immediately applied to (A.13). Before demonstrating the main result, let us first explore the specific expression of $\mathbf{Z}_2^{n(N)}$. From (A.9) we have

$$\begin{aligned}\mathbf{Z}_2^{n(N)} &= \overline{\mathbb{E}}\left[(\phi_r(t)-\phi_e(t))\cdot[\Gamma_{n(N)}^T\ \ \mathbf{0}_{1\times n(N)}]\frac{1}{A_0(q)}e(t)\right]\\ &= -\overline{\mathbb{E}}\left[\phi_e(t)\cdot[\Gamma_{n(N)}^T\ \ \mathbf{0}_{1\times n(N)}]\frac{1}{A_0(q)}e(t)\right]\\ &= -\left[\overline{\mathbb{E}}[\mathbf{G}_\rho'(\rho_0)S_0Ke(t)\cdot\Gamma_{n(N)}^TH_0e(t)]\ \ \mathbf{0}_{1\times n(N)}\right].\end{aligned}\tag{A.14}$$

Then from Theorem D.3 in [89], the asymptotic auto-covariance of $\mathbf{Z}_2(N)$ is

$$\lim_{N\to\infty}\mathbb{E}[\mathbf{Z}_2(N)\mathbf{Z}_2^T(N)]=\lim_{N\to\infty}\mathbf{Z}_2^{n(N)}[\overline{\mathbf{R}}^{n(N)}]^{-1}(\mathbf{Z}_2^{n(N)})^T,\tag{A.15}$$

where $\bar{\mathbf{R}}^n$ was defined in (2.27).

For the third term of (A.8), to simplify the analysis, we consider the cross-covariance between $\mathbf{Z}_1(N)$

and

$$\overline{\mathbf{Z}}_2(N) = \mathbf{Z}_2^{n(N)}[\overline{\mathbf{R}}^{n(N)}]^{-1}\frac{1}{\sqrt{N}}\sum_{t=1}^{N}\varphi_t^{n(N)}e(t),$$

where $\varphi_t^{n(N)}$ was defined in (2.29). Therefore, the cross-covariance between $\overline{\mathbf{Z}}_2(N)$ and $\mathbf{Z}_1^T(N)$ gives

$$\begin{aligned}\lim_{N\to\infty}\mathbb{E}[\overline{\mathbf{Z}}_2(N)\mathbf{Z}_1^T(N)] &= \lim_{N\to\infty}\mathbf{Z}_2^{n(N)}[\overline{\mathbf{R}}^{n(N)}]^{-1}\frac{1}{N}\sum_{t=1}^{N}\sum_{s=1}^{N}\mathbb{E}[\varphi_t^{n(N)}e(t)\cdot e(s)\psi^T(s,\rho_0,\eta_0)] \\ &= \mathbf{Z}_2^{n(N)}[\overline{\mathbf{R}}^{n(N)}]^{-1}\sigma_e^2\overline{\mathbb{E}}\left[\varphi_t^{n(N)}\psi^T(t,\rho_0,\eta_0)\right]. \end{aligned} \tag{A.16}$$

For the last term of (A.8), following the same line of above derivations we have

$$\begin{aligned}\lim_{N\to\infty}\mathbb{E}[\mathbf{Z}_1(N)\overline{\mathbf{Z}}_2^T(N)] &= \lim_{N\to\infty}\frac{1}{N}\sum_{t=1}^{N}\sum_{s=1}^{N}\mathbb{E}[\psi(t,\rho_0,\eta_0)e(t)\cdot e(t)(\varphi_t^{n(N)})^T][\overline{\mathbf{R}}^{n(N)}]^{-1}(\mathbf{Z}_2^{n(N)})^T \\ &= \sigma_e^2\overline{\mathbb{E}}\left[\psi(t,\rho_0,\eta_0)(\varphi_t^{n(N)})^T\right][\overline{\mathbf{R}}^{n(N)}]^{-1}(\mathbf{Z}_2^{n(N)})^T. \end{aligned} \tag{A.17}$$

Adding the results of (A.12), (A.15), (A.16) and (A.17) yields the expression for $\mathbf{Q}$ in (2.31). Following the procedure in proving Theorem 9.1 in [15], it can be observed that asymptotically, $\sqrt{N}\mathbf{V}_N'(\rho_0,\hat{\eta}_N)$ is normally distributed, i.e.,

$$\sqrt{N}\mathbf{V}_N'(\rho_0,\hat{\eta}_N) \sim AsN(0,\mathbf{Q}). \tag{A.18}$$

(2) Asymptotic Analysis of $[\mathbf{V}_N''(\xi_N,\hat{\eta}_N)]$

From (A.2)-(A.3) we have the following expression

$$\mathbf{V}_N''(\rho,\hat{\eta}_N) = \frac{1}{N}\sum_{t=1}^{N}\psi(t,\rho,\hat{\eta}_N)\psi^T(t,\rho,\hat{\eta}_N) - \frac{1}{N}\sum_{t=1}^{N}\frac{\partial}{\partial\rho}\psi(t,\rho,\hat{\eta}_N)\varepsilon(t,\rho,\hat{\eta}_N). \tag{A.19}$$

Expanding the first term in the above equation at η_0, similar to the proof of Theorem 2.4.1, we obtain

$$\begin{aligned}&\frac{1}{N}\sum_{t=1}^{N}\psi(t,\rho,\hat{\eta}_N)\psi^T(t,\rho,\hat{\eta}_N) = \frac{1}{N}\sum_{t=1}^{N}\psi(t,\rho,\eta_0)\psi^T(t,\rho,\eta_0) + \frac{1}{N}\sum_{t=1}^{N}\{[A(\hat{\eta}_N)-A(\eta_0)]\psi(t,\rho)\} \\ &\cdot\left\{\psi^T(t,\rho,\eta_0)\right\} + \frac{1}{N}\sum_{t=1}^{N}\left\{\psi(t,\rho,\eta_0)\right\}\left\{[A(\hat{\eta}_N)-A(\eta_0)]\psi^T(t,\rho)\right\}.\end{aligned}$$

It follows that

$$\sup_{\rho\in\Omega_\rho}\left\|\frac{1}{N}\sum_{t=1}^{N}\psi(t,\rho,\hat{\eta}_N)\psi^T(t,\rho,\hat{\eta}_N) - \overline{\mathbb{E}}\psi(t,\rho,\eta_0)\psi^T(t,\rho,\eta_0)\right\| \to 0, \text{ w.p.1, as } N\to\infty. \tag{A.20}$$

In an analogous way we have

$$\sup_{\rho\in\Omega_\rho}\left\|\frac{1}{N}\sum_{t=1}^{N}\frac{\partial}{\partial\rho}\psi(t,\rho,\hat{\eta}_N)\varepsilon(t,\rho,\hat{\eta}_N)-\overline{\mathbb{E}}\frac{\partial}{\partial\rho}\psi(t,\rho,\eta_0)\varepsilon(t,\rho,\eta_0)\right\|\to 0,\ \text{ w.p.1, as } N\to\infty, \tag{A.21}$$

since $\xi_N\in[\hat{\rho}_N,\rho_0]$ and $\hat{\rho}_N\to\rho_0$, w.p.1, as $N\to 0$ if the selected model structure $G(q,\rho)$ in (2.14) contains the true model $G_0(q)$. Therefore, we may conclude that $\xi_N\to\rho_0$ almost surely as sample number tends to infinity. Combining (A.19)-(A.21) and noticing that $\varepsilon(t,\rho,\eta_0)=e(t)$ (thus $\overline{\mathbb{E}}\frac{\partial}{\partial\rho}\psi(t,\rho,\eta_0)\varepsilon(t,\rho,\eta_0)=0$), we have

$$\mathbf{V}_N''(\rho,\hat{\eta}_N)\to\overline{\mathbb{E}}\left[\psi(t,\rho,\eta_0)\psi^T(t,\rho,\eta_0)\right],\ \text{ w.p.1, as } N\to\infty. \tag{A.22}$$

Combining the results of (A.1), (A.18) and (A.22), we can obtain (2.30), where $\mathbf{Q}(\hat{\eta}_N)$ is given by (2.31), and thus this theorem is proved.

Appendix B

Derivations for Chapter 4

B.1 Variance partition

For the measured two-dimensional data set $\mathbf{Y} \in \mathbb{R}^{m \times N}$, it has the following structure:

$$\mathbf{Y} = \begin{array}{c} \\ 1 \\ \vdots \\ i \\ \vdots \\ m \end{array} \begin{array}{c} \begin{array}{cccccc} 1 & \cdots & j & \cdots & N \end{array} \\ \begin{bmatrix} y_{11} & \cdots & y_{1j} & \cdots & y_{1N} \\ \vdots & \ddots & \vdots & \ddots & \vdots \\ y_{i1} & \cdots & y_{ij} & \cdots & y_{iN} \\ \vdots & \ddots & \vdots & \ddots & \vdots \\ y_{m1} & \cdots & y_{mj} & \cdots & y_{mN} \end{bmatrix} \end{array}, \tag{B.1}$$

where each row of $\mathbf{Y}$ refers to the N measurements of one data box, while each column of $\mathbf{Y}$ represents the measured profile at each scan across all the data boxes. The overall sample mean of the data set $\mathbf{Y}$ is defined as,

$$\bar{Y} = \sum_{i=1}^{m} \sum_{j=1}^{N} \frac{y_{ij}}{Nm}. \tag{B.2}$$

The total sample variance σ_T^2 can be calculated as,

$$\sigma_T^2 = \sum_{i=1}^{m} \sum_{j=1}^{N} \frac{(y_{ij} - \bar{Y})^2}{Nm - 1}. \tag{B.3}$$

The CD sample variance σ_{CD}^2 can be calculated as,

$$\sigma_{CD}^2 = \sum_{i=1}^{m} \frac{(\tilde{Y}_i - \bar{Y})^2}{m - 1}, \tag{B.4}$$

where $\tilde{Y}_i = \sum_{j=1}^{N} \frac{y_{ij}}{N}$. The MD sample variance σ_{MD}^2 can be calculated as,

$$\sigma_{MD}^2 = \sum_{j=1}^{N} \frac{(\tilde{Y}_j - \bar{Y})^2}{N-1}, \tag{B.5}$$

where $\tilde{Y}_j = \sum_{i=1}^{m} \frac{y_{ij}}{m}$. The residual sample variance σ_{Res}^2 is calculated as,

$$\sigma_{Res}^2 = \sigma_T^2 - \sigma_{CD}^2 - \sigma_{MD}^2. \tag{B.6}$$

B.2 Derivation of (4.12)

For the disturbance model (4.5), from the Diophantine identity, we have

$$\frac{C(q)}{A(q)} = F(q) + q^{-d}\frac{H(q)}{A(q)}, \tag{B.7}$$

where $F(q)$ and $H(q)$ are scalar polynomials, i.e.,

$$F(q) = f_0 + f_1 q + \ldots + f_{d-1} q^{-d+1}, \tag{B.8}$$

$$H(q) = h_0 + h_1 q + \ldots + h_{n_h} q^{-n_h}. \tag{B.9}$$

Considering the profile at time $t+d$ (supposing the current time is t), from (B.7) we have

$$\mathbf{y}_r(t+d|t) = \hat{\mathbf{y}}_r(t+d|t) + F(q)\phi\mathbf{e}(t+d), \tag{B.10}$$

where $\hat{\mathbf{y}}_r(t+d|t)$ represents the d-step-ahead prediction [120] at t, namely,

$$\hat{\mathbf{y}}_r(t+d|t) = \frac{B(q)F(q)}{C(q)}\mathbf{G}\mathbf{u}_r(t) + \frac{H(q)}{C(q)}\mathbf{y}_r(t). \tag{B.11}$$

Note that the second term in (B.10) is the unpredictable future profile due to the time-delay, which is controller invariant. The first term of (B.10) is controller-dependent and by minimizing $\mathbb{E}[\hat{\mathbf{y}}_r(t+d|t)\hat{\mathbf{y}}_r^T(t+d|t)]$ we will achieve the minimum variance of the residual profile. If the transfer matrix $\mathbf{G}$ in (B.11) is square and invertible, it is possible to find an input sequence such that $\hat{\mathbf{y}}_r(t+d|t) = 0$. However, due to the special

structure, $\mathbf{G}$ is often non-square, and hence the minimum variance of $\hat{\mathbf{y}}_r(t+d|t)$ is achieved by setting

$$\mathbf{u}_r(t) = -\mathbf{G}^{\dagger}\frac{H(q)}{B(q)F(q)}\mathbf{y}_r(t), \tag{B.12}$$

where $\mathbf{G}^{\dagger} = (\mathbf{G}^T\mathbf{G})^{-1}\mathbf{G}^T$ is the pseudo-inverse of $\mathbf{G}$. It should be noted that $\mathbf{G}^{\dagger}$ indeed represents the MVC in the spatial direction due to the special structure of $\mathbf{G}$ (refer to (4.6) and (4.11)) while $\frac{H(q)}{B(q)F(q)}$ denotes the temporal MVC due to time delay. Therefore, (B.12) stands for the temporal and spatial MVC for the residual model (4.3).

Appendix C

Proofs for Chapter 5

C.1 Proof of Theorem 5.3.1

Defining

$$\Phi_y = \begin{bmatrix} \psi_{\bar{y}}(1) \\ \vdots \\ \psi_{\bar{y}}(N) \end{bmatrix},$$

it then follows from (5.15) that

$$\hat{\mathbf{Y}} = [\Phi_y \ \Phi_u] \begin{bmatrix} \mathbf{a} \\ \mathbf{Cb} \end{bmatrix} = \begin{bmatrix} \tilde{\Phi}_y \ \tilde{\Phi}_u \end{bmatrix} \begin{bmatrix} \mathbf{a} \\ \mathbf{Bc} \end{bmatrix}, \tag{C.1}$$

where $\mathbf{B} = diag\{\mathbf{b}, \ldots, \mathbf{b}\}$. $\tilde{\Phi}_y$ and $\tilde{\Phi}_u$ are easily obtained by rearranging Φ_y and Φ_y, respectively. The loss function (5.17) is expressed in a more compact form,

$$V_N(\theta) = \|\mathbf{Y} - \hat{\mathbf{Y}}\|_2^2 = \left\| \mathbf{Y} - [\Phi_y \ \Phi_u] \begin{bmatrix} \mathbf{a} \\ \mathbf{Cb} \end{bmatrix} \right\|_2^2. \tag{C.2}$$

(i) The proof is an extension of Theorem IV.1 in [115]. Note that to ease the notation we will drop the hat in the parameter estimates from (5.20)-(5.22), but add a subscript "N" to stress the fact that these estimates are obtained from N samples of data. It is easy to see that through the iterative identification steps (5.20)-(5.22),

$$V_N(\theta_N^k) = V_N(\mathbf{a}_N^k, \mathbf{b}_N^k, \mathbf{c}_N^k) \leq V_N(\mathbf{a}_N^k, \mathbf{b}_N^k, \mathbf{c}_N^{k-1}) \leq V_N(\mathbf{a}_N^{k-1}, \mathbf{b}_N^{k-1}, \mathbf{c}_N^{k-1}) = V_N(\theta_N^{k-1}).$$

In other words, $V_N(\theta_N^k)$ is nonincreasing. Despite of the nonincreasing $V_N(\theta_N^k)$, without normalization (5.21),

it is possible that $\mathbf{b}_N^k \to \infty$, $\mathbf{c}_N^k \to 0$, as $k \to \infty$, or vice versa, but as a product, $\mathbf{C}_N^k \mathbf{b}_N^k$ remains finite. The presence of normalization step in (5.21) eliminates the above disfavored scenario. As a result, the sequence $\{\mathbf{b}_N^k\}$ is bounded due to the normalization and thus $\{\mathbf{c}_N^k\}$ is bounded. Since otherwise, $V_N(\theta_N^k)$ will become unbounded which contradicts the facts that $\mathbf{Z}^N$ is bounded, all model structures in Ω are stable, and that $V_N(\theta)$ is continuous in θ and nonincreasing.

Now let us concentrate on the convergence analysis of the iterative identification algorithms for large N. First we will establish a statement that when fixing the spatial parameter $\mathbf{c}$, $V_N(\theta)$ is convex in temporal parameters $\{\mathbf{a}, \mathbf{b}\}$ and vice versa. Based on (C.2), we have

$$V_N(\mathbf{a},\mathbf{b},\mathbf{c}) = \mathbf{Y}^T\mathbf{Y} - 2\mathbf{Y}^T\Phi \begin{bmatrix} \mathbf{a} \\ \mathbf{Cb} \end{bmatrix} + \begin{bmatrix} \mathbf{a} \\ \mathbf{Cb} \end{bmatrix}^T \Phi^T\Phi \begin{bmatrix} \mathbf{a} \\ \mathbf{Cb} \end{bmatrix}, \ \Phi = [\Phi_y \ \Phi_u]. \tag{C.3}$$

When the parameter $\mathbf{c}$ is fixed, it is easy to derive that for $\lambda \in [0,1]$,

$$\begin{aligned} V_N(\lambda\mathbf{a}_1 + (1-\lambda)\mathbf{a}_2, \lambda\mathbf{b}_1 + (1-\lambda)\mathbf{b}_2, \mathbf{c}) &= \lambda V_N(\mathbf{a}_1,\mathbf{b}_1,\mathbf{c}) + (1-\lambda)V_N(\mathbf{a}_2,\mathbf{b}_2,\mathbf{c}) \\ -\lambda(1-\lambda)&\left(\begin{bmatrix} \mathbf{a}_1 \\ \mathbf{Cb}_1 \end{bmatrix} - \begin{bmatrix} \mathbf{a}_1 \\ \mathbf{Cb}_1 \end{bmatrix}\right)^T \Phi^T\Phi \left(\begin{bmatrix} \mathbf{a}_2 \\ \mathbf{Cb}_2 \end{bmatrix} - \begin{bmatrix} \mathbf{a}_2 \\ \mathbf{Cb}_2 \end{bmatrix}\right). \end{aligned} \tag{C.4}$$

We mention that due to Assumption 3, for any large N, Φ has full column rank, which renders $\Phi^T\Phi > 0$. Therefore, with the fact that $\mathbf{a} \neq 0$, $\mathbf{b} \neq 0$, $\mathbf{c} \neq 0$, (C.4) implies that

$$V_N(\lambda\mathbf{a}_1 + (1-\lambda)\mathbf{a}_2, \lambda\mathbf{b}_1 + (1-\lambda)\mathbf{b}_2, \mathbf{c}) \geq \lambda V_N(\mathbf{a}_1,\mathbf{b}_1,\mathbf{c}) + (1-\lambda)V_N(\mathbf{a}_2,\mathbf{b}_2,\mathbf{c}).$$

This verifies the convexity of $V_N(\mathbf{a},\mathbf{b},\mathbf{c})$ with respect to $\mathbf{a},\mathbf{b}$. A similar conclusion can be achieved for the convexity of $V_N(\mathbf{a},\mathbf{b},\mathbf{c})$ with respect to $\mathbf{c}$. An immediate consequence of these statements is that in each optimization of the iterative identification algorithm, we have a unique and closed-form solution. It will be shown below that even though $V_N(\theta)$ may not be convex in θ, our algorithm can always converge to its local minimum.

Now define θ^k to be the parameter estimate at k-th iteration. When the iterative identification algorithm (5.20)-(5.22) converges, i.e., $\theta^k \to \theta$ for some θ, we need to show that $\nabla V_N(\theta) = 0$. Suppose that $\nabla V_N(\theta) \neq 0$, then there always exists a direction (e.g. negative gradient) along which $V_N(\theta)$ decreases. Because the

solution to (5.20) and to (5.22) is unique, we can always minimize $V_N(\theta)$ sequentially to achieve another point θ', such that $V_N(\theta') \leq V_N(\theta)$. This contradicts the facts that $V_N(\theta)$ is nonincreasing and θ^k converges to θ. Thus the statement in (i) holds.

(ii) Combining (5.6) and (5.9), one can see that the closed-loop system has the form

$$\mathbf{y}(t) = f_{\mathscr{S}}\left(t, \mathbf{y}^{t-1}, \mathbf{u}^{t-1}\right) + \mathbf{e}^o(t). \tag{C.5}$$

According to Assumption 1, the nonlinear closed-loop system (C.5) is exponentially stable, which satisfies S1-S3 in [121]. Moreover, with the parameterizations (5.12), the one-step-ahead predictor (5.15) of the model is differentiable with respect to parameter θ, which implies the condition M1 in [121]. Our selected quadratic criterion also meets the regularity condition C1 in that paper. As a result, Lemma 3.1 in [121] applies to our scenario, which indicates the validity of (5.29). As the convergence in (5.29) is uniform in $\theta \in \Omega$, (5.30) follows directly from (5.29).

(iii) From Assumptions 1 and 2, it follows that $\varepsilon(t, \theta^o) = \mathbf{e}^o(t)$. Therefore,

$$\begin{aligned} \overline{V}(\theta) - \overline{V}(\theta^o) &= \overline{\mathbb{E}}[\varepsilon(t,\theta) - \varepsilon(t,\theta^o)]^T \varepsilon(t,\theta^o) \\ &\quad + \overline{\mathbb{E}}[\varepsilon(t,\theta) - \varepsilon(t,\theta^o)]^T [\varepsilon(t,\theta) - \varepsilon(t,\theta^o)]. \end{aligned} \tag{C.6}$$

Note that $\varepsilon(t,\theta) - \varepsilon(t,\theta^o) = \hat{\mathbf{y}}(t|\theta) - \hat{\mathbf{y}}(t|\theta^o)$ which only depends on past input-output data and thus is not correlated with current noise $\varepsilon(t,\theta^o)$. Hence, the first term in (C.6) is zero. The second term is always nonnegative which means that $\overline{V}(\theta)$ is always greater than $\overline{V}(\theta^o)$ unless $\hat{\mathbf{y}}(t|t-1,\theta) = \hat{\mathbf{y}}(t|t-1,\theta^o)$. We now show that under the informativeness condition of closed-loop data as in Assumption 3, $\hat{\mathbf{y}}(t|\theta^*) = \hat{\mathbf{y}}(t|\theta^o)$ implies that $\theta^* = \theta^o$. From Assumption 2 and (5.15) we know

$$\hat{\mathbf{y}}(t|\theta^*) - \hat{\mathbf{y}}(t|\theta^o) = \psi(t) \begin{bmatrix} \mathbf{a}^* - \mathbf{a}^o \\ \mathbf{C}\mathbf{b}^* - \mathbf{C}\mathbf{b}^o \end{bmatrix}, \quad \psi(t) = \left[\psi_y(t)\ \psi_{\bar{u}}(t-d)\right]. \tag{C.7}$$

Plugging this into the limit loss function (C.6) yields

$$\overline{\mathbb{E}}[\hat{\mathbf{y}}(t|\theta^*) - \hat{\mathbf{y}}(t|\theta^o)] = \begin{bmatrix} \mathbf{a}^* - \mathbf{a}^o \\ \mathbf{C}\mathbf{b}^* - \mathbf{C}\mathbf{b}^o \end{bmatrix}^T \overline{\mathbb{E}}[\psi^T(t)\psi(t)] \begin{bmatrix} \mathbf{a}^* - \mathbf{a}^o \\ \mathbf{C}\mathbf{b}^* - \mathbf{C}\mathbf{b}^o \end{bmatrix}. \tag{C.8}$$

From Assumption 3a, we know that (5.26) holds for any large N. Thus asymptotically, $\overline{\mathbb{E}}[\psi_{\bar{u}}(t)]$ has full column rank. Moreover, according to (5.27), columns of $\overline{\mathbb{E}}[\psi_{\bar{u}}(t-d)]$ are linearly independent of those in $\overline{\mathbb{E}}[\psi_{\bar{y}}(t)]$. This leads to the statement that $\overline{\mathbb{E}}[\psi^T(t)\psi(t)]$ has full column rank. Therefore, the only situation making $\overline{V}(\theta^*) - \overline{V}(\theta^o) = 0$ is $\mathbf{a}^* = \mathbf{a}^o$, $\mathbf{C}\mathbf{b}^* = \mathbf{C}\mathbf{b}^o$. Note that from the rescaling (step 6) of the algorithm, we can arrive at $\mathbf{C}^* = \mathbf{C}^o$, $\mathbf{b}^* = \mathbf{b}^o$, which ends the proof of (5.31).